Super-resolution in wave imaging

Timothée Wintz

THÈSE DE DOCTORAT

de l'Université de recherche Paris Sciences et Lettres
PSL Research University

Préparée à l'École Normale Supérieure

Super-resolution in wave imaging

Super-résolution en imagerie par ondes

Ecole doctorale n°386

Mathématiques Paris Centre

Spécialité Mathématiques appliquées

COMPOSITION DU JURY :

Mme. LIM Mikyoung
Korea Advanced Institute of Science and Technology, Rapporteur

Mme. SCHÖNLIEB Carola-Bibiana
University of Cambridge, Rapporteur

M. PEYRÉ Gabriel
Ecole Normale Supérieure, Président du jury

M. AMMARI Habib
ETH Zürich, Membre du jury

M. TRIKI Faouzi
Université Grenoble Alpes, Membre du jury

M. POIGNARD Clair
Université de Bordeaux, Membre du jury

Mme. BORCEA Liliana
University of Michigan, Membre du jury

Soutenue par Timothée **WINTZ**
Le 26 juin 2017

Dirigée par Habib AMMARI

ENS ÉCOLE NORMALE SUPÉRIEURE | PSL RESEARCH UNIVERSITY PARIS

Remerciements

Je remercie Habib de m'avoir proposé ce sujet de thèse et de m'avoir accompagné – même à distance – durant ces trois années passées à l'ENS.

Un grand merci à Mikyoung Lim et Carola Schönlieb pour avoir accepté de rapporter ma thèse ainsi qu'aux autres membres du jury, Gabriel Peyré, Faouzi Triki, Clair Poignard et Liliana Borcea.

Je tiens à remercier tout spécialement Giovanni pour son soutien, ses idées, ses conseils et sa rigueur dans la relecture. Merci aussi à Pancho, avec qui j'ai travaillé à l'ETH, toujours dans la bonne humeur !

Merci à ceux que j'ai côtoyés à l'ENS durant ces années: Mattias et Wenlong avec qui j'ai partagé ces années de thèse sous la direction d'Habib, Pierre qui nous a précédé. Merci aussi à Bénédicte et Zaïna, et à Lara pour l'organisation des nombreuses missions à Zürich.

Résumé

Les différentes modalités d'imagerie par ondes présentent chacune des limitations en termes de résolution ou de contraste. Dans ce travail, nous modélisons l'imagerie ultrasonore ultrarapide et présentons des méthodes de reconstruction qui améliorent la précision de l'imagerie ultrasonore. Nous introduisons deux méthodes qui permettent d'augmenter le contraste et de mesurer la position superrésolue et la vitesse dans les vaisseaux sanguins. Nous présentons aussi une méthode de reconstruction des paramètres microscopiques en tomographie d'impédance électrique en utilisant des mesures multifréquence et en s'aidant de la théorie de l'homogénisation.

Abstract

Different modalities in wave imaging each present limitations in terms of resolution or contrast. In this work, we present a mathematical model of the ultrafast ultrasound imaging modality and reconstruction methods which can improve contrast and resolution in ultrasonic imaging. We introduce two methods which allow to improve contrast and to locate blood vessels below the diffraction limit while simultaneously estimating the blood velocity. We also present a reconstruction method in electrical impedance tomography which allows reconstruction of microscopic parameters from multi-frequency measurements using the theory of homogenization.

Contents

Introduction

In medical imaging, inverse problems are often ill-posed, or limited in their resolution by the physics of the waves at play. There exist several techniques to overcome these difficulties, using additional information about the medium. For example, by reducing the set of admissible solutions and the number of unknowns, by looking for a inclusions with parameters significantly different from those of the surrounding medium [8].

Assuming different frequency responses for different tissue components, another approach uses signal separation techniques to reconstruct robust solutions using multi-frequency settings [6], [1], [2].

A third promising technique for improving the robustness of wave-based imaging is to combine different physical types of waves. This allows to alleviate deficiencies of each separate type of waves and to combine their strengths. Example of multi-wave imaging modalities include photo-acoustic and thermo-acoustic imaging [53], magnetic resonance elastography [41], magneto-acousto-electrical tomography [47], magneto-acoustic tomography with magnetic induction [54], and impediography [34].

Recently, nanoparticles have been proposed to be used as labels in molecular biology. Plasmon resonant nanoparticles have unique capabilities of enhancing the brightness and directivity of light and confining strong electromagnetic fields [38]. These nonlinear optical contrast mechanisms reveal new information from biological specimens and tissues.

Finally, one can use the specific dynamics of the imaged elements to improve the robustness of the imaging process. For example in blood flow imaging, the blood dynamics are used to locate blood vessels [13]. Such techniques have been successfully used in Dynamic Optical Coherence Tomography [10].

This thesis aims at investigating different methods for improving the resolution and contrast of wave-based imaging techniques for imaging of biological tissues. It is focused on two promising non-invasive imaging methods: ultrafast ultrasound, based on the propagation of sound waves, and electrical impedance tomography (EIT), based on the propagation of low frequency electro-magnetic waves. Both ultrasound imaging and EIT present the ad-

vantage of being fast, relatively cheap and easy to operate. These methods are examples of the tradeoff between contrast and resolution that is encountered in many wave-based imaging techniques. Ultrasound imaging provides a high resolution of the order of less than a millimeter, but since acoustic impedance has a poor contrast in biological media, its contrast is very low. On the contrary, due to its low frequency nature, EIT provides a very low resolution, and due to its ill-posedness is very sensitive to measurements errors. Contrast is not a problem though, since different features in biological tissues present very distinct conductivities.

To overcome these difficulties, several approaches are possible. Ultrafast ultrasound is a promising imaging modality based on acoustic propagation. Instead of using focused waves as is the case in traditional echography, ultrafast ultrasound is based on plane waves produced by an array of piezzoelectrical elements. This allows for very high numbers of images per seconds, up to 10000Hz. This method induces a worse signal-to-noise ratio (SNR) than conventional echography, but by combining the information of a whole sequence of images, this allows for better imaging, for example in blood flow imaging. Signal processing techniques can then be used to improve reconstruction, using knowledge on dynamics of blood and tissue.

We make use of the dynamics of blood flow, and show that it can be used to improve the imaging of blood vessels.

In the case of a cell culture, it is impossible to directly image the microstructure. An idea developed in this thesis to improve the usefulness of EIT is to use the theory of homogenization and a very precise a priori model on the micro-structure. This model, combined with multi-frequency measurements, will allow us to reconstruct precise information about the micro-structure.

Overview of the thesis

The thesis is divided into four chapters.

First chapter

This chapter provides a mathematical analysis of ultrafast ultrasound imaging. This newly emerging modality for biomedical imaging uses plane waves instead of focused waves in order to achieve very high frame rates. We derive the point spread function of the system in the Born approximation for wave propagation and study its properties.

Second chapter

In this chapter, we consider dynamic data for blood flow imaging, and introduce a suitable random model for blood cells. We show that a singular value decomposition method can successfully remove the clutter signal by using the different spatial coherence of tissue and blood signals, thereby providing high-resolution images of blood vessels, even in cases when the clutter and blood speeds are comparable in magnitude. Several numerical simulations are presented to illustrate and validate the approach.

Third chapter

In this chapter, we introduce a signal processing method to produce simultaneous localization and velocity measurements of blood vessels, with super-resolution. The method is based on L1 minimization and sparsity, with an added dynamic parameter. Numerical experiments show that this method allow for a reconstruction of both particle location and velocity.

Fourth chapter

In this chapter, we present a simplified electrical model for tissue culture. We derive a mathematical structure for overall electrical properties of the culture and study their dependence on the frequency of the current. We introduce a method for recovering the microscopic properties of the cell culture from the spectral measurements of the effective conductivity. Numerical examples are provided to illustrate the performance of our approach.

Publications

Results of chapters 1 and 2 are published in [3]. Results of chapter 4 is published in [7]. Chapter 3 will be published in a forthcoming paper.

Chapter 1

Modeling of Ultrafast Ultrasound Imaging

1.1 Introduction

Conventional ultrasound imaging is performed with focused ultrasonic waves [49, 48]. This yields relatively good spatial resolution, but clearly limits the acquisition time, since the entire specimen has to be scanned. Over the last decade, ultrafast imaging in biomedical ultrasound has been developed [44, 50, 23]. Plane waves are used instead of focused waves, thereby limiting the resolution but increasing the frame rate considerably, up to 20,000 frames per second. Ultrafast imaging has been made possible by the recent technological advances in ultrasonic transducers, but the idea of ultrafast ultrasonography dates back to 1977 [17]. The advantages given by the very high frame rate are many, and the applications of this new modality range from blood flow imaging [12, 23], deep super-resolution vascular imaging [26] and functional imaging of the brain [40, 39] to ultrasound elastography [29]. In this chapter we focus on blood flow imaging.

A single ultrafast ultrasonic image is obtained as follows [44]. A pulsed plane wave (focused on the imaging plane – see Figure 1.1b) insonifies the medium, and the back-scattered echoes are measured at the receptor array, a linear array of piezoelectric transducers. These spatio-temporal measurements are then beamformed to obtain a two-dimensional spatial signal. This is what we call *static inverse problem*, as it involves only a single wave, and the dynamics of the medium is not captured. The above procedure yields very low lateral resolution, i.e. in the direction parallel to the wavefront, because of the absence of focusing. In order to solve this issue, it was proposed to use multiple waves with different angles: these improve the lateral

resolution, but has the drawback of reducing the frame rate.

In this work, we provide a detailed mathematical analysis of ultrasound ultrafast imaging. To our knowledge, this is the first mathematical study addressing the important challenges of this emerging and very promising modality. Even though in this work we limit ourselves to formalize the existing methods, the mathematical analysis provided gives important insights, which we expect will lead to improved reconstruction schemes.

First, we carefully study the forward and inverse static problems. In particular, we derive the point spread function (PSF) of the system, in the Born approximation for ultrasonic wave propagation. We investigate the behavior of the PSF, and analyze the advantages of angle compounding. In particular, we study the lateral and vertical resolutions. In addition, this analysis allows us to fully understand the roles of the key parameters of the system, such as the directivity of the array and the settings related to angle compounding.

This chapter is structured as follows. In Section 1.2 we describe the imaging system and the model for wave propagation. In Section 1.3 we discuss the static inverse problem. In particular, we describe the beamforming process, the PSF and the angle compounding technique.

1.2 The Forward Problem

The imaging system is composed of a medium contained in $\mathbb{R}^3_+ := \{(x, y, z) \in \mathbb{R}^3 : z > 0\}$ and of a fixed linear array of transducers located on the line $z = 0, y = 0$. This linear array of piezoelectric transducers (see [49, Chapter 7]) produces an acoustic illumination that is focused in elevation – in the y coordinates, near the plane $y = 0$ – and has the form of a plane wave in the direction $\mathbf{k} \in S^1$ in the x, z coordinates (see Figure 1.1b). Typical sizes for the array length and for the penetration depth are about 10^{-1} m.

We make the assumption that the acoustic incident field u^i can be approximated as

$$u^i(x, y, z, t) = A_z(y) f\left(t - c_0^{-1}\mathbf{k} \cdot (x, z)\right),$$

where c_0 is the background speed of sound in the medium. The function A_z describes the beam waist in the elevation direction at depth z (between $4 \cdot 10^{-3}$ m and 10^{-2} m). This is a simplified expression of the true incoming wave, which is focused by a cylindrical acoustic lens located near the receptor array (see [49, Chapters 6 and 7]). The function f is the waveform describing the shape of the input pulse:

$$f(t) = e^{2\pi i \nu_0 t} \chi(\nu_0 t), \qquad \chi(u) = e^{-\frac{u^2}{\tau^2}}, \tag{1.1}$$

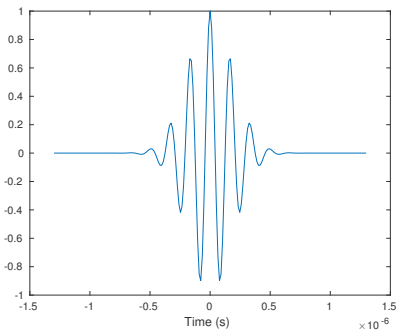

(a) The real part of the input pulse f.

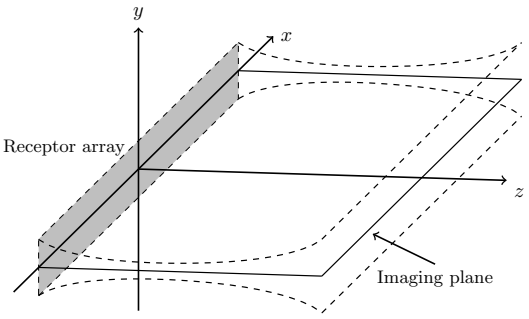

(b) The imaging system. The incident wave is supported near the imaging plane $\{y = 0\}$, within the focusing region bounded by the two curved surfaces.

Figure 1.1: The pulse f of the incident wave u^i and the focusing region.

where ν_0 is the principal frequency and τ the width parameter of the pulse (see Figure 1.1a). Typically, ν_0 will be of the order of $10^6\,\mathrm{s}^{-1}$. More precisely, realistic quantities are

$$c_0 = 1.5 \cdot 10^3\,\mathrm{m}\cdot\mathrm{s}^{-1}, \quad \nu_0 = 6 \cdot 10^6\,\mathrm{s}^{-1}, \quad \tau = 1. \tag{1.2}$$

Let $c : \mathbb{R}^3 \to \mathbb{R}_+$ be the speed of sound and consider the perturbation n given by

$$n\left(\mathbf{x}\right) = \frac{1}{c^2\left(\mathbf{x}\right)} - \frac{1}{c_0^2}.$$

We assume that $\operatorname{supp} n \subseteq \mathbb{R}^3_+$. The acoustic pressure in the medium satisfies the wave equation

$$\Delta u\left(\mathbf{x}, t\right) - \frac{1}{c^2\left(\mathbf{x}\right)} \frac{\partial^2}{\partial t^2} u\left(\mathbf{x}, t\right) = 0, \qquad \mathbf{x} \in \mathbb{R}^3,$$

with a suitable radiation condition on $u - u^i$. Let G denote the Green's function for the acoustic wave equation in $\mathbb{R}^3$ [5, 52]:

$$G(\mathbf{x}, t, \mathbf{x}', t') = -\frac{(4\pi)^{-1}}{|\mathbf{x} - \mathbf{x}'|} \delta\left((t - t') - c_0^{-1}\left|\mathbf{x} - \mathbf{x}'\right|\right).$$

In the following, we will assume that the Born approximation holds, i.e. we consider only first reflections on scatterers, and neglect subsequent reflections [5, 21] (in cases when the Born approximation is not valid, nonlinear methods

have to be used). This is a very common approximation in medical imaging, and is justified by the fact that soft biological tissues are almost acoustic homogeneous, due to the high water concentration. In mathematical terms, it consists in the linearization around the constant sound speed c_0. In this case, the scattered wave $u^s := u - u^i$ is given by

$$u^s(\mathbf{x},t) = \int_{\mathbb{R}}\int_{\mathbb{R}^3} n(\mathbf{x}')\,\frac{\partial^2 u^i}{\partial t^2}(\mathbf{x}',t')\,G(\mathbf{x},t,\mathbf{x}',t')\,d\mathbf{x}'dt', \qquad \mathbf{x}\in\mathbb{R}^3,\ t\in\mathbb{R}_+,$$

since contributions from $n\partial_t^2 u^s$ are negligible. Therefore, inserting the expressions for the Green's function and for the incident wave yields

$$u^s(\mathbf{x},t) = -\int_{\mathbb{R}^3} \frac{(4\pi)^{-1}}{|\mathbf{x}-\mathbf{x}'|} n(\mathbf{x}')\,A_{z'}(y')\,f''\left(t - c_0^{-1}\left((x',z')\cdot\mathbf{k} + |\mathbf{x}-\mathbf{x}'|\right)\right)d\mathbf{x}',$$

where we set $\mathbf{x} = (x,y,z)$ and $\mathbf{x}' = (x',y',z')$. Since the waist of the beam in the y direction is small compared to the distance at which we image the medium, we can make the assumption

$$|\mathbf{x} - (x',y',z')| \simeq |\mathbf{x} - (x',0,z')|, \qquad \mathbf{x} = (x,0,0)\in\mathbb{R}^3,$$

so that the following expression for u^s holds for $\mathbf{x} = (x,0,0)\in\mathbb{R}^3$ and $t>0$:

$$u^s(\mathbf{x},t) = \\ \int_{\mathbb{R}^2} \frac{-(4\pi)^{-1}}{|\mathbf{x}-(x',0,z')|} f''\left(t - c_0^{-1}\left((x',z')\cdot\mathbf{k} + |\mathbf{x}-(x',0,z')|\right)\right)\tilde{n}(x',z')dx'dz',$$

where $\tilde{n}$ is given by

$$\tilde{n}(x',z') := \int_{\mathbb{R}} n(\mathbf{x}')\,A_{z'}(y')\,dy', \qquad \mathbf{x}' = (x',y',z')\in\mathbb{R}^3. \tag{1.3}$$

Since our measurements are only two-dimensional (one spatial dimension given by the linear array and one temporal dimension), we cannot aim to reconstruct the full three-dimensional refractive index n. However, the above identity provides a natural expression for what can be reconstructed: the vertical averages $\tilde{n}$ of n. Since A_z is supported near $y=0$, $\tilde{n}$ reflects the contribution of n only near the imaging plane. In physical terms, $\tilde{n}$ contains all the scatterers in the support of A_z; these scatterers are in some sense projected onto $y=0$, the imaging plane. For simplicity, with an abuse of notation from now on we shall simply denote $\tilde{n}$ by n, since the original three-dimensional n will not play any role, due to the dimensionality restriction

discussed above. Moreover, for the same reasons, all vectors $\mathbf{x}$ and $\mathbf{x}'$ will be two-dimensional, namely, $\mathbf{x} = (x, z)$ and similarly for $\mathbf{x}'$. In view of these considerations, for $\mathbf{x} = (x, 0) \in \mathbb{R}^2$ and $t > 0$ the scattering wave takes the form

$$u^s(\mathbf{x}, t) = -\int_{\mathbb{R}^2} \frac{(4\pi)^{-1}}{|\mathbf{x} - \mathbf{x}'|} f''\left(t - c_0^{-1}\left(\mathbf{x}' \cdot \mathbf{k} + |\mathbf{x} - \mathbf{x}'|\right)\right) n(\mathbf{x}')\, d\mathbf{x}'. \quad (1.4)$$

It is useful to parametrize the direction $\mathbf{k} \in S^1$ of the incident wave by $\mathbf{k} = \mathbf{k}_\theta = (\sin\theta, \cos\theta)$ for some $\theta \in \mathbb{R}$; in practice, $|\theta| \leq 0.25$ [44].

1.3 The Inverse Problem

The static inverse problem consists in the reconstruction of n (up to a convolution kernel) from the measurements u^s at the receptors, assuming that n does not depend on time. This process provides a single image, and will be repeated many times in order to obtain dynamic imaging, as it is discussed in the next sections.

1.3.1 Beamforming

The receptor array is a segment $\Gamma = (-A, A) \times \{0\}$ for some $A > 0$. The travel time from the receptor array to a point $\mathbf{x} = (x, z)$ and back to a receptor located in $\mathbf{u}_0 = (u, 0)$ is given by

$$\tau_{\mathbf{x}}^{\theta}(u) = c_0^{-1}\left(\mathbf{x} \cdot \mathbf{k}_\theta + |\mathbf{x} - \mathbf{u}_0|\right).$$

The beamforming process [49, 44] consists in averaging the measured signals on Γ at $t = \tau_{\mathbf{x}}^{\theta}(u)$, which results in the image

$$s_\theta(x, z) := \int_{x-Fz}^{x+Fz} u^s\left(\mathbf{u}_0, \tau_{\mathbf{x}}^{\theta}(u)\right) du, \mathbf{x} = (x, z) \in \mathbb{R}^2_+ := \{(x, z) \in \mathbb{R}^2 : z > 0\}.$$

The dimensionless aperture parameter F indicates which receptors are chosen to image the location $\mathbf{x} = (x, z)$, and depends on the directivity of the ultrasonic array (in practice, $0.25 \leq F \leq 0.5$ [44]). In general, F depends on the medium roughness and on θ, but this will not be considered this work. The above identity is the key of the static inverse problem: from the measurements $u^s((u, 0), t)$ we reconstruct $s_\theta(x, z)$.

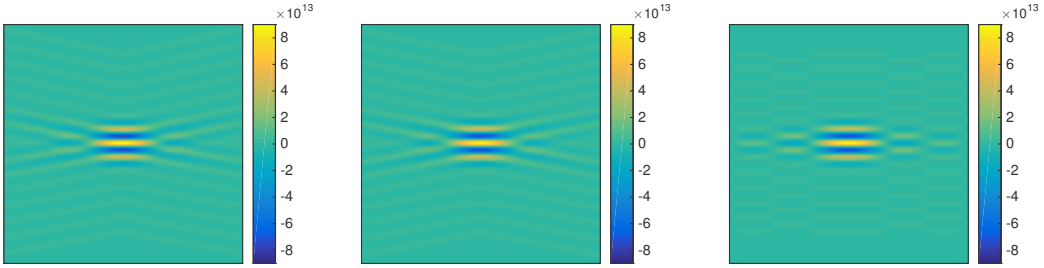

(a) The exact PSF given in (1.6).

(b) The approximation of the PSF given in (1.9).

(c) The approximation of the PSF given in (1.10).

Figure 1.2: The real part of the point spread function g_0 and its approximations are shown in these figures (with parameters as in (1.1) and (1.2), and $F = 0.4$). The size of the square shown is $2\,\text{mm} \times 2\,\text{mm}$, and the horizontal and vertical axes are the x and z axes, respectively. The relative error in the L^∞ norm is about 7% for the approximation shown in panel (b) and about 9% for the approximation shown in panel (c).

We now wish to understand how s_θ is related to n. In order to do so, observe that by (1.4) we may write for $\mathbf{x} \in \mathbb{R}^2_+$

$$\begin{aligned} s_\theta(x,z) &= -\int_{\mathbf{x}'\in\mathbb{R}^2} n(\mathbf{x}') \int_{x-Fz}^{x+Fz} \frac{(4\pi)^{-1}}{|\mathbf{x}'-\mathbf{u}_0|} f''\left(\tau^\theta_{\mathbf{x}}(u) - \tau^\theta_{\mathbf{x}'}(u)\right) du\, d\mathbf{x}' \\ &= \int_{\mathbf{x}'\in\mathbb{R}^2} g_\theta(\mathbf{x},\mathbf{x}')\, n(\mathbf{x}')\, d\mathbf{x}', \end{aligned} \tag{1.5}$$

where g_θ is defined as

$$g_\theta(\mathbf{x},\mathbf{x}') = -\int_{x-Fz}^{x+Fz} \frac{(4\pi)^{-1}}{|\mathbf{x}'-\mathbf{u}_0|} f''\left(\tau^\theta_{\mathbf{x}}(u) - \tau^\theta_{\mathbf{x}'}(u)\right) du, \tag{1.6}$$

(see Figure 1.2a for an illustration in the case when $\theta = 0$). In other words, the reconstruction s_θ is the result of an integral operator given by the kernel g_θ applied to the refractive index n. Thus, the next step is the study of the point spread function (PSF) $g_\theta(\mathbf{x},\mathbf{x}')$, which should be thought of as the image corresponding to a delta scatterer in $\mathbf{x}'$.

1.3.2 The point spread function

In its exact form, it does not seem possible to simplify the expression for g further: we will have to perform some approximations. First, observe that

setting $h^\theta_{\mathbf{x},\mathbf{x}'}(u) = \tau^\theta_{\mathbf{x}}(u) - \tau^\theta_{\mathbf{x}'}(u)$ for $\mathbf{x}, \mathbf{x}' \in \mathbb{R}^2_+$ we readily derive

$$\begin{aligned}(h^\theta_{\mathbf{x},\mathbf{x}'})'(u) &= c_0^{-1}\left(\frac{u-x}{|\mathbf{x}-\mathbf{u}_0|} - \frac{u-x'}{|\mathbf{x}'-\mathbf{u}_0|}\right) \\ &\approx c_0^{-1}\left(\frac{u-x}{|\mathbf{x}'-\mathbf{u}_0|} - \frac{u-x'}{|\mathbf{x}'-\mathbf{u}_0|}\right) = c_0^{-1}\frac{x'-x}{|\mathbf{x}'-\mathbf{u}_0|},\end{aligned}$$

for $\mathbf{x}$ close to $\mathbf{x}'$ (note that, otherwise, the magnitude of the PSF would be substantially lower). As a consequence, by (1.6) we have

$$\begin{aligned}g_\theta(\mathbf{x},\mathbf{x}') &\approx \frac{c_0(4\pi)^{-1}}{x-x'}\int_{x-Fz}^{x+Fz}(h^\theta_{\mathbf{x},\mathbf{x}'})'(u) f''\left(h^\theta_{\mathbf{x},\mathbf{x}'}(u)\right) du \\ &= \frac{c_0(4\pi)^{-1}}{x-x'}\left[f'(h^\theta_{\mathbf{x},\mathbf{x}'}(x+Fz)) - f'(h^\theta_{\mathbf{x},\mathbf{x}'}(x-Fz))\right].\end{aligned} \tag{1.7}$$

In order to simplify this expression even further, let us do a Taylor expansion of $w^\theta_\pm(x,z) := h^\theta_{\mathbf{x},\mathbf{x}'}(x \pm Fz)$ with respect to (x,z) around (x',z'). Direct calculations show that

$$w^\theta_\pm(x',z') = 0, \nabla w^\theta_\pm(x',z') = \frac{c_0^{-1}}{C_F}(C_F\sin\theta \mp F, 1 + C_F\cos\theta),$$

where we define

$$C_F := \sqrt{1+F^2}.$$

Whence

$$\begin{aligned}h^\theta_{\mathbf{x},\mathbf{x}'}(x \pm Fz) \approx &\frac{c_0^{-1}}{C_F}\left((1+C_F\cos\theta)(z-z')\right. \\ &\left.+(C_F\sin\theta \mp F)(x-x')\right).\end{aligned}$$

Substituting this expression into (1.7) yields

$$g_\theta(\mathbf{x},\mathbf{x}') \approx \tilde{g}_\theta(\mathbf{x}-\mathbf{x}'), \tag{1.8}$$

where

$$\begin{aligned}\tilde{g}_\theta(\mathbf{x}) = \frac{c_0}{4\pi x}\left[f'\left(\frac{c_0^{-1}}{C_F}\left((1+C_F\cos\theta)z + (C_F\sin\theta - F)x\right)\right)\right. \\ \left.-f'\left(\frac{c_0^{-1}}{C_F}\left((1+C_F\cos\theta)z + (C_F\sin\theta + F)x\right)\right)\right],\end{aligned} \tag{1.9}$$

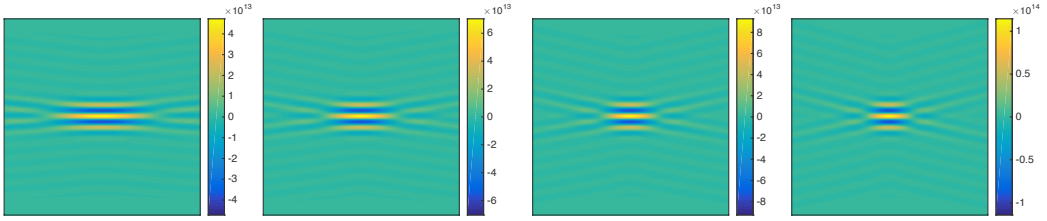

(a) The PSF with $F = 0.2$.

(b) The PSF with $F = 0.3$.

(c) The PSF with $F = 0.4$.

(d) The PSF with $F = 0.5$.

Figure 1.3: The exact PSF with different values of the aperture parameter F (with parameters as in (1.1) and (1.2), and $\theta = 0$). The size of the square shown is $2\,\text{mm} \times 2\,\text{mm}$, and the horizontal and vertical axes are the x and z axes, respectively.

(see Figure 1.2b for an illustration in the case $\theta = 0$), thereby allowing to write the image s_θ given in (1.5) as a convolution of $\tilde{g}_\theta$ and the refractive index n, namely

$$s_\theta(\mathbf{x}) = \int_{\mathbf{x}' \in \mathbb{R}^2} \tilde{g}_\theta(\mathbf{x} - \mathbf{x}') n(\mathbf{x}')\, d\mathbf{x}' = (\tilde{g}_\theta * n)(\mathbf{x}), \qquad \mathbf{x} \in \mathbb{R}^2_+.$$

The validity of this approximation, obtained by truncating the Taylor expansion of $w^\theta_\pm$ at the first order, is by no means obvious. Indeed, by construction, the pulse $f(t)$ is highly oscillating ($\nu_0 \approx 6 \cdot 10^6\,\text{s}^{-1}$), and therefore even small variations in t may result in substantial changes in $f(t)$. However, this does not happen, since if (x, z) is not very close to (x', z') then the magnitude of the PSF is very small, if compared to the maximum value. The verification of this fact is quite technical, and thus is omitted: the details may be found in Appendix A.

Remark 1. From this expression, it is easy to understand the role of the aperture parameter F, which depends on the directivity of the array. Ignoring the second order effect in F and taking, for simplicity $\theta = 0$, we can further simplify the above expression as

$$\tilde{g}_0(\mathbf{x}) \approx \frac{c_0}{4\pi x} \left[f'\left(c_0^{-1}(2z - Fx)\right) - f'\left(c_0^{-1}(2z + Fx)\right) \right].$$

It is clear that F affects the resolution in the variable x: the higher F is, the higher the resolution is. Moreover, the aperture parameter affects also the orientation of the diagonal tails in the PSF. These two phenomena can be clearly seen in Figure 1.3. In general, the higher the aperture is the better for the reconstruction: as expected, the intrinsic properties of the array affects the reconstruction.

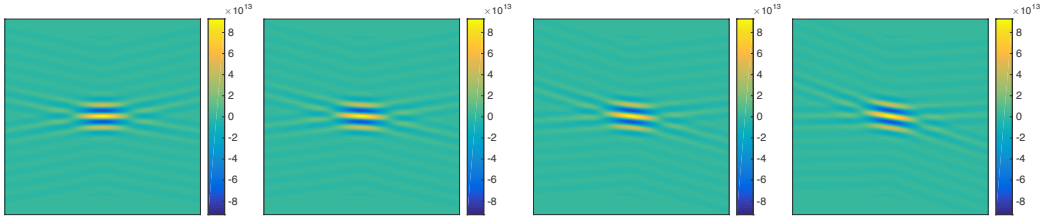

(a) The PSF with $\theta = 0$.

(b) The PSF with $\theta = 0.1$.

(c) The PSF with $\theta = 0.2$.

(d) The PSF with $\theta = 0.3$.

Figure 1.4: The exact PSF with different values of the angle θ (with parameters as in (1.1) and (1.2), and $F = 0.4$). The size of the square shown is $2\,\text{mm} \times 2\,\text{mm}$, and the horizontal and vertical axes are the x and z axes, respectively.

Remark 2. It is also easy to understand the role of the angle θ. In view of

$$\tilde{g}_\theta(\mathbf{x}) \approx \frac{c_0}{4\pi x}\left[f'\left(c_0^{-1}\left((1+\cos\theta)z + (\sin\theta - F)x\right)\right)\right.$$
$$\left. - f'\left(c_0^{-1}\left((1+\cos\theta)z + (\sin\theta + F)x\right)\right)\right],$$

an angle $\theta \neq 0$ substantially gives a rotation of the PSF; see Figure 1.4.

We have now expressed g_θ as a convolution kernel. In order to better understand the different roles of the variables x and z, it is instructive to use the actual expression for f given in (1.1). Since $f'(t) = \nu_0 e^{2\pi i \nu_0 t}\tilde{\chi}(\nu_0 t)$, with $\tilde{\chi}(t) = 2\pi i \chi(t) + \chi'(t)$, we can write

$$\begin{aligned} & f'\left(\frac{c_0^{-1}}{C_F}\left((1 + C_F\cos\theta)z + (C_F\sin\theta \pm F)x\right)\right) \\ & = \nu_0 e^{\frac{2\pi i \nu_0 c_0^{-1}}{C_F}((1+C_F\cos\theta)z + (C_F\sin\theta \pm F)x)} \\ & \quad \tilde{\chi}\left(\frac{\nu_0 c_0^{-1}}{C_F}\left((1 + C_F\cos\theta)z + (C_F\sin\theta \pm F)x\right)\right) \\ & \approx \nu_0 e^{2\pi i \nu_0 c_0^{-1}(2z + (\theta \pm F)x)}\tilde{\chi}\left(2\nu_0 c_0^{-1} z\right), \end{aligned}$$

where we have approximated the dependence on F and θ at first order around $F = 0$ and $\theta = 0$ in the complex exponential (recall that F and θ are small) and at zero-th order ($F = 0$ and $\theta = 0$) inside $\tilde{\chi}$: the difference in the orders is motivated by the fact that the variations of the complex exponentials have much higher frequencies than those of $\tilde{\chi}$, since several oscillations are contained in the envelope defined by χ, as it can be easily seen in Figure 1.1a (and similarly for χ'). This approximation may be justified by arguing as in

Appendix A. Inserting this expression into (1.9) yields

$$\begin{aligned}\tilde{g}_\theta(\mathbf{x}) &\approx \frac{c_0\nu_0}{4\pi x}\left[e^{2\pi i\nu_0 c_0^{-1}(2z+(\theta-F)x)}\tilde{\chi}\left(2\nu_0 c_0^{-1}z\right) - e^{2\pi i\nu_0 c_0^{-1}(2z+(\theta+F)x)}\tilde{\chi}\left(2\nu_0 c_0^{-1}z\right)\right] \\ &= -\frac{i\nu_0 c_0}{2\pi x}\,\tilde{\chi}\left(2\nu_0 c_0^{-1}z\right)e^{4\pi i\nu_0 c_0^{-1}z}e^{2\pi i\nu_0 c_0^{-1}\theta x}\,\sin(2\pi\nu_0 c_0^{-1}Fx),\end{aligned}$$

whence for every $\mathbf{x} = (x, z) \in \mathbb{R}^2$

$$\tilde{g}_\theta(\mathbf{x}) \approx -i\nu_0^2 F\tilde{\chi}\left(2\nu_0 c_0^{-1}z\right)e^{4\pi i\nu_0 c_0^{-1}z}e^{2\pi i\nu_0 c_0^{-1}\theta x}\,\mathrm{sinc}(2\pi\nu_0 c_0^{-1}Fx), \qquad (1.10)$$

where $\mathrm{sinc}(x) := \sin(x)/x$ (see Figure 1.2c). This final expression allows us to analyze the PSF $\tilde{g}_\theta$, and in particular its different behaviors with respect to the variables x and z. Consider for simplicity the case $\theta = 0$ (with $\tau = 1$). In view of the term $\tilde{\chi}\left(2\nu_0 c_0^{-1}z\right)$, the vertical resolution is approximately $0.8 \cdot \nu_0^{-1}c_0$; similarly, in view of the term $\mathrm{sinc}(2\pi\nu_0 c_0^{-1}Fx)$, the horizontal resolution is approximately $\frac{1}{2F}\,\nu_0^{-1}c_0$. Even though horizontal and vertical resolutions are comparable, in terms of focusing and frequencies of oscillations the PSF has very different behaviours in the two directions. Indeed, we can observe that the focusing in the variable z is sharper than that in the variable x: the decay of $\tilde{\chi}$ is much stronger than the decay of sinc. Moreover, in the variable z we have only high oscillations, while in the variable x the highest oscillations are at least four times slower ($2 = 4\frac{1}{2} \geq 4F$), and very low frequencies are present as well, due to the presence of the sinc. As it is clear from Figure 1.2, this approximation introduces evident distortions of the tails, as it is expected from the approximation $F = 0$ inside $\tilde{\chi}$; however, the center of the PSF is well approximated. Similar considerations are valid for the case when $\theta \neq 0$: as observed before, this simply gives a rotation.

The same analysis may be carried out by looking at the expression of the PSF in the frequency domain. For simplicity, consider the case $\theta = 0$: the general case simply involves a translation in the frequency domain with respect to x. Thanks to the separable form of $\tilde{g}_\theta$ given in (1.10), the Fourier transform may be directly calculated, and results in the product of the Fourier transform of $\tilde{\chi}$ and the Fourier transform of the sinc. More precisely, we readily derive

$$\begin{aligned}\mathcal{F}\tilde{g}_\theta(\xi_x,\xi_z) &= \int_{\mathbb{R}^2}\tilde{g}_\theta(x,z)e^{-2\pi i(x\xi_x+z\xi_z)}\,dxdz \\ &\approx -i\nu_0^2 F\int_{\mathbb{R}}\mathrm{sinc}(2\pi\nu_0 c_0^{-1}Fx)e^{-2\pi ix\xi_x}\,dx \\ &\quad\times\int_{\mathbb{R}}\tilde{\chi}\left(\nu_0 c_0^{-1}z\right)e^{-2\pi i(-2\nu_0 c_0^{-1}+\xi_z)z}\,dz.\end{aligned}$$

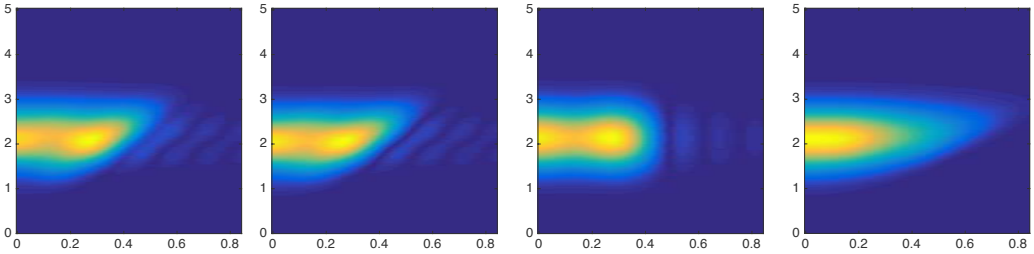

(a) The Fourier transform of the exact PSF g_0 given in (1.6).

(b) The Fourier transform of the approximation of the PSF $\tilde{g}_0$ given in (1.9).

(c) The Fourier transform (1.11) of the approximation of the PSF $\tilde{g}_0$ given in (1.10).

(d) The Fourier transform of the PSF g_Θ^{ac} given in (1.13), for $\Theta = 0.25$.

Figure 1.5: The absolute values of the Fourier transforms of the point spread functions and its approximations (with parameters as in (1.1) and (1.2), and $F = \theta = 0$). The frequency axes are normalized by $\nu_0 c_0^{-1}$: the PSF is a low pass filter with cut-off frequency $F\nu_0 c_0^{-1}$ with respect to the variable x and a band pass filter around $2\nu_0 c_0^{-1}$ with respect to z.

Thus, since the Fourier transform of the sinc may be easily computed and is a suitable scaled version of the rectangle function, we have

$$\begin{aligned}\mathcal{F}\tilde{g}_\theta(\xi_x,\xi_z) &\approx -i\nu_0^2 F \frac{1}{2\nu_0 c_0^{-1} F}\mathbb{1}_{[-F,F]}\left(c_0\nu_0^{-1}\xi_x\right)\\ &\quad\times\int_{\mathbb{R}}\tilde{\chi}\left(\nu_0 c_0^{-1} z\right)e^{-2\pi i(-2\nu_0 c_0^{-1}+\xi_z)z}\,dz\\ &= -\frac{ic_0\nu_0}{2}\mathbb{1}_{[-F,F]}\left(c_0\nu_0^{-1}\xi_x\right)\frac{1}{\nu_0 c_0^{-1}}\mathcal{F}\tilde{\chi}\left(\frac{-2\nu_0 c_0^{-1}+\xi_z}{\nu_0 c_0^{-1}}\right),\end{aligned}$$

whence

$$\mathcal{F}\tilde{g}_\theta(\xi_x,\xi_z) \approx -ic_0^2\,\mathbb{1}_{[-F,F]}\left(c_0\nu_0^{-1}\xi_x\right)\mathcal{F}\tilde{\chi}\left(-2+\nu_0^{-1}c_0\xi_z\right)/2. \tag{1.11}$$

Therefore, up to a constant, the Fourier transform of the PSF is a low-pass filter in the variable x with cut-off frequency $F\nu_0 c_0^{-1}$ and a band pass filter in z around $2\nu_0 c_0^{-1}$ (since $\tilde{\chi}$ is a low-pass filter). This explains, from another point of view, the different behaviors of $\tilde{g}_\theta$ with respect to x and z. This difference is evident from Figure 1.5, where the absolute values of the Fourier transforms of the different approximations of the PSF are shown.

1.3.3 Angle compounding

We saw in the previous subsection that, while very focused in the direction z, the PSF is not very focused in the direction x due to the presence of the

sinc function, see (1.10). In order to have a better focusing, it was proposed in [44] to use multiple measurements corresponding to many angles in an interval $\theta \in [-\Theta, \Theta]$ for some $0 \leq \Theta \leq 0.25$. The reason why this technique is promising is evident from Figure 1.4: adding up several angles together will result in an enhancement of the center of the PSF, and in a substantial reduction of the artifacts caused by the tails in the direction x. Let us now analyze this phenomenon analytically.

In a continuous setting, angle compounding corresponds to setting

$$s_\Theta^{\mathrm{ac}}(\mathbf{x}) = \frac{1}{2\Theta} \int_{-\Theta}^{\Theta} s_\theta(\mathbf{x})\, d\theta, \qquad \mathbf{x} \in \mathbb{R}^2_+. \tag{1.12}$$

Thus, by linearity, the corresponding PSF is given by

$$g_\Theta^{\mathrm{ac}}(\mathbf{x}, \mathbf{x}') = \frac{1}{2\Theta} \int_{-\Theta}^{\Theta} g_\theta(\mathbf{x}, \mathbf{x}')\, d\theta, \qquad \mathbf{x}, \mathbf{x}' \in \mathbb{R}^2_+. \tag{1.13}$$

Let us find a simple expression for g_Θ^{ac}. By using (1.8), we may write $g_\Theta^{\mathrm{ac}}(\mathbf{x}, \mathbf{x}') \approx \tilde{g}_\Theta^{\mathrm{ac}}(\mathbf{x} - \mathbf{x}')$, where $\tilde{g}_\Theta^{\mathrm{ac}}$ is given by $\tilde{g}_\Theta^{\mathrm{ac}}(\mathbf{x}) = \frac{1}{2\Theta} \int_{-\Theta}^{\Theta} \tilde{g}_\theta(\mathbf{x})\, d\theta$, so that the image may be expressed as

$$s_\Theta^{\mathrm{ac}}(\mathbf{x}) = (\tilde{g}_\Theta^{\mathrm{ac}} * n)(\mathbf{x}), \qquad \mathbf{x} \in \mathbb{R}^2_+. \tag{1.14}$$

Thus, in view of the approximation (1.10), we can write

$$\begin{aligned} \tilde{g}_\Theta^{\mathrm{ac}}(\mathbf{x}) &= -\frac{i\nu_0^2 F}{2\Theta} \int_{-\Theta}^{\Theta} \tilde{\chi}\left(2\nu_0 c_0^{-1} z\right) e^{4\pi i \nu_0 c_0^{-1} z} e^{2\pi i \nu_0 c_0^{-1} \theta x} \operatorname{sinc}(2\pi \nu_0 c_0^{-1} F x)\, d\theta \\ &= -i\nu_0^2 F \tilde{\chi}\left(2\nu_0 c_0^{-1} z\right) e^{2i\nu_0 c_0^{-1} z} \operatorname{sinc}(2\pi \nu_0 c_0^{-1} F x) \operatorname{sinc}(2\pi \nu_0 c_0^{-1} \Theta x). \end{aligned}$$

Therefore, we immediately obtain

$$\tilde{g}_\Theta^{\mathrm{ac}}(\mathbf{x}) = \tilde{g}_0(\mathbf{x}) \operatorname{sinc}(2\pi \nu_0 c_0^{-1} \Theta x), \qquad \mathbf{x} \in \mathbb{R}^2. \tag{1.15}$$

This expression shows that the PSF related to angle compounding is nothing else than the PSF related to the single angle imaging with $\theta = 0$ multiplied by $\operatorname{sinc}(2\pi \nu_0 c_0^{-1} \Theta x)$. Thus, for $\Theta = 0$ we recover $\tilde{g}_\theta$ for $\theta = 0$, as expected. However, for $\Theta > 0$, this PSF enjoys faster decay in the variable x. See Figure 1.6 for an illustration of g_Θ^{ac} and $\tilde{g}_\Theta^{\mathrm{ac}}$ and a comparison with g_θ and Figure 1.5d for an illustration of the Fourier transform of g_Θ^{ac}.

To sum up the main features of the static problem, we have shown that the recovered image may be written as $s_\Theta^{\mathrm{ac}} = \tilde{g}_\Theta^{\mathrm{ac}} * n$, where $\tilde{g}_\Theta^{\mathrm{ac}}$ is the PSF of the imaging system with measurements taken at multiple angles. The ultrafast imaging technique is based on obtaining many of these images over time, as we discuss in the next section.

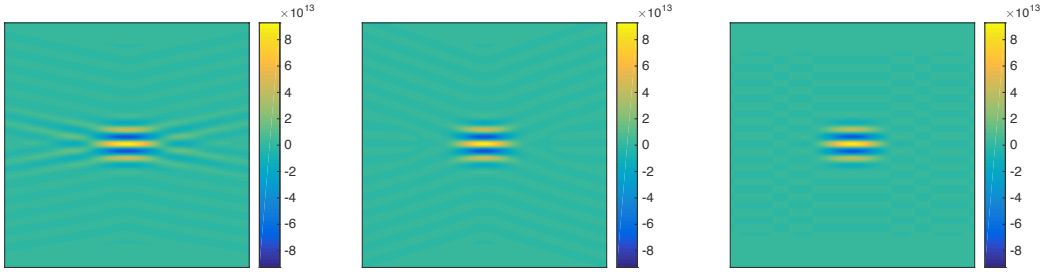

(a) The PSF g_θ with $\theta = 0$.

(b) The PSF g^{ac}_Θ with $\Theta = 0.25$.

(c) The PSF $\tilde{g}^{\mathrm{ac}}_\Theta$ with $\Theta = 0.25$.

Figure 1.6: A comparison of the PSF related to the single illumination with the PSF associated to multiple angles (with parameters as in (1.1) and (1.2), and $F = 0.4$). The better focusing in the variable x for g^{ac}_Θ is evident, as well as the good approximation given by $\tilde{g}^{\mathrm{ac}}_\Theta$. The size of the square shown is $2\,\mathrm{mm} \times 2\,\mathrm{mm}$, and the horizontal and vertical axes are the x and z axes, respectively.

1.4 Conclusion

In this chapter, we have provided for the first time a detailed mathematical analysis of ultrafast ultrasound imaging. We have derived an approximate expression for the PSF of this imaging system, which allows for a detailed analysis of blood flow imaging in the next chapter.

Chapter 2

Blood Flow Imaging in Ultrafast Ultrasound

2.1 Introduction

In this chapter, we consider *dynamic imaging*, that is the ultrafast ultrasound imaging process described in the previous chapter is repeated many times, which gives several thousand images per second. In blood flow imaging, we are interested in locating blood vessels. One of the main issues lies in the removal of the clutter signal, typically the signal scattered from tissues, as it introduces major artifacts [14]. Ultrafast ultrasonography allows to overcome this issue, thanks to the very high frame rate. Temporal filters [12, 40, 39], based on high-pass filtering the data to remove clutter signals, have shown limited success in cases when the clutter and blood velocities are close (typically of the order of $10^{-2}\,\mathrm{m}\cdot\mathrm{s}^{-1}$), or even if the blood velocity is smaller than the clutter velocity. A spatio-temporal method based on the singular value decomposition (SVD) of the data was proposed in [23] to overcome this drawback, by exploiting the different spatial coherence of clutter and blood scatterers. Spatial coherence is understood as similar movement, in direction and speed, in large parts of the imaged zone. Tissue behaves with higher spatial coherence when compared to the blood flow, since large parts of the medium typically move in the same way, while blood flow is concentrated only in small vessels, which do not share necessarily the same movement direction and speed. This explains why spatial properties are crucial to perform the separation.

The analysis of the PSF provided in the previous chapter allows to study the Doppler effect, describing the dependence on the direction of the flow. Moreover, we consider a random model for the movement of blood cells,

which allows us to study and justify the SVD method for the separation of the blood signal from the clutter signal, leading to the reconstruction of the blood vessels' geometry. The analysis is based on the empirical study of the distribution of the singular values, which follows from the statistical properties of the relative data. We provide extensive numerical simulations, which illustrate and validate this approach.

This chapter is structured as follows. In Section 2.2 the dynamic forward problem is considered: we briefly discuss how the dynamic data are obtained and analyze the Doppler effect. In Section 2.3 we focus on the source separation to solve the dynamic inverse problem. We discuss the random model for the refractive index and the method based on the SVD decomposition of the data. In Section 2.4 numerical experiments are provided. Some concluding remarks and outlooks are presented in the final section.

2.2 The Forward Problem

2.2.1 The quasi-static approximation and the construction of the data

The dynamic imaging setup consists in the repetition of the static imaging method over time to acquire a collection of images of a medium in motion. We consider a quasi-static model: the whole process of obtaining one image, using the image compounding technique discussed in Subsection 1.3.3, is fast enough to consider the medium static, but collecting several images over time gives us a movie of the movement over time. In other words, there are two time scales: the fast one related to the propagation of the wave is considered instantaneous with respect to the slow one, related to the sequence of the images.

In view of this quasi-static approximation, from now on we neglect the time of the propagation of a single wave to obtain static imaging. The time t considered here is related to the slow time scale. In other words, by (1.14) at fixed time t we obtain a static image $s(\mathbf{x}, t)$ of the medium $n = n(\mathbf{x}, t)$, namely

$$s(\mathbf{x}, t) = \left(\tilde{g}_{\Theta}^{\mathrm{ac}} * n(\,\cdot\,, t)\right)(\mathbf{x}). \tag{2.1}$$

Repeating the process for $t \in [0, T]$ we obtain the movie $s(\mathbf{x}, t)$, which represents the main data we now need to process. As mentioned in the introduction, our aim is locating the blood vessels within the imaged area, by using the fact that $s(\mathbf{x}, t)$ will be strongly influenced by movements in n.

2.2.2 The Doppler effect

Measuring the medium speed is an available criterion to separate different sources; thus, we want to see the influence on the image of a single particle in movement, as by linearity the obtained conclusions naturally extend to a group of particles. For a single particle, we are interested in observing the generated Doppler effect in the reconstructed image, namely peaks in the Fourier transform away from zero.

Intuitively, Figure 1.5d shows that there is a clear difference in the movements depending on their orientation. We want to explore this difference in a more precise way. Let us consider $n(x,z,t) = \delta_{(0,vt)}(x,z)$, i.e. a single particle moving in the z direction with velocity v. The resulting image, as a function of time, is obtained via equations (1.15) and (2.1)

$$\begin{aligned} s(x,z,t) &\approx \int_{\mathbb{R}^2} \tilde{g}^{\mathrm{ac}}_{\Theta}(x-x',z-z')\delta_{(0,vt)}(x',z')dx'dz' \\ &= \tilde{g}^{\mathrm{ac}}_{\Theta}(x,z-vt) \\ &= \tilde{g}_0(x,z-vt)\mathrm{sinc}(2\pi\nu_0 c_0^{-1}\Theta x). \end{aligned}$$

Therefore, arguing as in (1.11), we obtain that the Fourier transform with respect to the time variable t of the image is given by

$$\begin{aligned} \mathcal{F}_t(s)(x,z,\xi) &\approx \int_{\mathbb{R}} \tilde{g}_0(x,z-vt)e^{-2\pi i\xi t}dt\ \mathrm{sinc}(2\pi\nu_0 c_0^{-1}\Theta x) \\ &= \frac{1}{v}e^{-2\pi i\frac{\xi z}{v}}\mathcal{F}_2(\tilde{g}_0)(x,-\frac{\xi}{v})\mathrm{sinc}(2\pi\nu_0 c_0^{-1}\Theta x), \end{aligned}$$

where $\mathcal{F}_2$ is the Fourier transform with respect to the variable z. Adopting approximation (1.10), we obtain

$$\begin{aligned} \mathcal{F}_t(s)(x,z,\xi) \approx & -\frac{1}{v}i\nu_0^2 F e^{-2\pi i\frac{\xi z}{v}}\mathrm{sinc}(2\pi\nu_0 c_0^{-1}\Theta x) \\ & \times \quad \mathrm{sinc}(2\pi\nu_0 c_0^{-1}Fx)\mathcal{F}(\tilde{\chi})\Big(\frac{-\xi}{2\nu_0 c_0^{-1}v}-1\Big). \end{aligned}$$

Given the shape of $\tilde{\chi}$, its Fourier transform has a maximum around 0, thus we can see a peak of $|\mathcal{F}_t(s)(x,z,\xi)|$ when ξ is around $-2\nu_0 c_0^{-1}v$, and so we have the Doppler effect.

In the case when the particle is moving parallel to the detector array, namely $n(x,z,t) = \delta_{(vt,0)}(x,z)$, following an analogous procedure as before, we obtain

$$s(x,z,t) \approx \tilde{g}_0(x-vt,z)\mathrm{sinc}(2\pi\nu_0 c_0^{-1}\Theta(x-vt)),$$

and applying the Fourier transform in time yields

$$\mathcal{F}_t(s)(x,z,\xi) \approx \frac{1}{v} e^{-2\pi i \frac{\xi x}{v}} \mathcal{F}(\tilde{g}_0(\cdot,z)\mathrm{sinc}(2\pi\nu_0 c_0^{-1}\Theta\cdot))(-\frac{\xi}{v}).$$

Using approximation (1.10), the convolution formula for the Fourier transform and the known transform of the sinc function, gives

$$\begin{aligned}\mathcal{F}_t(s)(x,z,\xi) \approx -i\frac{e^{-2\pi i\frac{\xi x}{v}}}{4\Theta v}\nu_0 c_0 \tilde{\chi}(2\nu_0 c_0^{-1} z) e^{4\pi i \nu_0 c_0^{-1} z} \\ \times (\mathbb{1}_{[-F,F]} * \mathbb{1}_{[-\Theta,\Theta]}) \left(-\frac{\xi}{v\nu_0 c_0^{-1}}\right).\end{aligned}$$

The convolution of these characteristic functions evaluated at η is equal to the length of interval $[-F+\eta, F+\eta] \cap [-\Theta, \Theta]$, because

$$\begin{aligned}(\mathbb{1}_{[-F,F]} * \mathbb{1}_{[-\Theta,\Theta]})(\eta) &= \int_{\mathbb{R}} \mathbb{1}_{[-F,F]}(\eta - s)\mathbb{1}_{[-\Theta,\Theta]}(s)ds \\ &= \int_{\mathbb{R}} \mathbb{1}_{[-F+\eta,F+\eta]}(s)\mathbb{1}_{[-\Theta,\Theta]}(s)ds.\end{aligned}$$

Since both intervals are centered at 0, this value is maximized for η (and thus ξ) around 0, like in the static case, and so the observed Doppler effect is very small.

These differences are fundamental to understand the capabilities of the method for blood flow imaging. This phenomenon will be experimentally verified in Section 2.4.

2.2.3 Multiple scatterer random model

We have seen the effect on the image $s(x,z,t)$ of a single moving particle. We now consider the more realistic case of a medium (either blood vessels or tissue) with a large number of particles in motion. This will allow to study the statistical properties of the resulting measurements.

We consider a rectangular domain $\Omega = (-L_x/2, L_x/2) \times (0, L_z)$, which consists in N point particles. Let us denote the location of particle k at time t by $a_k(t)$. In the most general case, each particle is subject to a dynamics

$$a_k(t) = \varphi_k(u_k, t), \qquad a_k(0) = u_k, \tag{2.2}$$

where $(u_k)_{k=1,\dots,N}$ are independent uniform random variables on Ω and $(\varphi_k)_{k=1,\dots,N}$ are independent and identically distributed stochastic flows: for instance, they can be the flows of a stochastic differential equation or the deterministic flows of a partial differential equation. Thus, the a_ks are independent and

identically distributed stochastic processes. In view of these considerations, we consider the medium given by

$$n(\mathbf{x},t)=\frac{C}{\sqrt{N}}\sum_{k=1}^{N}\delta_{a_k(t)}(\mathbf{x}), \tag{2.3}$$

where $C>0$ denotes the scattering intensity and $\frac{1}{\sqrt{N}}$ is the natural normalization factor in view of the central limit theorem.

To avoid minor issues from boundary effects, which are of no interest to us in the analysis of this problem, we assume the periodicity of the medium. In other words, we consider the periodization

$$n_p(\mathbf{x},t)=\sum_{\mathbf{l}\in\mathbb{Z}^2} n(\mathbf{x}+\mathbf{l}\cdot\mathbf{L},t), \tag{2.4}$$

where $\mathbf{L}=(L_x,L_z)$. Let $g(\mathbf{x}):=\sum_{\mathbf{l}\in\mathbb{Z}^2}\tilde{g}_\Theta^{\mathrm{ac}}(\mathbf{x}+\mathbf{l}\cdot\mathbf{L})$ be the periodic PSF, which is more convenient than $\tilde{g}_\Theta^{\mathrm{ac}}$ (given by (1.15)) for a Ω-periodic medium. The dynamic image s is then given by

$$s(\mathbf{x},t)=(\tilde{g}_\Theta^{\mathrm{ac}}*n_p(\cdot,t))(\mathbf{x})=(g*n(\cdot,t))(\mathbf{x})=\frac{C}{\sqrt{N}}\sum_{k=1}^{N}g(\mathbf{x}-a_k(t)).$$

Let us also assume for the sake of simplicity that, at every time t, $a_k(t)$ modulo Ω is a uniform random variable on Ω, namely

$$\mathbb{E}\sum_{\mathbf{l}\in\mathbb{Z}^2} w(a_k(t)+\mathbf{l}\cdot\mathbf{L})=|\Omega|^{-1}\int_{\mathbb{R}^2} w(\mathbf{y})\,d\mathbf{y},\qquad w\in L^1(\mathbb{R}^2). \tag{2.5}$$

As a simple but quite general example, it is worth noting that in the case when $a_k(t)=u_k+F(t)$, where $F(t)$ is any random process independent of u_k, the above equality is satisfied, since

$$\begin{aligned}\mathbb{E}\sum_{\mathbf{l}\in\mathbb{Z}^2} w(u_k+F(t)+\mathbf{l}\cdot\mathbf{L})&=|\Omega|^{-1}\mathbb{E}\sum_{\mathbf{l}\in\mathbb{Z}^2}\int_\Omega w(\mathbf{y}+F(t)+\mathbf{l}\cdot\mathbf{L})d\mathbf{y}\\&=|\Omega|^{-1}\int_{\mathbb{R}^2} w(\mathbf{y})\,d\mathbf{y},\end{aligned}$$

where the expectation in the first term is taken with respect to u_k and $F(t)$, while in the second term only with respect to $F(t)$.

We now wish to compute the expectation of the random variables present in the expression for $s(\mathbf{x},t)$. By (1.10) and (1.15), since $\tilde{g}_\Theta^{\mathrm{ac}}$ is a derivative of

a Schwartz function in the variable z, we have $\int_{\mathbb{R}^2} \tilde{g}_\Theta^{\mathrm{ac}}(\mathbf{y})d\mathbf{y} = 0$. Thus, by (2.5) the expected value may be easily computed as

$$\mathbb{E}\left(g\left(\mathbf{x} - a_k\left(t\right)\right)\right) = \mathbb{E}\sum_{\mathbf{l}\in\mathbb{Z}^2} \tilde{g}_\Theta^{\mathrm{ac}}(\mathbf{x}-a_k(t)+\mathbf{l}\cdot\mathbf{L}) = |\Omega|^{-1}\int_{\mathbb{R}^2} \tilde{g}_\Theta^{\mathrm{ac}}(\mathbf{y})d\mathbf{y} = 0. \quad (2.6)$$

Let $(\mathbf{x}_i)_{i=1,\dots,m_\mathbf{x}}$ and $(t_j)_{j=1,\dots,m_t}$ be the sampling locations and times respectively. The data may be collected in the Casorati matrix $S_N \in \mathbb{C}^{m_\mathbf{x}\times m_t}$ defined by

$$S_N(i,j) = s(\mathbf{x}_i, t_j).$$

By (2.6), according to the multivariate central limit theorem, the matrix S_N converges in distribution to a Gaussian complex matrix $S \in \mathbb{C}^{m_\mathbf{x}\times m_t}$, the distribution of which is entirely determined by the following correlations, for $i, i' = 1, \dots, m_\mathbf{x}$ and $j, j' = 1, \dots, m_t$

$$\begin{aligned}
&\mathbb{E}(S(i,j)) = 0,\\
&\mathrm{Cov}\left(S(i,j), S(i',j')\right) = C^2\mathbb{E}\left(g\left(\mathbf{x}_i - a_1\left(t_j\right)\right) g\left(\mathbf{x}_{i'} - a_1\left(t_{j'}\right)\right)\right), \quad (2.7)\\
&\mathrm{Cov}\left(S(i,j), \overline{S(i',j')}\right) = C^2\mathbb{E}\left(g\left(\mathbf{x}_i - a_1\left(t_j\right)\right)\overline{g\left(\mathbf{x}_{i'} - a_1\left(t_{j'}\right)\right)}\right). \quad (2.8)
\end{aligned}$$

More precisely, let $w \in \mathbb{C}^{m_\mathbf{x}m_t}$ be a column vector containing all the entries of S. Let $v \in \mathbb{C}^{2m_\mathbf{x}m_t}$ and $V \in \mathbb{C}^{2m_\mathbf{x}m_t\times 2m_\mathbf{x}m_t}$ be defined by

$$v = \left(w_1, \overline{w_1}, w_2, \overline{w_2}, ..., w_{m_\mathbf{x}m_t}, \overline{w_{m_\mathbf{x}m_t}}\right)^T \quad \text{and} \quad V = \mathbb{E}\left(v\overline{v}^T\right).$$

The covariance matrix V can be easily computed from (2.7) and (2.8). Then the probability density function f of v can be expressed as [15]:

$$f\left(v\right) = \frac{1}{\pi^{m_\mathbf{x}m_t}\det\left(V\right)^{\frac{1}{2}}}\exp\left(-\frac{1}{2}v^*V^{-1}v\right).$$

Moreover, it is possible to generate samples from this distribution: if X is a complex unit variance independent normal random vector, and if $\sqrt{V}$ is a square root of V, then $\sqrt{V}X$ is distributed like v. This allows for simulations of sample image sequences for a large number of particles with a complexity independent of the number of particles.

The analysis carried out here will allow us to study the distribution of the singular value of the matrix S, depending on the properties of the flows φ_k. This will be the key ingredient to justify the correct separation of blood and clutter signals by means of the singular value decomposition of the measurements.

2.3 The Inverse Problem: Source Separation

2.3.1 Formulation of the dynamic inverse problem

As explained in the introduction, the aim of the dynamic inverse problem is blood flow imaging. In other words, we are interested in locating blood vessels, possibly very small, within the medium. The main issue is that the signal $s(\mathbf{x}, t)$ is highly corrupted by clutter signal, namely the signal scattered from tissues. In the linearized regime we consider, we may write the refractive index n as the sum of a clutter component n_c and a blood component n_b, namely $n = n_c + n_b$. Blood is located only in small vessels in the medium, whereas clutter signal comes from everywhere: by (1.3), since blood vessels are smaller than the focusing height, even pixels located in blood vessels contain reflections coming from the tissue. Let us denote the location of blood vessels by $\Omega_b \subset \Omega$. The inverse problem is the following: can we recover Ω_b from the data $s(\mathbf{x}, t) = s_c(\mathbf{x}, t) + s_b(\mathbf{x}, t)$? Here, s_c and s_b are given by (2.1), with n replaced by n_c and n_b, respectively. In this section, we provide a quantitative analysis of the method described in [23] based on the singular value decomposition (SVD) of s.

2.3.2 The SVD algorithm

We now review the SVD algorithm presented in [23]. The Casorati matrix $S \in \mathbb{C}^{m_\mathbf{x} \times m_t}$ is defined as in previous section by

$$S(i, j) = s\left(\mathbf{x}_i, t_j\right), \qquad i \in \{1, ..., m_\mathbf{x}\}\,,\ j \in \{1, ..., m_t\}\,.$$

Without loss of generality, we further assume that $m_t \leq m_\mathbf{x}$. We remind the reader that the SVD of S is given by

$$S = \sum_{k=1}^{m_t} \sigma_k u_k \overline{v_k}^T,$$

where $(u_1, ..., u_{m_\mathbf{x}})$ and $(v_1, ..., v_{m_t})$ are orthonormal bases of $\mathbb{C}^{m_x}$ and $\mathbb{C}^{m_t}$, and $\sigma_1 \geq \sigma_2 \geq ... \geq \sigma_{m_t} \geq 0$. For any $K \geq 1$, $S_K = \sum_{k=1}^{K} \sigma_k u_k \overline{v_k}^T$ is the best rank K approximation of S in the Frobenius norm. The SVD is a well-known tool for denoising sequences of images, see for example [32]. The idea is that since singular values for the clutter signal are quickly decaying after a certain threshold, the best rank K approximation of S will contain most of the signal coming from the clutter, provided that K is large enough. This could be used to recover clutter data, by applying a "denoising" algorithm,

and keeping only S_K. But it can also be used to recover the blood location, by considering the "power Doppler"

$$\hat{S}_{b,K}(i) := \sum_{k=K+1}^{m_t} \sigma_k^2 |u_k|^2(i) = \sum_{j=1}^{m_t} |(S - S_K)(i,j)|^2, \qquad i \in \{1, ..., m_{\mathbf{x}}\}.$$

As we will show in the following subsection, clutter signal can be well approximated by a low-rank matrix. Therefore, S_K will contain most of the clutter signal for K large enough. In this case, even if the intensity of total blood reflection is small, $S - S_K$ will contain more signal coming from the blood than from the clutter and therefore high values of $\hat{S}_{b,K}(i)$ should be located in blood vessels.

Before presenting the justification of this method, let us briefly provide a heuristic motivation by considering the SVD of the continuous data given by

$$s(\mathbf{x}, t) = \sum_{k=1}^{\infty} \sigma_k u_k(\mathbf{x}) \overline{v_k}(t).$$

In other words, the dynamic data s is expressed as a sum of spatial components u_k moving with time profiles $\overline{v_k}$, with weights σ_k. Therefore, since the tissue movement has higher spatial coherence than the blood flow, we expect the first factors to contain the clutter signal, and the remainder to provide information about the blood location via the quantity $\hat{S}_{b,K}$.

2.3.3 Justification of the SVD in 1D

We will assume that the particles of the blood and of the clutter have independent dynamics described by (2.2)-(2.4). We add the subscripts b and c to indicate the dynamics of blood and clutter, respectively.

In this subsection, using the limit Gaussian model presented in §2.2.3, we present the statistics of the singular values in a simple 1D model. These are useful to understand the behavior of SVD filtering. The results of §2.2.3 allow to simulate large number of sample signals s, given that we can compute the covariance matrices (2.7) and (2.8). Since these matrices are very large, we restrict ourselves to the $1D$ case, so that all sampling locations $\mathbf{x}_i$ are located at $x = 0$, and are thus characterized by their depth z_i. We will therefore drop all references to x in the following. We also consider very simplified dynamics, which can be thought of as local descriptions of the global dynamics at work in the medium. Let $a_b = a_{1,b}$ and $a_c = a_{1,c}$ be the random variables for the dynamics of blood and clutter particles, respectively, as introduced in (2.2). The dynamics is modeled by a Brownian motion with drift, namely

$$a_\alpha(t) = u_\alpha + v_\alpha t + \sigma_\alpha B_t, \qquad \alpha \in \{b, c\}.$$

Here, u_α represents the position of the particle at time $t = 0$, and is uniformly distributed in $(0, L_\alpha)$, where $L_b \ll L_c$. The deterministic quantity v_α is the mean velocity of the particles. In order to take into account the random fluctuations of the particles in movement, we added a diffusion term $\sigma_\alpha B_t$, where B_t is a Brownian motion and σ_α^2 is a diffusion coefficient quantifying the variance of the fluctuations of the particle position relative to the mean trajectory. We also make the simplifying assumption that the diffusion terms are independent over different particles. More precisely, we have the following conditional expectation and variance:

$$\mathbb{E}\left(a_\alpha(t)|\, u_\alpha\right) = u_\alpha + v_\alpha t, \qquad \mathrm{Var}\left(a_\alpha(t)|\, u_\alpha\right) = t\sigma_\alpha^2.$$

The difference between clutter and blood dynamics is in the diffusion coefficient: in the case of clutter, since it is an elastic displacement, $\sigma_c^2 \approx 0$. For simplicity, from now on we set $\sigma_c = 0$. In the case of blood, which is modeled as a suspension of cells in a fluid, we have $\sigma_b^2 = \sigma^2 > 0$. This coefficient is expressed in $\mathrm{m^2 s^{-1}}$, and models the random diffusion in a fluid transporting red blood cells due to turbulence in the fluid dynamics and collisions between cells. In practice, σ^2 is much larger than the diffusion coefficient of microscopic particles in a static fluid, and depends on the velocity v_b [19]. As for the mean velocities, in the most extreme cases, v_b and v_c can be of the same order, even though most of the time $v_b > v_c$.

Let S_b and S_c denote the data matrix constructed in §2.2.3, related to blood and clutter signal, respectively. We now compute the covariance matrix V of S_α:

$$\begin{aligned}
\mathrm{Cov}(S_\alpha(i,j), S_\alpha(i',j')) &= C_\alpha^2 \mathbb{E}\left(g\left(z_i - a_\alpha(t_j)\right) g\left(z_{i'} - a_\alpha(t_{j'})\right)\right) \\
&= \frac{C_\alpha^2}{L} \mathbb{E} \int_0^L g\left(z_i - y - v_\alpha t_j - \sigma_\alpha v_\alpha B_{t_j}\right) \\
&\qquad \times g\big(z_{i'} - y - v_\alpha t_{j'} - \sigma_\alpha v_\alpha B_{t_{j'}}\big) dy \\
&= C_\alpha^2 \mathbb{E}\, C_{gg}\Big(z_i - z_{i'} + v_\alpha\big(t_{j'} - t_j + \sigma_\alpha(B_{t_{j'}} - B_{t_j})\big)\Big),
\end{aligned}$$

where $C_{gg}(z) = \frac{1}{L}\int_0^L g(y) g(z+y) dy$ and C_b and C_c denote the intensity of the blood and clutter signals, respectively. The expectation operator is taken over all possible positions u_α and all possible drifts B_{t_j} and $B_{t_{j'}}$ in the first line, and only over all drifts in the second and third lines. By standard properties of the Brownian motion, $B_{t_{j'}} - B_{t_j}$ is Gaussian distributed, of expected value 0 and variance $|t_j - t_{j'}|$ and so it has the same distribution as $B_{t_{j'} - t_j}$. Thus, in the case of the blood, we can write

$$\mathrm{Cov}\left(S_b(i,j), S_b(i',j')\right) = C_b^2 \mathbb{E}\, C_{gg}\big(z_i - z_{i'} + v_b(t_{j'} - t_j + \sigma_b B_{t_{j'} - t_j})\big).$$

Likewise,

$$\mathrm{Cov}\big(S_b(i,j), \overline{S_b(i',j')}\big) = C_b^2 \mathbb{E}\, C_{g\bar{g}}\big(z_i - z_{i'} + v_b(t_{j'} - t_j + \sigma_b B_{t_{j'}-t_j})\big),$$

where $C_{g\bar{g}}(z) = \frac{1}{L}\int_0^L g(y)\bar{g}(z+y)dy$. The tissue model is then given by $\sigma_c = 0$, and is therefore deterministic given the initial position. Thus

$$\begin{aligned}
\mathrm{Cov}\left(S_c(i,j), S_c(i',j')\right) &= C_c^2 C_{gg}\left(z_i - z_{i'} + v_c\left(t_{j'} - t_j\right)\right), \\
\mathrm{Cov}\big(S_c(i,j), \overline{S_c(i',j')}\big) &= C_c^2 C_{g\bar{g}}\left(z_i - z_{i'} + v_c\left(t_{j'} - t_j\right)\right).
\end{aligned}$$

On one hand, in the case of blood, since $C_{g\bar{g}}$ and C_{gg} are oscillating and with very small support (see Figures 2.1a and 2.1b), the integration done when taking the expectation in the blood case should yield small correlations as long as $|t_{j'} - t_j|$ is large enough. On the other hand, in the case of clutter, correlations will be high between the two signals as long as $z_i - z_{i'}$ and $v_c\left(t_j - t_{j'}\right)$ are of the same order and almost cancel out. This heuristic is confirmed by numerical experiments. In Figure 2.1c, we compare the clutter model and the blood model in one dimension: velocities are in the z direction, and we only consider points aligned on the z axis. As we can see, correlations are quickly decaying as we move away from $(0,0)$ in the case of blood. In the case of clutter, there are correlations at any times at the corresponding displaced locations.

Once the correlation matrix is computed, we can generate a large number of samples to study the distribution of the singular values in different cases. In Figure 2.2a, we compare the distribution in the two models (blood and clutter), using the Gaussian limit approximation for the simulations, with the same intensity for both models. A comparison with a white noise model with the same variance shows that blood and noise have approximately the same singular value distribution. On the contrary, the distribution of the singular values of clutter presents a much larger tail. A comparison of the distribution of the singular values for the clutter model at different velocities shows no real difference in the tail of the distribution (Figure 2.2b).

As a consequence, the clutter signal s_c is well approximated by a low rank matrix, and the blood signal can be thought of as if it were only noise. Therefore, the SVD method act as a denoising algorithm and extracts the clutter signal, according to the discussion in the previous subsection.

2.4 Numerical Experiments

In this section, we consider again a more realistic 2D model, given by (2.2). This framework will allow us to simulate generic blood flow imaging sequences

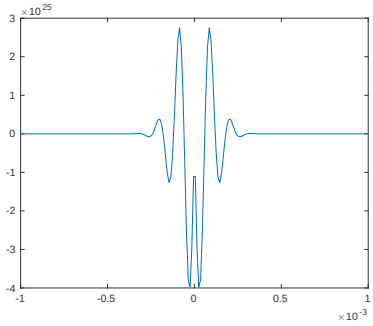

(a) The real part of C_{gg}.

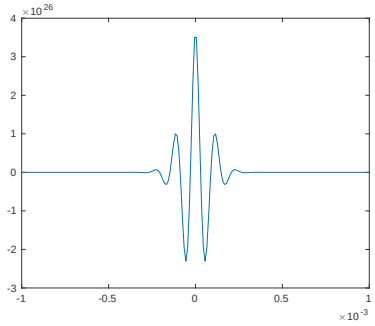

(b) The real part of $C_{g\bar{g}}$.

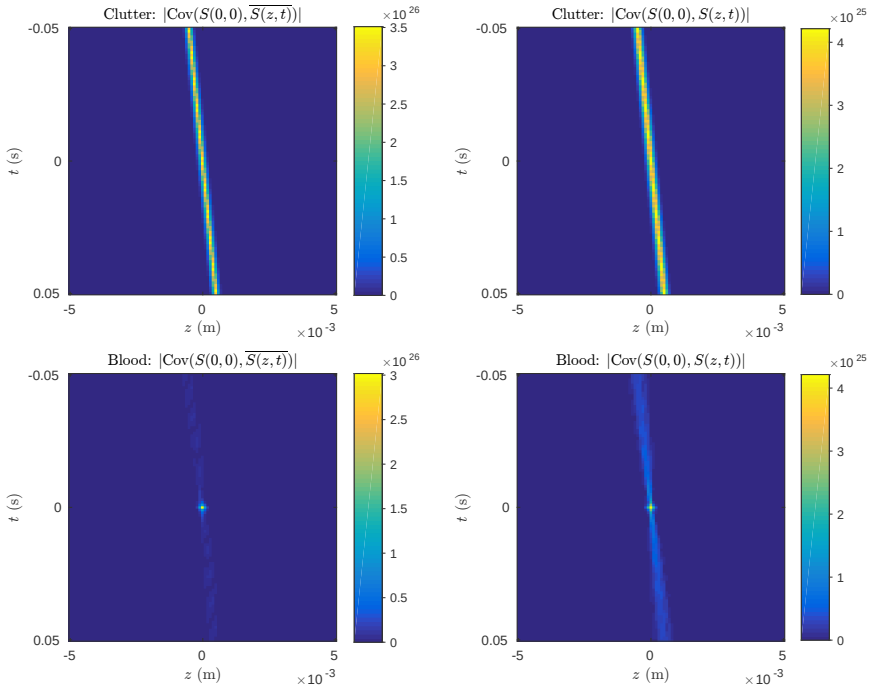

(c) Absolute values of the correlations in the clutter model ($\sigma = 0$, $v_c = 10^{-2}\,\mathrm{m{\cdot}s^{-1}}$) and in the blood model ($\sigma^2 = 10^{-6}\,\mathrm{m^2 s^{-1}}$, $v_b = 10^{-2}\,\mathrm{m{\cdot}s^{-1}}$).

Figure 2.1: Correlations of the Casorati matrix.

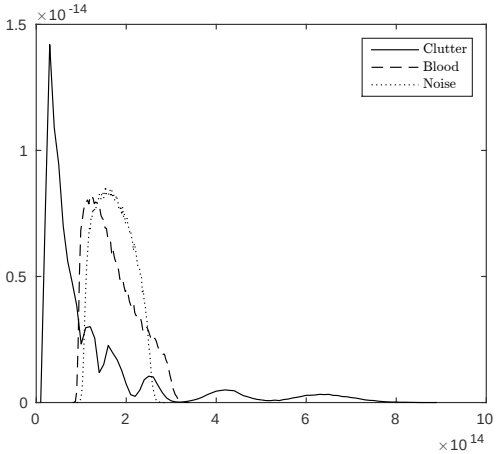

(a) The clutter model ($\sigma = 0$, $v_c = 10^{-2}\,\mathrm{m{\cdot}s^{-1}}$), the blood model ($\sigma^2 = 10^{-6}\,\mathrm{m^2 s^{-1}}$, $v_b = 10^{-2}\,\mathrm{m{\cdot}s^{-1}}$) and a white noise model with same variance as the blood.

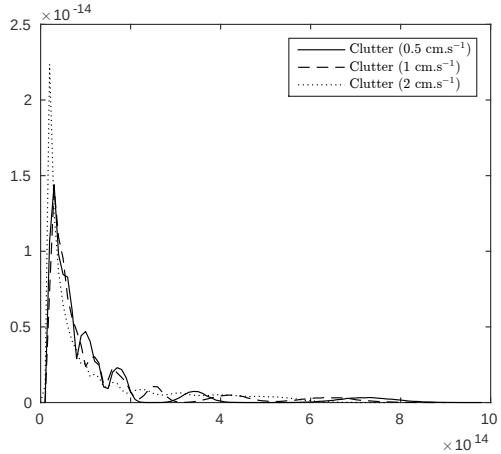

(b) The clutter model with different velocities.

Figure 2.2: The distribution of the singular values of the Casorati matrix S in different cases.

from particles. The dynamics of blood and clutter are modeled as follows. Let us assume that clutter is subject to a deterministic and computable flow φ_c. The randomness of the motion of red blood cells in vessels is modeled by a stochastic differential equation, given by

$$d\mathbf{y} = \mathbf{v}_b\,(t, y)\,dt + \sigma(y)\,dB_t, \tag{2.9}$$

where B_t is a two dimensional Brownian motion and σ is determined by the effective diffusion coefficient $K = \frac{1}{2}\sigma^2$. In blood vessels, this diffusion coefficient is proportional to the product $\dot{\gamma} r^2$ where $\dot{\gamma}$ is the shear stress in the vessel, and r is the radius of red blood cells. As in the previous section, let $a_c = a_{1,c}$ and $a_b = a_{1,b}$. Let φ_b be the flow associated to (2.9). We assume that φ_b represents the dynamics of blood particles, relative to overall clutter movement, so that

$$a_c\,(t) = \varphi_c\,(u_c, t)\,, \qquad \varphi_c(u_c, 0) = u_c, \tag{2.10}$$

and

$$a_b\,(t) = \varphi_c\,(\varphi_b\,(u_b, t)\,, t)\,, \qquad \varphi_b(u_b, 0) = u_b. \tag{2.11}$$

The dynamics of all the other particles are then taken to be independent realizations of the same dynamics. The velocity field $\mathbf{v}_b$ and the clutter

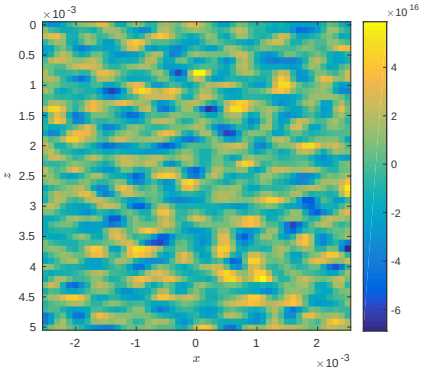

Figure 2.3: Single frame of ultrafast ultrasound (real part).

dynamics φ_c are computed beforehand and correspond to the general blood flow velocity and to an elastic displacement, respectively. In our experiments, we let φ_c be an affine displacement of the medium, changing over time: a global affine transformation, with slowly varying translation and shearing applied to the medium at each frame, namely

$$\varphi_c(u,t) = \begin{bmatrix} 1 & w_1(t) \\ 0 & 1 \end{bmatrix} u + \begin{bmatrix} w_2(t) \\ w_3(t) \end{bmatrix},$$

where w_i are smooth and slowly varying (compared to φ_b) functions such that $w_i(0) = 0$. As for the blood velocity flow $\mathbf{v}_b$, it is parallel to the blood vessels, with its intensity decreasing away from the center of the blood vessel [49, Section 11.3]. More precisely, $\mathbf{v}_b$ is a Poiseuille laminar flow, namely the mean blood flow velocity is half of the maximum velocity, which is the fluid velocity in the center of the vessel.

The relative blood displacements $b_{k,j} = \varphi_{k,b}(u_{b,k}, t_j)$ are computed according to the following discretization of the stochastic differential equation (2.9):

$$b_{k,j+1} = b_{k,j} + \delta t \mathbf{v}_b(t_j, b_{k,j}) + \sqrt{\delta t}\sigma(b_{k,j}) X_{k,j} + o(\delta t),$$

where $(X_{k,j})$ are centered independent Gaussian random variables and $\delta t = t_{j+1} - t_j$ is taken to be constant. The blood particle positions $a_{k,b}(t_j)$ are then computed simply by applying the precomputed flow φ_c.

In order to validate the SVD approach, we explore the effects of the blood velocity and of the direction of the blood vessels on the behavior of the singular values and on the quality of the reconstruction. In each case, the clutter displacement is the same composition of time-varying shearing and translation, and the mean clutter velocity is $1\,\mathrm{cm}\cdot\mathrm{s}^{-1}$. We choose $C_c = 5$ and $C_b = 1$, for the same density of scatterers from clutter and blood: per

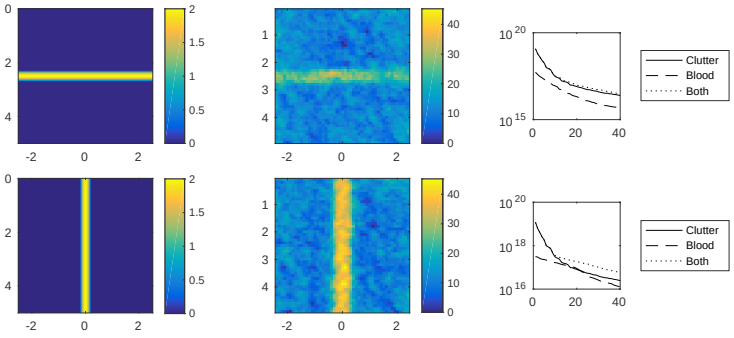

(a) Maximum blood velocity: $2\,\mathrm{cm}\cdot\mathrm{s}^{-1}$; mean clutter velocity: $1\,\mathrm{cm}\cdot\mathrm{s}^{-1}$.

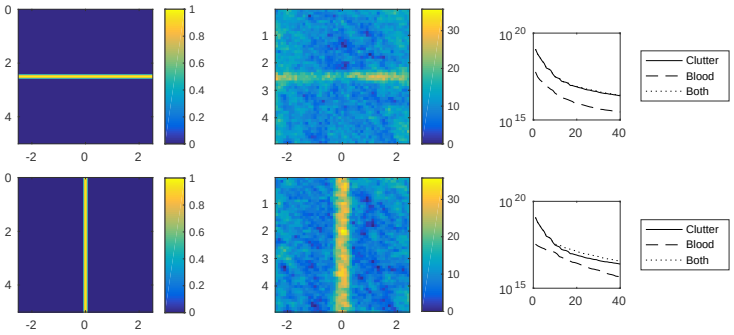

(b) Maximum blood velocity: $1\,\mathrm{cm}\cdot\mathrm{s}^{-1}$; mean clutter velocity: $1\,\mathrm{cm}\cdot\mathrm{s}^{-1}$.

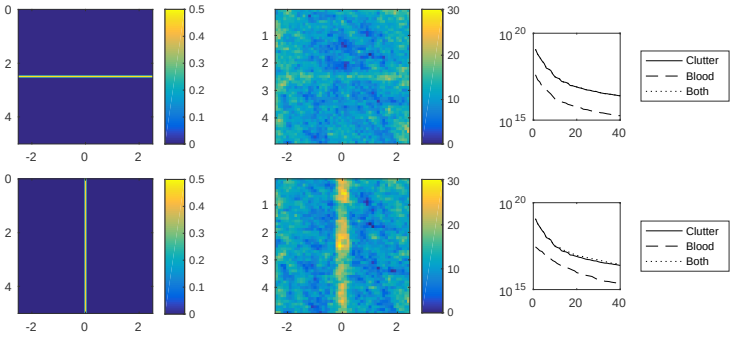

(c) Maximum blood velocity: $0.5\,\mathrm{cm}\cdot\mathrm{s}^{-1}$; mean clutter velocity: $1\,\mathrm{cm}\cdot\mathrm{s}^{-1}$.

Figure 2.4: The SVD method for different velocities and orientations. In each case, we have from left to right: the blood velocity and location, the reconstructed blood location, the decay of the singular values. The squares are $5\,\mathrm{mm} \times 5\,\mathrm{mm}$, and the horizontal and vertical axes are the x and z axes, respectively. The parameters used are those given in (1.1) and (1.2), $F = 0.4$ and $\Theta = 7$. The density of particles for both blood and clutter is 2,000 per mm^2, and $\sigma = 2.5 \cdot 10^{-5}$.

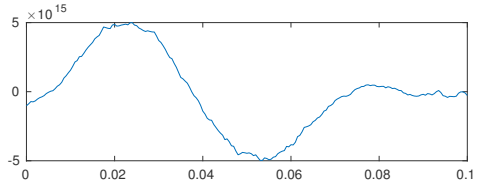

(a) Flow parallel to the receptor array.

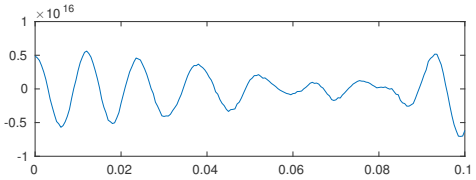

(b) Flow perpendicular to the receptor array.

Figure 2.5: Time behavior of a single pixel (real part), located in a constant velocity flow.

unit of area, the clutter intensity is therefore five times higher than the blood intensity. A single frame of ultrafast ultrasound imaging is presented in Figure 2.3: it is clear that without further processing, it is impossible to locate the blood vessels.

In Figure 2.4, the results for various velocities and orientations are presented. The reconstruction intensities are expressed in decibels, relatively to the smallest value in the image. The SVD method allows for reconstruction of blood vessels, even if the maximum blood velocity is close to, or oven lower than, the mean velocity of clutter. We always use the threshold $K = 20$. As we can see, due to the better resolution in the z direction discussed in Section 1.3, vessels oriented parallel to the receptor array have a reconstruction with a better resolution. But due to the oscillating behavior of the PSF in the z direction, and the low-pass filter behavior of the PSF in the x direction, the sensitivity is better for vessels oriented perpendicularly to the receptor array, and the SVD method is able to reconstruct smaller vessels with lower velocities. This follows from the discussion in Subsection 2.2.2. In order to visualize this phenomenon even better, Figure 2.5 presents the time behavior of a single pixel from the data of Figure 2.4c. We can clearly see the Doppler effect in the case when the flow is perpendicular to the receptor array, and the low frequency behavior of the signal in the case when it is parallel to the receptor array.

In Figure 2.6, results of an investigation on the effect of the threshold K on the reconstruction are presented. Except for K, the parameters of Figure 2.4b are used. If the threshold is too low, the reconstruction is not satisfactory and artifacts appear everywhere in the reconstructed image. If the threshold is too high, the reconstruction still works but the contrast becomes lower. With our parameters, $K = 20$ seems to produce the best results.

In order to further validate the method, we consider the impact of mea-

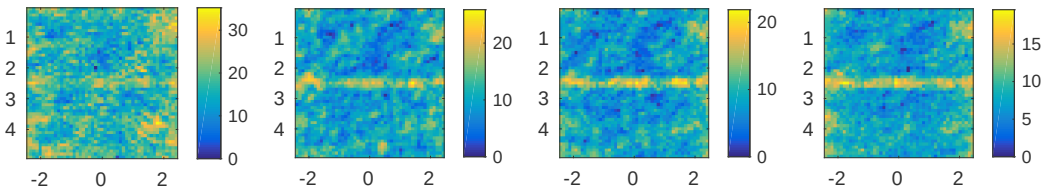

(a) Flow parallel to the receptor array.

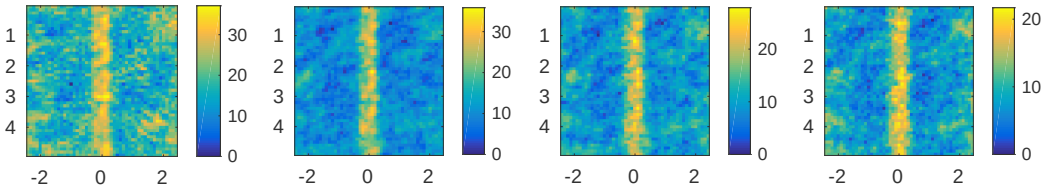

(b) Flow perpendicular to the receptor array.

Figure 2.6: Effect of the threshold K on the reconstruction. From left to right: $K = 10, 20, 30, 40$.

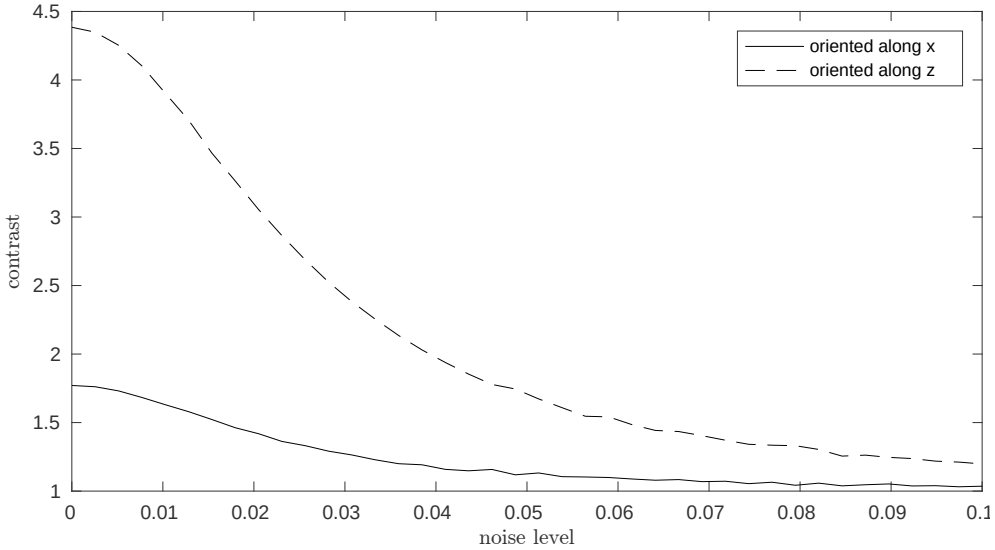

(a) Contrast as a function of noise level

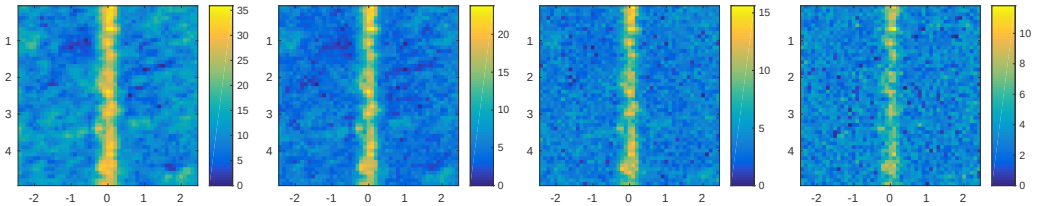

(b) 0% noise (c) 2.5% noise (d) 5% noise (e) 7.5% noise

Figure 2.7: Effect of noise on the reconstruction. The parameters are the same used in Figure 2.4b.

surement noise on the recovery. To this end, we add independent white Gaussian noise to the data, and consider the quality of the reconstruction as a function of the noise intensity. Let us define the contrast of the reconstruction as the ratio between the mean intensity of the reconstructed image inside and outside the blood domain. The parameters of Figure 2.4b are used. Blood intensity is five times lower than clutter intensity, and therefore a noise intensity of 10% corresponds to half the intensity of blood. In Figure 2.7, sample reconstructions at different noise levels are provided. We can conclude that contrast is robust to moderate levels of noise, since blood vessels can still be identified up to 7.5% of noise if they are oriented along the z axis, and up to 2.5% of noise if they are oriented along the x axis. Figure 2.7 also clearly quantifies the better contrast for vessels oriented along the z axis.

2.5 Conclusion

In this chapter, by using a random model for the movement of the blood cells, we have shown that a SVD approach can separate the blood signal from the clutter signal. Our model and results open a door for a mathematical and numerical framework for realizing super-resolution in dynamic optical coherence tomography [33], in ultrafast ultrasound imaging by tracking micro-bubbles [26], as well as in acousto-optic imaging based on the use of ultrasound plane waves instead of focused ones, which allows to increase the imaging rate drastically [37].

Chapter 3

Dynamic super-resolution

3.1 Introduction

The super-resolution problem is the following: given possibly noisy low frequency measurements of a medium – Fourier coefficients below a certain value, convolution by a low pass filter – is it possible to reconstruct the original medium with a precision which exceeds the diffraction limit? This problem is impossible in the general case, but there can be situations where it is indeed possible, with conditions on sparsity for example.

One possible mathematical formulation for the super-resolution problem can be the so called sparse spike reconstruction problem: let

$$\mu_0 = \sum_{i=1}^{N} \alpha_i \delta_{x_i}$$

be a complex measure with finite support defined on $\Omega \subset \mathbb{R}^d$. Let

$$\mathcal{F} : \mathcal{M}(\Omega) \to \mathbb{R}^n,$$

where $\mathcal{M}(\Omega)$ is the set of complex measures on Ω, be the measurement operator, so that the observed vector y is

$$y = \mathcal{F}\mu_0.$$

The super-resolution is then that of recovering the measure μ_0 given the measurements y. Since $\mathcal{M}(\Omega)$ is infinite dimensional, $\mathcal{F}$ is not injective, and therefore one has to use regularization to invert it. A common method for solving such sparse problems is to use an infinite dimensional variant of the Lasso program:

$$\hat{\mu} \in \operatorname{argmin}_\nu \|\nu\|_{\mathrm{TV}} \text{ such that } \mathcal{F}\nu = y. \tag{3.1}$$

Mathematical theory on the sparse spike recovery given low frequency measurements has been flourishing in the past years. It includes stable reconstruction of spikes with separation in one and multiple dimensions [18], robust recovery of positive spikes in the case of a Gaussian point spread function, with no condition of separation [11], exact reconstruction for positive spikes in a general settings in one dimension [22], with estimations on the stability [24].

The resolution of ultrafast ultrasound is determined by the wavelength of the incident wave, and by other factors such as the length of the receptor array and the range of angles used in angle compounding [3]. Due to diffraction theory, the minimum resolution one can obtain is of the order of half a wavelength, which is of the order of 300 nm. This implies that in imaging of small blood vessels, blood vessels separated by less than 300 nm cannot be distinguished.

Localization microscopy has been shown to surpass the diffraction limit in optical imaging [51], [31], and a similar technique has been proposed in ultrasound imaging [27], [25]. In ultrasound imaging, this method consists in using a contrast agent — micro-bubbles for example — which are randomly activated in blood vessels and produce very localized spikes in the observations. If separated by at least several wavelengths, using sparse recovery methods, it is possible to achieve sub-wavelength recovery of the position of particles.

This motivates the introduction of our dynamic model for super-resolution. Instead of considering a single measure μ_0, we consider a time-varying measure μ_t, where $t \in [-\delta, \delta]$. To simplify the problem, we assume that each point is moving with a constant velocity:

$$\mu_t = \sum_i^N \alpha_i \delta_{x_i + v_i t}, t \in [-\delta, \delta],$$

where $v_i \in \mathbb{R}^d$. The measurements vector is then composed of the measurements at discrete times $t_k = k\tau, k \in [-K, K]$, where $K\tau = \delta$:

$$y_k = \mathcal{F}\mu_{t_k}, k \in [-K, K].$$

In this work, we show that under certain conditions, we are able to recover simultaneously the positions x_i and the velocities v_i with infinite precision, using a sparse spike recovery based method. Figure 3.1 illustrates the idea of the method in the case of 2d particles and a convolution operator.

The chapter is organized as follows: first, we present theoretical results on the dynamic super-resolution problem. Second, we present numerical

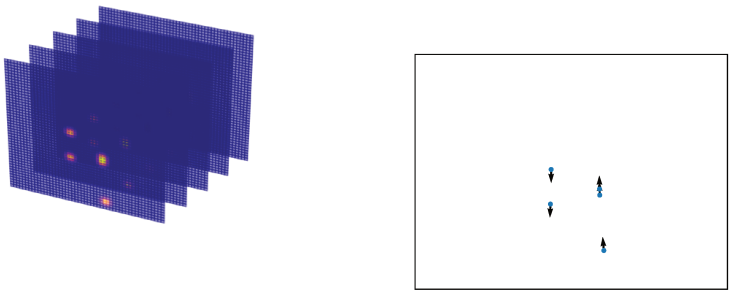

(a) (b)

Figure 3.1: Measurement sequence and reconstruction.

simulations which show that the method works in various cases. Then, we investigate applications to the ultrafast ultrasound imaging modality. We then conclude with a summary and open questions.

3.2 Theoretical results

3.2.1 The space-velocity model

In order to integrate the velocity in the recovery problem, we increase the dimension to $2d$ and consider the following complex measure:

$$\mu = \sum_{i=1}^{N} \alpha_i \delta_{x_i, v_i}.$$

We will assume that for all $i \in \{1, \dots, N\}$, $x_i \in \Omega_x$, $v_i \in \Omega_v$. We remind the reader that the measure μ_t is defined as the corresponding position of points at time t,

$$\mu_t = \sum_{i}^{N} \alpha_i \delta_{x_i + v_i t}, t \in [-\delta, \delta],$$

and that the measurements are done at times $t_k = k\tau, k \in [-K, K], k\tau = \delta$. Let us assume that the measurement operator $\mathcal{F}$ is defined as

$$\mathcal{F}\nu = \left(\langle \nu, \varphi_l \rangle\right)_{l=1}^{n}.$$

The functions φ_l are some test functions against which the measures $\mu_{t_k}, k \in \{-K, \dots, K\}$ are evaluated. In this case, let us consider

$$\varphi_{l,k}(x, v) = \varphi_l(x + t_k v),$$

and

$$\mathcal{G}\nu = \left(\langle \nu, \varphi_{l,k} \rangle\right)_{l,k}, \nu \in \mathcal{M}(\Omega_x \times \Omega_v).$$

In this case, the measurements $y = (y_k)_k$ where $y_k = \mathcal{F}\mu_{t_k}$ are given by

$$y = \mathcal{G}\mu.$$

This allows us to propose the following program to recover positions and velocities:

$$\hat{\mu} \in \operatorname{argmin}_\nu \|\nu\|_{\mathrm{TV}} \text{ such that } \mathcal{G}\nu = y. \tag{3.2}$$

We will call (3.2) the *dynamic* recovery, whereas (3.1) will be called the *static* recovery.

3.2.2 The perfect low-pass case

From now on to the end of this section, we consider the specific case of Fourier coefficients:

$$\begin{aligned} \Omega_x &= [0,1], \\ \Omega_v &= [-v_{\max}, v_{\max}], \\ \varphi_l(x) &= e^{-2\pi\langle x,l\rangle}, l \in \{-f_c, \dots, f_c\}^d. \end{aligned}$$

Analog to [18], a sufficient condition for the solution to (3.2) to be μ is that for any $\eta \in \mathbb{C}^N$ such that $|\eta| = 1, \forall j \in 1, \dots, N$, there exists a dual polynomial, called a dual certificate,

$$q(x,v) = \sum_{k=-K}^{K} \sum_{||l||_\infty \leq f_c} c_{k,l} e^{i2\pi l \cdot (x + k\tau v)}. \tag{3.3}$$

obeying:

$$\begin{cases} q(x_i, v_i) = \eta_j, & j \in \{1, \dots, N\} \\ q(x,v) < 1, & \text{everywhere else.} \end{cases} \tag{3.4}$$

Compared to the dual polynomials in the two dimensional case presented in [18], the only difference with our case, when $d = 1$, is in the allowed frequencies: whereas in the two dimensional case, all 2 dimensional low frequencies are allowed, here the only allowed frequencies are

$$\left\{(l^t, k\tau l^t), k = -K, \dots, K, ||l||_\infty \leq f_c\right\}.$$

The following proposition presents the uniqueness of the reconstruction in the case where we have uniqueness in more than 3 frames:

Proposition 1. *Let $\nu_i = \frac{\alpha_i}{|\alpha_i|}$. Assume that there exist m distinct time-steps, $m \geq 3$, $k_1, k_2, \ldots, k_m$ such that for all $p \in \{1, \ldots, m\}0$, there exist a trigonometric polynomial q_j defined on $\mathbb{R}^d$ with frequencies in $\{-f_c, \ldots, f_c\}^d$ such that*

$$\begin{cases} q_p(x_i + t_{k_p}\tau v_i) = \nu_j, & i \in \{1, \ldots, N\}, p \in \{1, \ldots, m\} \\ |q_j(x)| < 1, & \text{everywhere else.} \end{cases} \tag{3.5}$$

Moreover, assume that for any m distinct indices $i_1, i_2, \ldots, i_m \in \{1, \ldots, N\}$ such that $\eta_{i_p} = \eta_{i_q}$, for all p, q,

$$\bigcap_{p=i}^{m} \left\{(x, v) : (x - x_{i_p}) + k_p\tau(v - v_{i_p}) = 0\right\} = \emptyset. \tag{3.6}$$

Then the polynomial $q(x, v) = \frac{1}{m}\sum_{p=1}^{m} q_p(x + t_{k_p}\tau v)$ satisfies (3.3) and (3.4).

Proof. It is immediate that q defined as such verifies:

$$\begin{cases} q(x_i, v_i) = \nu_j, & i \in \{1, \ldots, N\} \\ |q(x, v)| \leq 1, & \text{everywhere.} \end{cases} \tag{3.7}$$

Moreover, let (x, v) be such that $|q(x, v)| = 1$. By the properties of q_j, this means that each of the terms in the sum must be equal and have modulus $1/m$. Therefore, there must exist $i_1, i_2, \ldots, i_m$ such that $\eta_{i_p} = \eta_{i_q}$ for all p, q and:

$$x + k_p\tau v = x_{i_p} + k_p\tau v_{i_p}, \text{ for all } p \in \{1, \ldots, m\}.$$

By (3.6), $i_1, i_2, \ldots, i_m$ cannot be distinct. Therefore, at least two are equal to some $j \in \{1, \ldots, N\}$ and we can conclude that $x = x_j$ and $v = v_j$. □

Geometrically, condition (3.6) ensures that there cannot be a virtual point hiding between a true point at each of the frames where there is separation. Numerical experiments show indeed that such situations produce instability in the reconstruction. Figure 3.2 illustrates the simplest of these situations: three points are static (their velocity is 0) and are equally spaced by Δ. In this case, two ghost points arise. One point at the position of the center point at $t = 0$ and with a velocity $v = \Delta/\tau$, this is the point illustrated in the figure. The other one is the symmetric with the same location but negative velocity.

There are also simple conditions that imply that the condition is always verified: if $m > n$ or if all α_is have a different phase. This simple result ensures that our proposed method works at least as well as what we call the static method, which consists in identifying the position of particles in each frame and then estimating their velocity. In the following proposition, we list a number of concrete cases where we can apply this result.

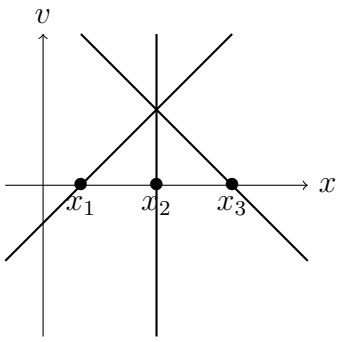

Figure 3.2: Geometry of ghost points

Proposition 2. *Assume that there exist m distinct time-steps, $m \geq 3$, $k_1, k_2, \ldots, k_m$ such that for all $p \in \{1, \ldots, m\}$, such that (3.6) hold and either:*

i) $d = 1$ or $d = 2$ and $\forall p \in \{1, \ldots, m\}, \forall i \neq j$

$$|x_i + t_{k_p} v_i - x_j - t_{k_p} v_j| > \frac{C}{f_c},$$

where $C = 2$ if $d = 1$ and $C = 2.38$ if $d = 2$.

ii) $d = 1$, $\alpha_i > 0, \forall i$ and the $x_i + t_{k_p} v_i$ are all distinct.

Then μ is the only solution to (3.2).

Proof. Condition i) comes from [18], condition ii) comes from [22]. □

3.3 Numerical simulations

3.3.1 Methods

Solving minimization problem (3.2) in all its generality is not an easy task. Indeed, it is not linear and infinite dimensional. It is possible to use an analog discrete problem, where the locations and velocities are fixed on a grid, whose size determines the resolution we want to obtain, and replacing the TV norm by a l_1 norm. However, this methods becomes intractable for a fine resolution. In [18], a continuous solution is obtained in the one dimensional case, however, its not trivial to adapt their algorithm to our method.

In this work, we propose to use a continuous reconstruction method. In [16], an algorithm is presented to solve the following problem:

$$\min_{\tilde{\mu}} \|\mathcal{F}\tilde{\mu} - Y\|_2^2 \quad \text{subject to } \|\tilde{\mu}\|_{TV} \leq M. \tag{3.8}$$

The proposed algorithm is limited to positive weights, but this is a realistic expectation in the case of physical signals. Let us assume that we can guess the value of $\|\mu\|_{TV}$ beforehand. Then we can set $M = \|\mu\|_{TV}$. In this setting, we have the following proposition:

Proposition 3. *Assume that μ is the unique solution of (3.2). Then μ is the unique solution of (3.8).*

Proof. Since (3.2) admits a unique minimizer, every $\tilde{\mu} \neq \mu$ such that $\mathcal{F}\tilde{\mu} = Y$ verifies $\|\tilde{\mu}\|_{TV} > K$. Therefore, $\tilde{\mu}$ is the unique minimizer of (3.8). □

In order to evaluate the numerical experiments, we introduce the super-resolution factor in space as follow:

$$\mathrm{SRF}_x = \frac{x_{\max}}{f_c \Delta_x}, \tag{3.9}$$

where $x_{\max}$ is such that $\Omega = [0, x_{\max}]$. In the case of velocity reconstruction, we introduce a super-resolution factor in velocity defined as:

$$\mathrm{SRF}_v = \frac{x_{\max}}{f_c \Delta_v \delta}. \tag{3.10}$$

3.3.2 1D Fourier examples.

We consider the perfect low-pass filter described in section 3.2. We consider a generic example where a number N of points are scattered in the medium with uniform and independent positions and velocities. The parameters for these simulations are the following:

$$\begin{aligned} f_c &= 20 \\ x_{\max} &= 1\mathrm{cm} \\ K &= 2 \\ \tau &= 1/60\mathrm{s}. \end{aligned} \tag{3.11}$$

The number of points in taken between 4 and 10 and their velocities are taken between $+$ and $-$ $\mathrm{cm.s}^{-1}$. We then realize this setup 1000 times and try to reconstruct using the minimization scheme described above.

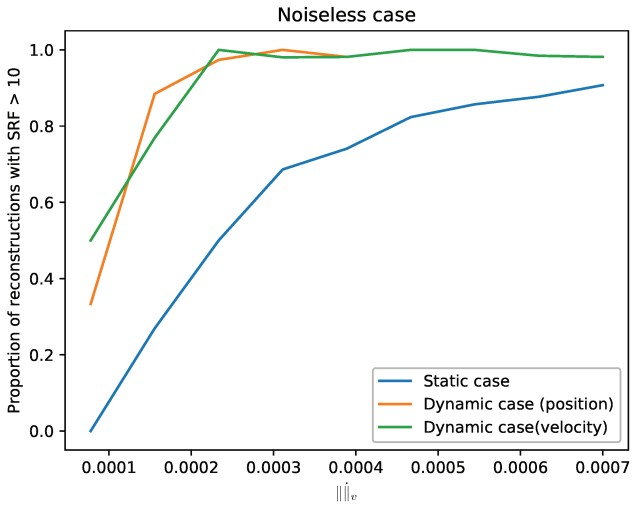

Figure 3.3: Noiseless recovery

Let us introduce the following norm:

$$\|(x,v)\|_v = |x| + 2\delta\,|v|\,. \tag{3.12}$$

In figure 3.3, the rate of correct reconstruction above a super-resolution factor of 10 is presented as a function of the norm (3.12). For comparison, the static case recovery rate is determined as the proportion of test cases where static recovery is possible in at least one of the 5 frames. Static recovery is therefore strictly worse than dynamic recovery in the sense that it does not necessarily allow reconstruction of the velocities. As figure 3.3 clearly shows, our method allows super-resoluted reconstruction of both position and velocity in more cases than the static method in the noiseless case.

In figure 3.4, the same results are presented but with various levels of measurement noise. Results indicate that our method is robust to noise, more so than the static method applied on a single frame.

Another factor of variability in the following: we have assumed that particles move in a straight line with constant velocity in the considered time window; in real life examples, velocity will not be strictly constant during the imaging frame. Therefore, we test our model against examples where the velocity is not constant. In figure 3.5, we present the rate of correct reconstruction as a function of curvature. This shows a moderate robustness to non linearity in the movement, with correct reconstructions obtained when there is a clear separation. These results show that there are many cases where proposition 1 is not optimal: indeed, the result assumes the existence

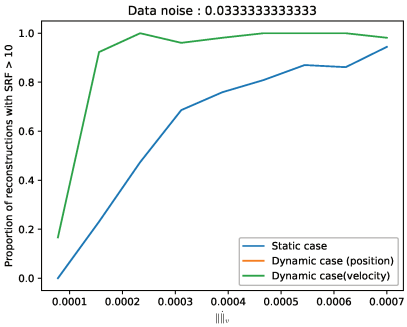

(a)

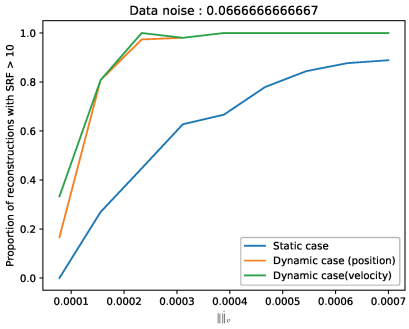

(b)

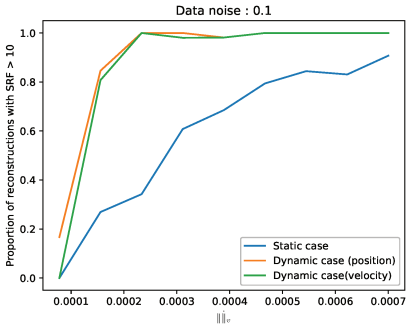

(c)

Figure 3.4: Robustness to noise

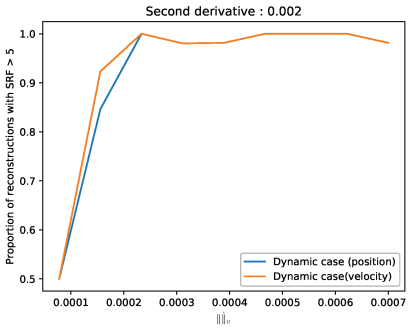

(a)

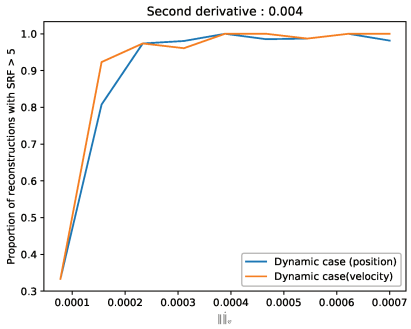

(b)

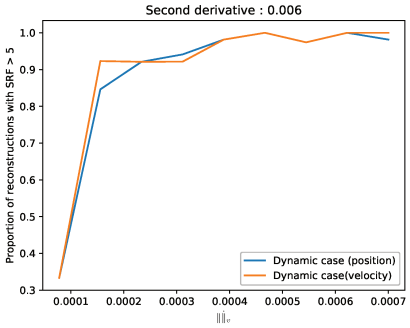

(c)

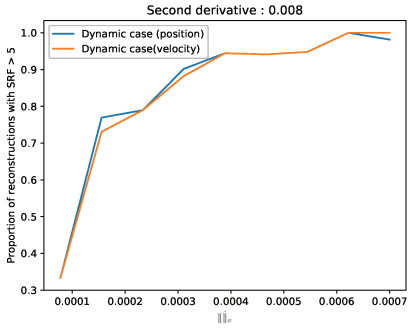

(d)

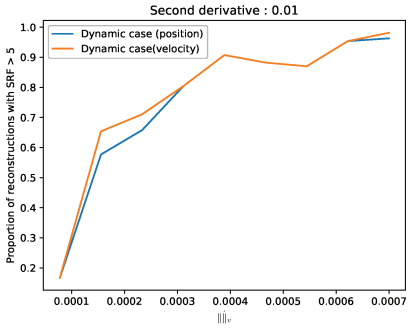

(e)

Figure 3.5: Robustness to curvature

of static frames where the reconstruction is correct, whereas numerical simulations show that dynamic reconstruction works in cases where the static reconstruction works in no single frame.

3.4 Applications to ultrafast ultrasound

This section is devoted to apply the described method to the case of blood flow imaging in ultrafast ultrasound (UFUS). The goal is to locate blood vessels and compute the velocity of blood inside them.

In the case of 2D UFUS with angle compounding, the point spread function is given up to a constant by

$$g(x,z) = \chi\left(2\nu_0 c_0^{-1} z\right) \exp\left(4i\pi\nu_0 c_0^{-1} z\right) \operatorname{sinc}\left(2\pi\nu_0 c_0^{-1} F x\right) \operatorname{sinc}\left(2\pi\nu_0 c_0^{-1}\Theta x\right),$$

where F, Θ are constants, ν_0 is the base pulsation, and χ is a smooth low-frequency function [3]. To remove high frequencies in measurements, we demodulate the signal by multiplying our measurements by $\exp\left(-4i\pi\nu_0 c_0^{-1} z\right)$. Therefore, if we sample our image at points $(x_l, z_l)_l$, the associated function φ_l are given by

$$\begin{aligned}\varphi_l(x,z) =& \chi\left(2\nu_0 c_0^{-1} z - z_l\right) \exp\left(4i\pi\nu_0 c_0^{-1} z\right) \times \\ & \operatorname{sinc}\left(2\pi\nu_0 c_0^{-1} F(x - x_l)\right) \operatorname{sinc}\left(2\pi\nu_0 c_0^{-1}\Theta(x - x_l)\right),\end{aligned} \tag{3.13}$$

Thanks to the Shannon sampling theorem, since the demodulated signal (3.13) has almost all its energy in low frequencies, the solution to the lasso minimization will be near the correct measure μ, as long as there is enough stability. This is the case when there is enough separation in the static images.

Figure 3.6 illustrates reconstruction in the case of an UFUS sequence on a small 2D patch.

3.5 Conclusion

In this chapter, we have shown that perfect reconstruction of positions and velocity is possible with low frequency measurements. We have proven that in the case where we have separation of the points in the static images, the minimization procedure exactly recovers positions and velocity. We have also shown that this procedure can be applied to ultrafast ultrasound imaging.

What remains to be done is to determine a tighter criterion to have perfect recovery, since numerical simulations show that reconstruction works even in the case where we have no separation in still images.

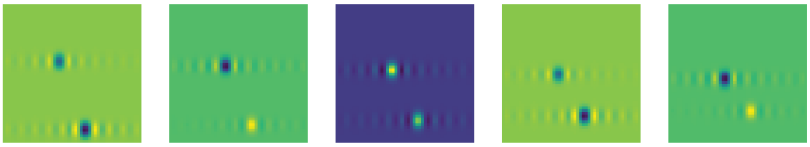

(a)

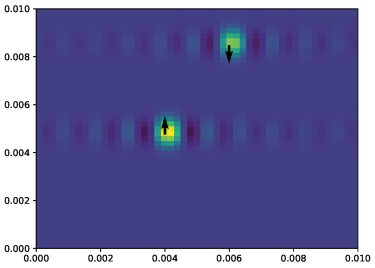

(b)

Figure 3.6: Reconstruction with UFUS PSF. On top: UFUS sequence, on bottom: reconstructed positions and velocities.

Chapter 4

Spectrography of cell cultures

4.1 Introduction

Cell culture production processes, such as those from stem cell therapy, must be monitored and controlled to meet strict functional requirements. For example, a cell culture of cartilage, designed to replace that in the knee, must be organized in a specific way.

Hyaline cartilage is located on the joint surface and play an important role in body movement. In normal articular cartilage, there is a depth-dependent stratified structure known as zonal organization. As a simplified model, cartilage comprises three different layers [42]: a superficial zone in outer 10%, a middle zone that is 50% of the height, and a deep zone consisting in the inner 40%. At the microscopic level, cartilage tissue is composed of cells, collagen fibers, and glycosaminoglycans (GAGs). The concentration and organization of each micro-structure differs among the three layers. In the superficial zone, cells are anisotropic and horizontally aligned, collagen orientation is also horizontal and GAGs have a lower concentration than in the other layers. In the middle zone, there are fewer cells and they are isotropic, collagen is randomly oriented and there is a medium concentration of GAGs. In the deep zone, cells are isotropic, cell density is higher than in the middle zone, collagen is vertically aligned and there is a high GAG density. As these parameters all contribute to the function of collagen in the knee, and must be replicated in the cell culture.

It is important that the method for monitoring cell cultures is non-destructive. Destructive methods require hundreds of samples to be cultured for a single functional tissue, and for the samples to be monitored multiple times during maturation. Here, we propose a microscopic electrical impedance tomography (micro-EIT) method for monitoring cell cultures

that exploits the distinctive dielectric properties of cells and other microstructures. In this method, electrodes inject a current into the medium at different frequencies and the corresponding dielectric potentials are recorded, thus enabling reconstruction of the microscopic parameters of the medium. The parameters of interest are cell density, collagen orientation, and GAG density, as well as the orientation and shape of cells.

EIT uses a low-frequency current (below 500 kHz) to visualize the internal impedance distribution of a conducting domain such as a tissue sample or the human body. Recent studies measured electrical conductivity values and anisotropy ratios of engineered cartilage to distinguish extracellular matrix samples containing differing amounts of collagen and GAGs. During chondrogenesis over a six-week period, these measurements could distinguish the stages of the process and provide information regarding the internal depth-dependent structure.

In this work, we provide a mathematical framework for determining the microscopic properties of the cell culture from spectral measurements of the effective conductivity. For simplicity, we consider a micro-structure comprising two components in a background medium. One of the components has a frequency dependent on the material parameters arising from the cell membrane structure, while the other has constant conductivity and permittivity over the frequency range. First, we derive in Theorem 4 the overall electrical properties of the culture, which depend on the volume fraction of each component and associated membrane polarization tensors defined by (4.10) and (4.11). Then, we show that the spectral measurements of the overall electrical properties of the culture can be used to determine the volume fraction of each component and the anisotropy ratio of the first component. For doing so, we study the dependence of the membrane polarization tensors on the operating frequency and use the spectral theorem to recover in Proposition 7 from the measurement of the effective conductivity on a range of frequencies the coefficients of its expansion with respect to the frequency. Proposition 7 also provides the anisotropy ratio of the cell culture.

This chapter is organized as follows: In Section 4.2, we present a simplified model of the tissue culture. In Section 4.3, we derive an equivalent effective conductivity for the solution at the macroscopic scale. In Section 4.4, we present a method based on spectral measurements, in which microscopic properties are measured from the effective conductivity. This process is known as inverse homogenization or dehomogenization. Finally, we provide some numerical examples to illustrate our main findings.

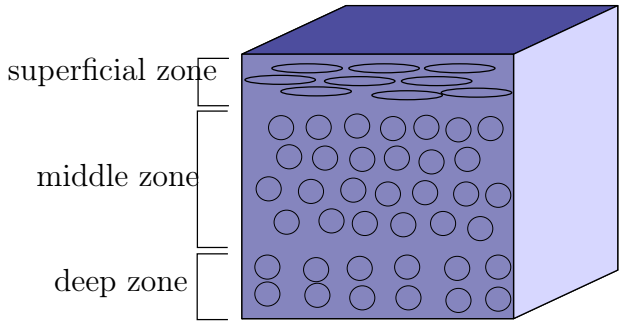

Figure 4.1: Organization of the cells in the cartilage tissue.

4.2 The direct problem

In this section, we propose a simple electrical model for the tissue and derive an effective conductivity using periodic homogenization.

4.2.1 Problem setting

We consider the domain of interest - the cell culture - to be described by a domain $\Omega \subset \mathbb{R}^3$. We assume that $\Omega = D \times (0,1)$ where $D \subset \mathbb{R}^2$ denotes a floor of the culture medium. Following [43], we describe the conductivity of the medium by a scalar field

$$\sigma_{\omega,\varepsilon}(x) = \sigma_\omega\left(x, \frac{x}{\varepsilon}\right),$$

where ω denotes the angular frequency of the injected current, and $\varepsilon > 0$ is a small parameter representing the microscopic scale of the medium; σ is $1-$periodic in every direction in the second variable. Let us consider the following unit domain:

$$\mathcal{Y} = \left(-\frac{1}{2}; \frac{1}{2}\right)^d.$$

For a fixed x, $\sigma\left(x, \frac{x}{\varepsilon}\right)$ describes the conductivity in a single cartilage tissue with cell size ε at a location $x \in \Omega$. To have a complete model of the tissue, σ must describe the conductivity of both cells and of the other inclusions, i.e., collagen and GAGs. The biological fluid conductivity is noted k_0 and is assumed to be frequency independent. The cells are made of biological fluid enclosed in a very thin and very resistive membrane [6] of thickness $\varepsilon\delta$ for some small parameter $\delta > 0$. The conductivity of the membrane is frequency dependent and is noted $k_m(\omega)$. The cell shape varies slowly with the parameter $x \in \Omega$ compared to the micro-scale ε. The other inclusions

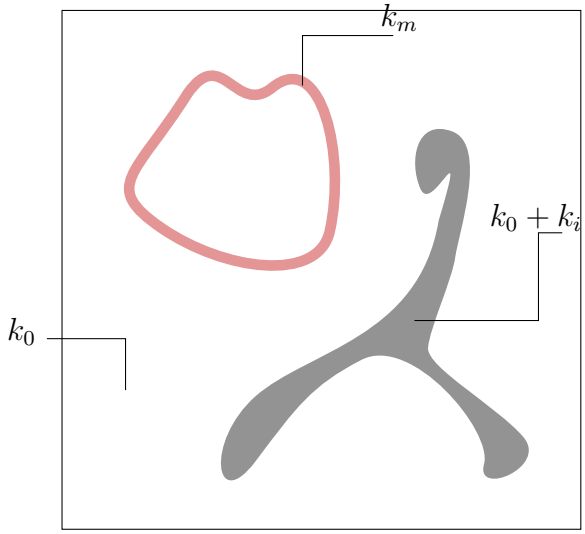

Figure 4.2: Typical values of σ_ω on $\mathcal{Y}$.

are described by some frequency independent conductivity function $k_i\left(x, \frac{x}{\varepsilon}\right)$. Let

$$\psi : \Omega \times \mathbb{R}^d :\to \mathbb{R}$$

be a $C^1\left(\Omega \times \mathbb{R}^d\right)$ function, 1-periodic in every direction with respect to the second variable. We assume that the function ψ is the level set function for the membrane boundary given by $\Omega_\varepsilon^+ = \left\{x : \psi\left(x, \frac{x}{\varepsilon}\right) > \delta\right\}$ (resp. $\Omega_\varepsilon^- = \left\{x : \psi\left(x, \frac{x}{\varepsilon}\right) < -\delta\right\}$). We also assume that the support of $k_i(x, y)$ is strictly included in $\{(x, y) : \psi(x, y) > \delta\}$. We can now describe the conductivity σ_ω, which is schematically represented at a fixed x in Figure 4.2:

$$\sigma_\omega(x, y) = \begin{cases} k_0 + k_i(x, y) & \text{if } \psi(x, y) > \delta, \\ k_0 & \text{if } \psi(x, y) < -\delta, \\ k_m(\omega) & \text{else.} \end{cases} \tag{4.1}$$

Now that we have an expression for the conductivity in the medium, as commonly accepted in EIT, we use the quasi-static approximation for the electrical potential. For an input current $g(x)\sin(\omega t)$ on the boundary $\partial\mathcal{Y}$, with $\int_{\partial\Omega} g = 0$, the real part of the corresponding time-harmonic potential, denoted by $u_{\omega,\varepsilon}$, satisfies the following problem approximately:

$$\begin{cases} \nabla \cdot \sigma_{\omega,\varepsilon} \nabla u_{\omega,\varepsilon} = 0 & \text{in } \Omega, \\ \sigma_{\omega,\varepsilon} \nabla u_{\omega,\varepsilon} \cdot \nu = g & \text{on } \partial\Omega. \end{cases} \tag{4.2}$$

where ν is the outer normal vector on $\partial\Omega$. Here, we impose the normalization $\int_{\Omega_\varepsilon} u_{\omega,\varepsilon} = 0$.

Remark 3. Let us briefly explain how the expression of σ_ω in (4.1) is derived. We should note that the frequency dependent behaviors of $\sigma_{\omega,\varepsilon}$ in (4.2) are attributed to thin cell membranes. Imagine that we inject an oscillating current at the angular frequency ω into the cube $\mathcal{Y}$. Then, the resulting time-harmonic potential $w = u + iv$ in $\mathcal{Y}$ is governed by

$$\nabla \cdot ((\sigma'(y) + i\omega\sigma''(y))\nabla w(y)) = 0 \quad \text{for} \quad y \in \mathcal{Y},$$

where σ' denotes the conductivity distribution and σ'' is the permittivity distribution in $\mathcal{Y}$. In [36], it was shown that, under some conditions on the membrane, the real part u approximately satisfies

$$\nabla \cdot \big(\frac{|\sigma' + i\omega\sigma''|^2}{\sigma'}\nabla u\big) = 0 \quad \text{in} \quad \mathcal{Y}. \tag{4.3}$$

Since $\sigma'' \ll \sigma'$ outside the membrane, we have

$$\frac{|\sigma' + i\omega\sigma''|^2}{\sigma'} \approx \sigma' \quad \text{outside the membrane.}$$

Hence, it is reasonable to assume that the conductivity outside the membrane, as a coefficient of the elliptic PDE (4.3), does not change with frequency. On the other hand, since σ' on the membrane is very small, the effect of σ'' is not negligible. Hence, the conductivity, k_m, on the membrane changes with frequency as follows:

$$\frac{|\sigma' + i\omega\sigma''|^2}{\sigma'} = \sigma' + \frac{\omega^2\sigma''}{\sigma'} \quad \text{on the membrane.}$$

4.2.2 Homogenization of the tissue

We are now interested in getting rid of the micro-scale oscillations of $\sigma_{\omega,\varepsilon}$, since boundary measurements will only allow us to image macro-scale variations of the conductivity. To this end, we proceed to the homogenization of equation (4.2). Assume that $k_0 + k_i$ is bounded from below and from above:

$$0 < \underline{\sigma} \leq k_0 + k_i \leq \overline{\sigma}.$$

From [6], we have two-scale convergence [4, 43, 45] of $u_{\omega,\varepsilon}$ to u_ω, which is a solution to

$$\begin{cases} \nabla \cdot \sigma^*_\omega \nabla u_\omega = 0 & \text{in } \Omega, \\ \sigma^*_\omega \nabla u_\omega \cdot \nu = g & \text{on } \partial\Omega, \\ \int_\Omega u_\omega = 0, \end{cases} \tag{4.4}$$

for an input current $g(x)\sin(\omega t)$ on the boundary $\partial\Omega$. Here, σ^*_ω is called the effective conductivity which can be represented by [6]

$$\begin{aligned}\sigma^*_\omega(x)e_p\cdot e_q &= \int_{\mathcal{Y}}\sigma_\omega(x,y)\nabla(y_p+v_p(y))\cdot e_q dy, \quad \forall p,q\in\{1,...,d\}\\ &= k_0\left(\delta_{p,q}+\int_{\partial\mathcal{Y}}\frac{\partial v_p}{\partial\nu}y_q\ ds(y)\right),\end{aligned} \tag{4.5}$$

where $e_p := (0,\cdots,1,\cdots,0)$ with 0 components except p-th component 1, and v_p is the solution to the following equation on $\mathcal{Y}$ for $p=1,...,d$:

$$\begin{cases}\nabla\cdot(\sigma_\omega(x,y)\nabla(v_p(y)+y_p))=0 & \text{for } y\in\mathcal{Y},\\ v_p & 1\text{-periodic},\\ \int_{\mathcal{Y}}(v_p(y)+y_p)dy=0.\end{cases} \tag{4.6}$$

As $\delta\to 0$, v_p can be approximated [35] by the solution of the following equation, where $\beta(\omega)=\frac{\delta}{k_m(\omega)}$:

$$\begin{cases}\nabla\cdot(\sigma_\omega(x,y)\nabla(v_p(y)+y_p))=0 & \text{for } y\in\mathcal{Y}\backslash\partial C,\\ k_0\frac{\partial}{\partial\nu}(v_p^+(y)+y_p)=k_0\frac{\partial}{\partial\nu}(v_p^-(y)+y_p) & \text{for } y\in\partial C,\\ v_p^+(y)-v_p^-(y)=\beta(\omega)k_0\frac{\partial}{\partial\nu}(v_p^+(y)+y_p) & \text{for } y\in\partial C,\\ v_p & 1\text{-periodic},\\ \int_{\mathcal{Y}}v_p(y)+ydy=0.\end{cases} \tag{4.7}$$

Here, ∂C denotes the membrane of the cell C and βk_0 is the effective thickness of the membrane.

4.3 Imaging the micro-structure from effective conductivity measurements

In this section, we do not care about the space dependence of σ^*_ω, and will therefore drop it. We will thus assume that σ^*_ω is constant equal to some matrix in $\mathcal{M}_d(\mathbb{C}) := \{m\in\mathbb{C}^{d\times d} \ : \ m_{i,j}=m_{j,i} \text{ for } i,j=1,2,\cdots,d\}$. We will show what kind of information on the micro-structure we can recover from the knowledge of σ^*_ω in a range of frequencies $\omega\in(\omega_1,\omega_2)$. First, in section 4.3.1, we will obtain a simple representation of the effective conductivity in the dilute case, where the volume fraction of both cells and other inclusions is small compared to the volume of biological fluid. Then, in the following sections we will use this representation and will show how to recover information about the micro-structure using the spectral measure.

4.3.1 Effective conductivity in the dilute case

Here, we consider some reference cell C_0 and some reference inclusion B_0 with there C^2 boundaries ∂C_0 and ∂B_0. We assume that $C = x_C + \rho_C C_0$ and $\beta(\omega) = \rho_C \beta_0(\omega)$ for some reference $\beta_0(\omega)$ and let $B = x_B + \rho_B B_0$, where x_C and x_B respectively indicate the locations of the cell and inclusion and ρ_C and ρ_B their characteristic sizes. We assume that the conductivity k_i of the inclusion is given by

$$k_i(y) = (k_0 - k_1)\chi_B(y),$$

where χ_B denotes the characteristic function of B.

The effective conductivity is therefore expressed as

$$\sigma^*_\omega e_p \cdot e_q = \int_{\mathcal{Y}} \sigma(y) \nabla (y_p + v_p(y)) \cdot e_q dy, \quad \forall p, q \in \{1, \cdots, d\},$$

where, for $p \in \{1, \cdots, d\}$,

$$\begin{cases} \nabla \cdot (k_0 \nabla (v_p(y) + y_p)) = 0 & \text{in } \mathcal{Y} \backslash (B \cup \partial C), \\ \nabla \cdot (k_1 \nabla (v_p(y) + y_p)) = 0 & \text{in } B, \\ k_0 \frac{\partial}{\partial \nu}(v_p^+(y) + y_p) = k_0 \frac{\partial}{\partial \nu}(v_p^-(y) + y_p) & \text{on } \partial C, \\ v_p^+ - v_p^- = \beta(\omega) k_0 \frac{\partial}{\partial \nu}(v_p^+(y) + y_p) & \text{on } \partial C, \\ v_p^+ - v_p^- = 0 & \text{on } \partial B, \\ k_0 \frac{\partial}{\partial \nu}(v_p^+(y) + y_p) = k_1 \frac{\partial}{\partial \nu}(v_p^-(y) + y_p) & \text{on } \partial B, \\ v_p & \text{periodic}, \\ \int_{\mathcal{Y}} (v_p(y) + y)\, dy = 0. \end{cases} \tag{4.8}$$

From now on, $\mathcal{I}$ denotes the inclusion map $H^{1/2}(\partial C) \to H^{-1/2}(\partial C)$, where $H^{1/2}$ and $H^{-1/2}$ are the Sobolev spaces of order $1/2$ and $-1/2$ on ∂C. We will now proceed to prove the following result.

Theorem 4. *Let $f_k = \rho_k^d$, $k \in \{B, C\}$ and $f = \max(f_B, f_C)$. Then we have the following expansion:*

$$\sigma^*_\omega = k_0 [I + f_B M_{B_0} + f_C M_{C_0}(\omega)] + o(f), \tag{4.9}$$

where

$$M_{C_0}(\omega) e_p \cdot e_q = \int_{\partial C_0} \nu_q(y) \left(\frac{1}{\beta_0(\omega) k_0} \mathcal{I} + \mathcal{L}_{\#, C_0} \right)^{-1} [\nu_p](y) ds(y), \tag{4.10}$$

and

$$M_{B_0} e_p \cdot e_q = \int_{\partial B_0} \left(\lambda I - \mathcal{K}^*_{\#, B_0} \right)^{-1} [\nu_p](y) y_q \, ds(y) \tag{4.11}$$

with

$$\lambda = \frac{k_1 + k_0}{2\left(k_1 - k_0\right)}.$$

We begin be reviewing properties of periodic layer potentials. Let us define the periodic Green's function

$$G_{\#}(x) = -\sum_{n \in \mathbb{Z}^d \backslash \{0\}} \frac{e^{2i\pi n \cdot x}}{4\pi^2 \left|n\right|^2}.$$

Thanks to Poisson's summation formula, in the sense of distribution, $G_{\#}$ satisfies

$$\Delta G_{\#}\left(x\right) = \sum_{n \in \mathbb{Z}^d} \delta(x-n) - 1. \tag{4.12}$$

We write $G_{\#}\left(x,y\right) := G_{\#}\left(x-y\right)$. Let us introduce the periodic single layer potential, for a Lipschitz domain $D \subset \mathcal{Y}$:

$$\begin{aligned} \mathcal{S}_{\#,D} : H^{-1/2}\left(\partial D\right) &\rightarrow H^1_{\text{loc}}\left(\mathbb{R}^d \backslash \partial D\right) \\ \varphi &\mapsto x \mapsto \int_{\partial D} G_{\#}\left(x,y\right)\varphi(y) ds(y), \end{aligned}$$

the periodic double layer potential

$$\begin{aligned} \mathcal{D}_{\#,D} : H^{1/2}\left(\partial D\right) &\rightarrow H^1_{\text{loc}}\left(\mathbb{R}^d \backslash \partial D\right) \\ \varphi &\mapsto x \mapsto \int_{\partial D} \frac{\partial G_{\#}}{\partial \nu(y)}\left(x,y\right)\varphi(y) ds(y), \end{aligned}$$

and the periodic Neumann-Poincaré operator

$$\begin{aligned} \mathcal{K}_{\#,D} : H^{1/2}\left(\partial D\right) &\rightarrow H^{1/2}\left(\partial D\right) \\ \varphi &\mapsto x \mapsto \int_{\partial D} \frac{\partial G_{\#}}{\partial \nu(y)}\left(x,y\right)\varphi(y) ds(y), \end{aligned}$$

and its adjoint given by

$$\begin{aligned} \mathcal{K}^*_{\#,D} : H^{-1/2}\left(\partial D\right) &\rightarrow H^{-1/2}\left(\partial D\right) \\ \varphi &\mapsto x \mapsto \int_{\partial D} \frac{\partial G_{\#}}{\partial \nu(x)}\left(x,y\right)\varphi(y) ds(y). \end{aligned}$$

We review the jump properties of the layer potentials [9].

Lemma 1. *We have the following jump relations along the boundary ∂D:*

$$\begin{aligned}
\mathcal{S}_{\#,D}[\varphi](x)|_+ &= \mathcal{S}_{\#,D}[\varphi](x)|_- , \\
\frac{\partial}{\partial\nu}\mathcal{S}_{\#,D}[\varphi](x)\Big|_\pm &= \left(\pm\frac{1}{2}I + \mathcal{K}^*_{\#,D}\right)[\varphi](x), \\
\mathcal{D}_{\#,D}[\varphi](x)|_\pm &= \left(\mp\frac{1}{2}I + \mathcal{K}_{\#,D}\right)[\varphi](x), \\
\frac{\partial}{\partial\nu}\mathcal{D}_{\#,D}[\varphi](x)\Big|_+ &= \frac{\partial}{\partial\nu}\mathcal{D}_{\#,D}[\varphi](x)\Big|_- .
\end{aligned}$$

where the subscript $\pm$ means $f_D(x)|_\pm = \lim_{t\to 0^+} f_D(x \pm t\nu(x))$ for $x \in \partial D$.

We denote by $\mathcal{L}_{\#,D}$ the operator $\varphi \mapsto \frac{\partial}{\partial\nu}\mathcal{D}_{\#,D}[\varphi]$. We write $\nu_p = \nu \cdot e_p$ on ∂B and ∂C. Using these jump relations, we have the following representation theorem for v_p, $p \in \{1, ..., d\}$.

Theorem 5. *We have the following representation for v_p:*

$$v_p = C_p + \mathcal{S}_{\#,B}[\varphi_{1,p}] - \mathcal{D}_{\#,C}[\varphi_{2,p}], \tag{4.13}$$

where C_p is a constant and (φ_1, φ_2) satisfies the following system:

$$\begin{cases} \left(\lambda I - \mathcal{K}^*_{\#,B}\right)[\varphi_{1,p}] + \frac{\partial}{\partial\nu}\mathcal{D}_{\#,C}[\varphi_{2,p}] = \nu_p & \text{on } \partial B, \\ \left(\frac{1}{\beta k_0}\mathcal{I} + \mathcal{L}_{\#,C}\right)[\varphi_{2,p}] - \frac{\partial}{\partial\nu}\mathcal{S}_{\#,B}[\varphi_{1,p}]\Big|_+ = \nu_p & \text{on } \partial C. \end{cases} \tag{4.14}$$

Lemma 2. *For any $(F, G) \in H^{-1/2}(\partial B) \times H^{-1/2}(\partial C)$, the system*

$$\begin{cases} \left(\lambda I - \mathcal{K}^*_{\#,B}\right)[\varphi_1] + \frac{\partial}{\partial\nu}\mathcal{D}_{\#,C}[\varphi_2] = F & \text{on } \partial B, \\ \left(\frac{1}{\beta k_0}\mathcal{I} + \mathcal{L}_{\#,C}\right)[\varphi_2] - \frac{\partial}{\partial\nu}\mathcal{S}_{\#,B}[\varphi_1]\Big|_+ = G & \text{on } \partial C, \end{cases}$$

admits a unique solution $(\varphi_1, \varphi_2) \in H^{-1/2}(\partial B) \times H^{1/2}(\partial C)$.

Proof. As shown in Appendix B, $\frac{1}{\beta}\mathcal{I} + \mathcal{L}_{\#,C}$ and $\lambda I - \mathcal{K}^*_{\#,B}$ are invertible for $\lambda \notin (-1/2, 1/2]$. Moreover, since

$$\frac{\partial}{\partial\nu}\mathcal{D}_{\#,C} : H^{1/2}(\partial C) \to H^{-1/2}(\partial B)$$

and

$$\frac{\partial}{\partial\nu}\mathcal{S}_{\#,B} : H^{-1/2}(\partial B) \to H^{-1/2}(\partial C)$$

are compact, the operator

$$\begin{aligned} H^{-1/2}(\partial\Omega)\times H^{1/2}(\partial\Omega) &\to H^{-1/2}(\partial\Omega)\times H^{-1/2}(\partial\Omega) \\ (\varphi_1,\varphi_2) &\mapsto \left(\left(\lambda I-\mathcal{K}^*_{\#,B}\right)[\varphi_1]-\frac{\partial}{\partial\nu}\mathcal{D}_{\#,C}[\varphi_2],\right. \\ &\qquad \left.\left(\frac{1}{\beta k_0}\mathcal{I}+\mathcal{L}_{\#,C}\right)[\varphi_2]-\frac{\partial}{\partial\nu}\mathcal{S}_{\#,B}[\varphi_1]\Big|_+\right) \end{aligned}$$

is a Fredholm operator. It is therefore sufficient to show that it is injective. Let (φ_1,φ_2) be such that

$$\begin{cases} \left(\lambda I-\mathcal{K}^*_{\#,B}\right)[\varphi_1]+\frac{\partial}{\partial\nu}\mathcal{D}_{\#,C}[\varphi_2]=0 & \text{on } \partial B, \\ \left(\frac{1}{\beta k_0}\mathcal{I}+\mathcal{L}_{\#,C}\right)[\varphi_2]-\frac{\partial}{\partial\nu}\mathcal{S}_{\#,B}[\varphi_1]=0 & \text{on } \partial C. \end{cases}$$

Let $v=\mathcal{S}_{\#,B}[\varphi_1]-\mathcal{D}_{\#,C}[\varphi_2]$. Then v is 1-periodic in every direction, and v is a solution by construction to the following problem:

$$\begin{cases} \nabla\cdot(k_0\nabla(v_p(y)+y))=0 & \text{for } y\in\mathcal{Y}\backslash(B\cup\partial C), \\ \nabla\cdot(k_1\nabla(v_p(y)+y))=0 & \text{for } y\in B, \\ k_0\frac{\partial}{\partial\nu}(v_p^+(y)+y)=k_0\frac{\partial}{\partial\nu}(v_p^-(y)+y) & \text{for } y\in\partial C, \\ v_p^+(y)-v_p^-(y)=\beta(\omega)\,k_0\frac{\partial}{\partial\nu}(v_p^+(y)+y) & \text{for } y\in\partial C, \\ v_p^+(y)-v_p^-(y)=0 & \text{for } y\in\partial B, \\ k_0\frac{\partial}{\partial\nu}(v_p^+(y)+y)=k_1\frac{\partial}{\partial\nu}(v_p^-(y)+y) & \text{for } y\in\partial B. \end{cases} \tag{4.15}$$

By the uniqueness of the solution to (4.15) up to a constant, $v(x)=c,\quad \forall x\in\mathcal{Y}$. Then, we have $\varphi_1=0$ on ∂C and $\varphi_2=0$ on ∂B because they are equal to the jumps of v (resp. $\frac{\partial v}{\partial\nu}$) across ∂B (resp. ∂C). This concludes the proof. □

We can now proceed to prove Theorem 5.

Proof. Let (φ_1,φ_2) be a solution of (4.14), and let

$$v_p=\mathcal{S}_{\#,B}[\varphi_1]-\mathcal{D}_{\#,C}[\varphi_2].$$

Then using the jump relations of the layer potentials, we have that v_p is a solution of (4.8), except that we have not necessarily $\int_{\partial\mathcal{Y}}v_p=0$. We just have to adjust C_p accordingly. □

We now proceed to compute the representation of the effective conductivity.

Theorem 6. *We have the following representation for σ_ω^*:*

$$\sigma_\omega^* = k_0 \left(I + M^* \right),$$

where $M^* = (M_{pq}^*)_{p,q=1}^d$ is defined by

$$(M^*)_{pq} = \int_{\partial B} x_p \varphi_{1,q} ds - \int_{\partial C} \nu_p \varphi_{2,q} ds, \quad \forall p, q \in \{1, ..., d\}.$$

Proof. We recall the expression of σ_ω^* in (4.5):

$$\sigma_\omega^* e_p \cdot e_q = k_0 \left(\delta_{p,q} + \int_{\partial \mathcal{Y}} \frac{\partial v_p}{\partial \nu}(y) y_q ds(y) \right).$$

Using representation (4.13), we obtain

$$\int_{\partial \mathcal{Y}} \frac{\partial v_p}{\partial \nu}(y) y_q ds(y) = \int_{\partial \mathcal{Y}} \frac{\partial \mathcal{S}_{\#,B}\left[\varphi_{1,p}\right]}{\partial \nu}(y) y_q ds(y) - \int_{\partial \mathcal{Y}} \frac{\partial \mathcal{D}_{\#,C}\left[\varphi_{2,p}\right]}{\partial \nu}(y) y_q ds(y)$$

and

$$\begin{aligned} \int_{\partial \mathcal{Y}} \frac{\partial \mathcal{S}_{\#,B}\left[\varphi_{1,p}\right]}{\partial \nu}(y) y_q ds(y) &= \int_{\partial B} \left. \frac{\partial \mathcal{S}_{\#,B}\left[\varphi_{1,p}\right]}{\partial \nu} \right|_+ (y) y_q ds(y) \\ &\quad - \int_{\partial B} \left. \frac{\partial \mathcal{S}_{\#,B}\left[\varphi_{1,p}\right]}{\partial \nu} \right|_- (y) y_q ds(y) \\ &= \int_{\partial B} y_q \varphi_{1,p}(y) ds(y). \end{aligned}$$

The same reasoning applies to the second part of the equation:

$$\begin{aligned} \int_{\partial \mathcal{Y}} \frac{\partial \mathcal{D}_{\#,C}\left[\varphi_{2,p}\right]}{\partial \nu}(y) y_q ds(y) &= \int_{\partial C} \mathcal{D}_{\#,C}\left[\varphi_{2,p}\right]|_+ (y) \nu_q(y) ds(y) \\ &\quad - \int_{\partial C} \mathcal{D}_{\#,C}\left[\varphi_{2,p}\right]|_- (y) \nu_q(y) ds(y) \\ &= \int_{\partial C} \varphi_{2,p}(y) \nu_q(y) ds(y). \end{aligned}$$

Therefore,

$$\begin{aligned} \sigma_\omega^* e_p \cdot e_q &= k_0 \left(\delta_{p,q} + \int_{\partial \mathcal{Y}} \frac{\partial v_p}{\partial \nu}(y) y_q ds(y) \right) \\ &= k_0 \left(\delta_{p,q} + \int_{\partial B} y_q \varphi_{1,p}(y) ds(y) - \int_{\partial C} \varphi_{2,p} \nu_q(y)(y) ds(y) \right). \end{aligned}$$

□

We turn to the proof of Theorem 4. We first review asymptotic properties of the periodic Green's function $G_\#$. The following result from [9, Chapter 2] holds.

Lemma 3. *We have the following expansion for $G_\#$:*

$$G_\#(x) = G(x) + R_d(x),$$

where G is the Green function and R_d is a smooth function on $\mathbb{R}^d$ and its Taylor expansion at 0 is given by

$$R_d(x) = R_d(0) - \frac{1}{2d}|x|^2 + O\left(|x|^4\right). \tag{4.16}$$

Using this expansion, we obtain by exactly the same arguments as those in [9, Chapter 8] the following expansion, which is uniform in $z \in \partial B_0$,

$$\begin{aligned}\left(\lambda I - \mathcal{K}_{B_0}^*\right)[\psi_{B,p}](z) &= \nu_{B_0,p}(z) + o(1)\\ \left(\frac{1}{\beta_0 k_0}\mathcal{I} + \mathcal{L}_{C_0}\right)[\psi_{C,p}](z) &= \nu_{C_0,p}(z) + o(1),\end{aligned}$$

where $\mathcal{K}_{B_0}^*$ is the standard Neumann-Poincaré operator and $\mathcal{L}_{C_0}$ denotes the operator $\frac{\partial}{\partial\nu}\mathcal{D}_{C_0}$ associated with the standard double layer potential $\mathcal{D}_{C_0}$:

$$\begin{aligned}\mathcal{K}_{B_0}^*[\phi](x) &:= \int_{\partial B_0}\frac{\partial G}{\partial\nu(x)}(x,y)\phi(y)ds(y),\\ \mathcal{L}_{C_0}[\phi](x) &:= \frac{\partial}{\partial\nu}\int_{\partial C_0}\frac{\partial G}{\partial\nu(y)}(x,y)\phi(y)ds(y).\end{aligned}$$

Therefore, we arrive at the result stated in Theorem 4.

4.3.2 Spectral measure of the tissue

Expansion (4.9) yields

$$\sigma_\omega^* = k_0\left[I + \rho_B^d M_{B_0} + \rho_C^d M_{C_0}(\omega)\right] + O\left(\rho^d\right)$$

with

$$M_{C_0}(\omega)e_p \cdot e_q = \int_{\partial C_0}\nu_q(y)\left(\frac{1}{\beta_0(\omega)k_0}\mathcal{I} + \mathcal{L}_{C_0}\right)^{-1}[\nu_p](y)\,ds(y).$$

In order to use the spectral theorem in a Hilbert space, we have to modify the expression of M_{C_0}. Let $\mathcal{L}_{C_0}^{-1}$ be the inverse of $\mathcal{L}_{C_0} : H_0^{1/2}(\partial C_0) \to H_0^{-1/2}(\partial C_0)$. Then we write

$$\left(\frac{1}{\beta_0(\omega)k_0}\mathcal{I} + \mathcal{L}_{C_0}\right)^{-1}[\nu_p] = \left(\frac{1}{\beta_0(\omega)k_0}\mathcal{L}_{C_0}^{-1}\circ\mathcal{I} + I_{H^{1/2}}\right)^{-1}\mathcal{L}_{C_0}^{-1}[\nu_p].$$

The following result holds.

Lemma 4. *$\mathcal{L}_{C_0}^{-1} \circ \mathcal{I}$ can be extended to a self-adjoint operator $\mathcal{L}^\dagger : L^2(\partial C_0) \to L^2(\partial C_0)$, whose image is a subset of $H^{1/2}(\partial C_0)$.*

Proof. Let $\mathcal{J}_1 : L^2(\partial C_0) \hookrightarrow H^{-1/2}(\partial C_0)$ and $\mathcal{J}_2 : H^{1/2}(\partial C_0) \hookrightarrow L^2(\partial C_0)$. Let $\mathcal{L}^\dagger = \mathcal{J}_2 \circ \mathcal{L}_{C_0}^{-1} \circ \mathcal{J}_1$. Then obviously $\mathcal{L}^\dagger$ extends $\mathcal{L}_{C_0}^{-1} \circ \mathcal{I}$ and its image is a subset of $H^{1/2}(\partial C_0)$. Let us show that it is self-adjoint. Let $(\varphi, \psi) \in L^2(\partial C_0) \times L^2(\partial C_0)$. Let $\langle\, ,\, \rangle_{L^2}$ and $\langle\, ,\, \rangle_{H^{1/2},H^{-1/2}}$ respectively denote the L^2-scalar product and the duality pairing between $H^{1/2}(\partial C_0)$ and $H^{-1/2}(\partial C_0)$. We have

$$\begin{aligned}\left\langle \mathcal{L}^\dagger[\varphi], \psi \right\rangle_{L^2} &= \left\langle \mathcal{L}_{C_0}^{-1}[\varphi], \psi \right\rangle_{L^2} = \left\langle \mathcal{L}_{C_0}^{-1}[\varphi], \psi \right\rangle_{H^{1/2},H^{-1/2}} \\ &= \left\langle \mathcal{L}_{C_0}^{-1}[\psi], \varphi \right\rangle_{H^{1/2},H^{-1/2}} = \left\langle \mathcal{L}_{C_0}^{-1}[\psi], \varphi \right\rangle_{L^2} = \left\langle \mathcal{L}^\dagger[\psi], \varphi \right\rangle_{L^2},\end{aligned}$$

since $\mathcal{L}_{C_0}$ is self-adjoint from $H^{1/2}(\partial C_0)$ onto $H^{-1/2}(\partial C_0)$. □

From this result, we can now proceed. From the spectral theorem, there exists a spectral measure E such that for any $z \in \mathbb{C} \setminus \Lambda\left(\mathcal{L}^\dagger\right)$ and for any $(\varphi, \psi) \in \left(L^2(\partial C_0)\right)^2$,

$$\left\langle \left(\frac{\mathcal{L}^\dagger}{z} + I \right)^{-1} [\varphi], \psi \right\rangle_{L^2} = \int_{\Lambda\left(\mathcal{L}^\dagger\right)} \frac{1}{\frac{x}{z} + 1} \varphi(x)\psi(x) dE(x). \tag{4.17}$$

where $\Lambda(\mathcal{L}^\dagger)$ denotes the spectrum of $\mathcal{L}^\dagger$. Let

$$F_{p,q}(z) = \delta_{p,q} + \rho_B^d M_{B_0} e_p \cdot e_q + \rho_C^d \int_{\Lambda\left(\mathcal{L}^\dagger\right)} \frac{1}{\frac{x}{z} + 1} \mathcal{L}_{C_0}^{-1}[\nu_p](x) \cdot \nu_q(x) dE(x). \tag{4.18}$$

where $\delta_{p,q} = 1$ if $p = q$ and $\delta_{p,q} = 0$ if $p \neq q$. Therefore, we have

$$\sigma_\omega^* e_p \cdot e_q \simeq k_0 \left[F_{p,q}(\beta_0(\omega) k_0) \right].$$

Since

$$\lim_{z \to 0} F(z) = I + \rho_B^d M_{B_0},$$

there is no singularity of F in 0. Since $0 \notin \Lambda\left(\mathcal{L}^\dagger\right)$, (4.17) is valid on a neighborhood of 0.

Proposition 7. *Let $F = (F_{p,q})_{p,q=1}^d$ be defined by (4.18). Then the following expansion of F in a neighborhood of 0 holds:*

$$F_{p,q}(z) = \sum_{k=0}^{\infty} a_{k,p,q} z^k, \tag{4.19}$$

where

$$a_{0,p,q} = I + \rho_B^d M_{B_0} e_p \cdot e_q,$$

and

$$a_{1,p,q} = \rho_C^d \nu_p \cdot \nu_q.$$

Proof. Identity (4.19) holds using the analyticity of F in a neighborhood of 0. We also have

$$a_{0,p,q} = \lim_{z\to 0} F_{p,q}(z) = \delta_{p,q} + \rho_B^d M_{B_0} e_p \cdot e_q.$$

In order to obtain the next coefficients, we begin by establishing the following limit:

$$\lim_{z\to 0} \left(\mathcal{L}^\dagger + zI\right)^{-1} [\nu_p] = \mathcal{L}_{C_0}[\nu_p], \quad p = 1, 2.$$

Indeed, let $\varphi(z) = \left(\mathcal{L}^\dagger + zI\right)^{-1} [\nu_p]$. Then

$$\varphi(z) = \frac{1}{z}\left(\nu_p - \mathcal{L}^\dagger \varphi_p\right).$$

Since the range of $\mathcal{L}^\dagger$ is a subset of $H^{1/2}(\partial C_0)$, $\varphi(z) \in H^{1/2}(\partial C_0)$. Therefore,

$$\varphi(z) = \mathcal{L}_{C_0}[\nu_p] - z\mathcal{L}_{C_0}[\varphi](z) \underset{z\to 0}{\to} \mathcal{L}_{C_0}[\nu_p].$$

This yields

$$\lim_{z\to 0} \frac{1}{z}\left(F_{p,q}(z) - F_{p,q}(0)\right) = \rho_C^d \nu_p \cdot \nu_q.$$

□

In the following, we write

$$F(z) = \left(F_{p,q}(z)\right)_{p,q\in\{1,\ldots,d\}}, z \in \mathbb{C}\backslash\Lambda\left(\mathcal{L}_{C_0}\right),$$

and

$$A_k = \left(a_{k,p,q}\right)_{p,q\in\{1,\ldots,d\}}, k \in \mathbb{N}. \tag{4.20}$$

Since $F_{p,q}$ is analytic on $\mathbb{C}\backslash\Lambda\left(\mathcal{L}_{C_0}\right)$, the values of a_k can be recovered from the values of $F_{p,q}$ on a subset of $\mathbb{C}$ with a limiting point. Therefore, we can reconstruct the values $a_{k,p,q}$ from the measurements of the effective conductivity σ_ω^* in a band of frequencies $\omega \in (\omega_1, \omega_2)$. Further details on this will be provided in the following section.

4.4 Inverse homogenization

4.4.1 Imaging of the anisotropy ratio

The anisotropy ratio (the ratio between the largest and the lowest eigenvalue of the effective conductivity tensor) depends on the frequency [6]. Furthermore, in the general case, the anisotropy orientation (the direction of the effective conductivity tensor eigenvectors) depends also on the frequency. However, in the special case where we have an axis of symmetry of a single inclusion or a cell, the anisotropy orientation is independent of the frequency.

We denote by $\mathcal{O}_d(\mathbb{R}) := \{R \in \mathbb{R}^{d\times d} \mid R^T R = 1, \det(R) = 1\}$ the set of rotational matrices. Here, the superscript T denotes the transpose. For convenience, we write $R(x) := Rx$ for $x \in \mathcal{Y}$ and $R(D) := \{Rx \ : \ x \in D\}$. We will need the following covariance result :

Lemma 5. *Let $R \in \mathcal{O}_d(\mathbb{R})$ and $f \in L^2(\partial C_0)$. Then*

$$\mathcal{L}_{C_0}[f \circ R] \circ R = \mathcal{L}_{C_0}[f].$$

Proof. We have, for any $x \in \partial C_0$,

$$\mathcal{L}_{C_0}[f \circ R](R(x)) = \lim_{h\to 0} \nabla \mathcal{D}_{C_0}[f \circ R](R(x) + h\nu(R(x))) \cdot \nu(R(x)).$$

Moreover,

$$\begin{aligned}\mathcal{D}_{C_0}[f \circ R](R(x)) &= \int_{\partial C_0} \nabla G(R(x) - y) \cdot \nu(y) f(R(y)) ds(y) \\ &= \int_{\partial C_0} \nabla G(R(x) - R(y)) \cdot \nu(R(y)) f(y) ds(y).\end{aligned}$$

Since G is isotropically symmetric, $\nabla G(R(x-y)) = R(\nabla G(x-y))$, therefore for any $x, y \in \partial C_0$,

$$\nabla G(R(x) - R(y)) \cdot \nu(R(y)) = R(\nabla G(x-y)) \cdot R(\nu(y)) = \nabla G(x-y) \cdot \nu(y)$$

so that

$$\mathcal{D}_{C_0}[f \circ R](R(x)) = \mathcal{D}_{C_0}[f](x), \quad \forall x \in \partial C_0.$$

This in turn implies that

$$\begin{aligned}\mathcal{L}_{C_0}[f \circ R](R(x)) &= \lim_{h\to 0} \nabla \mathcal{D}_{C_0}[f \circ R](R(x) + h\nu(R(x))) \cdot \nu(R(x)) \\ &= \lim_{h\to 0} \nabla \mathcal{D}_{C_0}[f](x + \nu(x)) \cdot \nu(x) = \mathcal{L}_{C_0}[f](x).\end{aligned}$$

□

The following corollary holds immediately.

Corollary 8. *Let $R \in \mathcal{O}_d(\mathbb{R})$. Then,*

$$M_{R(C_0)} = R M_{C_0} R^T.$$

Let us begin with the two-dimensional case.

Proposition 9. *Let $d = 2$, and $(\varepsilon_1, \varepsilon_2)$ be an orthonormal basis of $\mathbb{R}^2$. Let ξ be the orthogonal symmetry of axis ε_1. If $\xi(C_0) = C_0$, then*

$$F(z)\varepsilon_1 \cdot \varepsilon_2 = 0, \quad \forall z \in \mathbb{C} \setminus \Lambda(\mathcal{L}^\dagger).$$

Proof.

$$\begin{aligned} F(z)\varepsilon_1 \cdot \varepsilon_2 &= \rho_C^d \int_{\partial C_0} \left(\frac{\mathcal{L}^\dagger}{z} + I\right)^{-1} [\nu \cdot \varepsilon_1](x)\ \nu(x) \cdot \varepsilon_2\ ds(x) \\ &= \rho_C^d \int_{\partial C_0} \left(\frac{\mathcal{L}^\dagger}{z} + I\right)^{-1} [\nu \cdot \varepsilon_1](\xi(x))\ \nu(\xi(x)) \cdot \varepsilon_2\ ds(x) \\ &= -\rho_C^d \int_{\partial C_0} \left(\frac{\mathcal{L}^\dagger}{z} + I\right)^{-1} [\nu \cdot \varepsilon_1](x)\ \nu(x) \cdot \varepsilon_2\ ds(x) \end{aligned}$$

because $\nu(\xi(x)) \cdot \varepsilon_1 = \nu(x) \cdot \varepsilon_1$ and $\nu(\xi(x)) \cdot \varepsilon_2 = -\nu(x) \cdot \varepsilon_2$. Therefore,

$$F(z)\varepsilon_1 \cdot \varepsilon_2 = 0, \quad \forall z \in \mathbb{C} \setminus \Lambda(\mathcal{L}^\dagger).$$

□

We have a similar result in three dimensions. The following proposition holds.

Proposition 10. *Let $d = 3$, and $(\varepsilon_1, \varepsilon_2, \varepsilon_3)$ be an orthonormal basis of $\mathbb{R}^3$. Let ξ_1 (resp. ξ_2) be the orthogonal symmetry of axis ε_1 (resp. ε_2). If $\xi_1(C_0) = \xi_2(C_0) = C_0$, then*

$$F(z)\varepsilon_j \cdot \varepsilon_k = 0, \quad \forall z \in \mathbb{C}, \quad \forall k \neq j \in \{1, 2, 3\}.$$

Proof. The proof is exactly the same as in the $d = 2$ case and is therefore omitted. □

Remark 4. It is also true that the symmetry axes of B_0 correspond to the eigenvectors of the polarization tensor M_{B_0}. Therefore, the anisotropy direction of the frequency-independent background can also be recovered as the principal directions of M_{B_0}.

Remark 5. Even if each of inclusion and cell has an axis of symmetry, the direction of eigenvectors of the effective conductivity tensor can be frequency dependent. The following numerical test is conducted to show an example of frequency dependency. There are an ellipsoidal inclusion with major axis

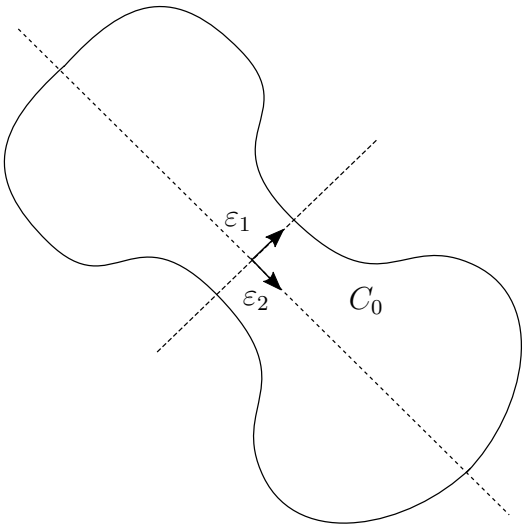

Figure 4.3: A domain presenting a symmetry. In this case, the anisotropy direction is frequency independent.

e_1 and minor axis e_2 and an ellipsoidal cell with major axis e_2 and minor axis e_1 in the unit square as shown in Figure 4.4 (a). For the square domain $\mathcal{Y} = (-\frac{1}{2}, \frac{1}{2})^2$, each axis length of cell and inclusion is 1/8, and 1/24. The center of ellipsoidal cell and inclusion are $(1/3, 1/6)$ and $(0, -1/3)$ respectively. The ratio between membrane thickness and size of a cell is 5×10^{-3}. The conductivity value of medium, membrane, inclusion are 0.5 S/m, 10^{-5} S/m, and 10^{-12} S/m respectively. We use (4.5) to compute the effective conductivity tensor. For the numerical computation, we take advantage of using u_j satisfying $\nabla \cdot (\sigma \nabla u_j) = 0$ in Ω with boundary condition $u_j(y)|_{\partial\Omega} = y_j|_{\partial\Omega}$ for $y = (y_1, y_2)$. Then, v_j can be replaced with $v_j = u_j - y_j$. Hence, the eigenvectors of the effective conductivity can be computed and the main direction of anisotropy changes in terms of the frequency as shown in Figure 4.4 (b).

4.4.2 Implementation of the inverse homogenization

Following [6], we use the following values:

- The size of cells: $50\mu m$;
- Ratio between membrane thickness and size of a cell: 0.7×10^{-3};
- Medium conductivity: $0.5\ S/m$;
- Membrane conductivity: $10^{-8}\ S/m$;

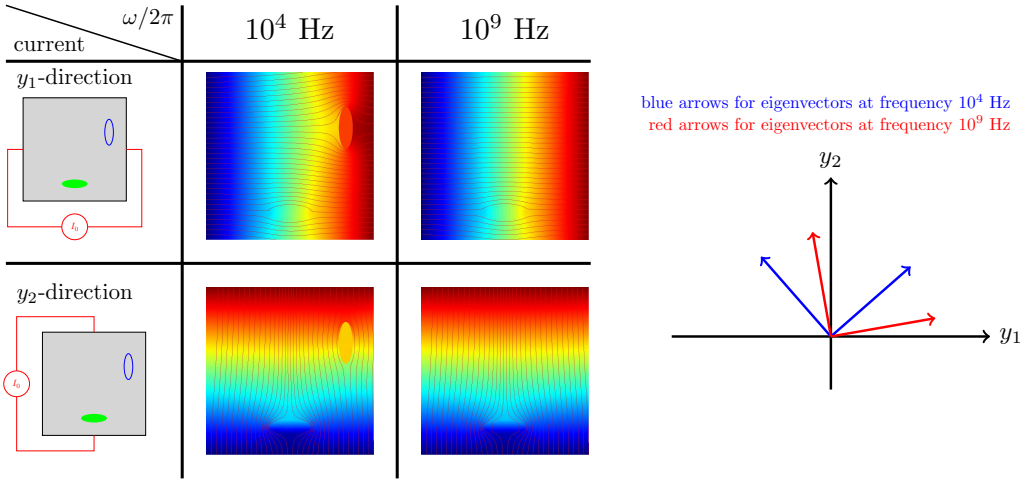

Figure 4.4: (a) shows voltage map with current flows for each y_1- and y_2- direction current at 10^4 and 10^9 Hz. (b) shows eigenvectors of the effective conductivity. Blue arrows represent eigenvectors at frequency $\omega/2\pi = 10^4$ Hz while red arrows are representing eigenvectors at frequency $\omega/2\pi = 10^9$ Hz.

- Background inclusion conductivity: 10^{-7} S/m;
- Membrane permittivity: $3.5 \times 8.85 \times 10^{-12}$ F/m;
- Frequency band: $\omega/2\pi \in [10^4; 10^9]$ Hz.

In this case, we have values of $\beta(\omega)$ for $\omega/2\pi \in [10^4;\ 10^9]$ in Figure 4.5. We consider a sample medium as follows: the cells are elliptic in shape, with axes lengths $\rho_C a_C$ and $\rho_C b_C$, with $a_c b_C \pi = 1$. The background is composed of elliptic inclusions, with axes lengths $\rho_B a_B$ and $\rho_B b_B$, with $a_B b_B \pi = 1$. Their orientation is given by the angles θ_C and θ_B respectively.

At each frequency, in order to compute the true effective conductivity given by (4.5), we perform a finite element computation using FreeFem++ [30]. Comparison between the true effective conductivity and the expansion from Theorem 4.9 can be seen in Figures 4.6 and 4.7, in the case $\theta_B = 0$ and $\theta_C = 0$, and $\rho_B = \rho_C = 0.1$.

To recover the moments from the effective conductivity, we approximate as a rational function,

$$F_{p,q}(z) \simeq \frac{p_0 + p_1 z + ... + p_N z^N}{q_0 + q_1 z + ... + q_N z^N}.$$

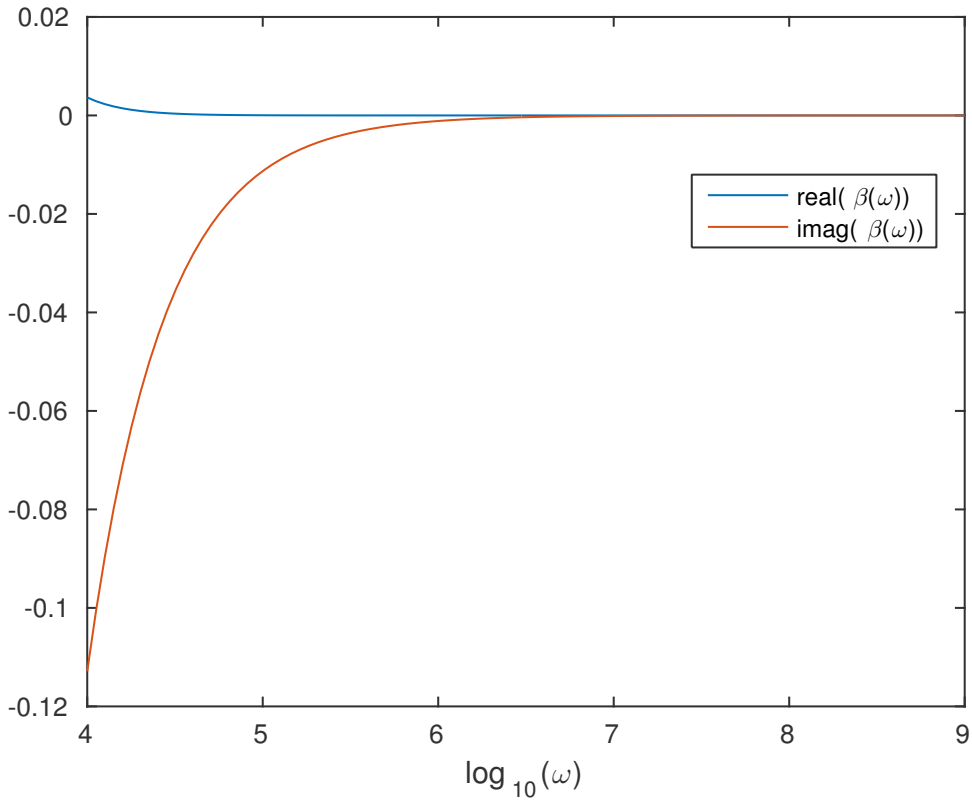

Figure 4.5: Values of $\beta(\omega)$ for $\omega/2\pi \in \left[10^4; 10^9\right]$.

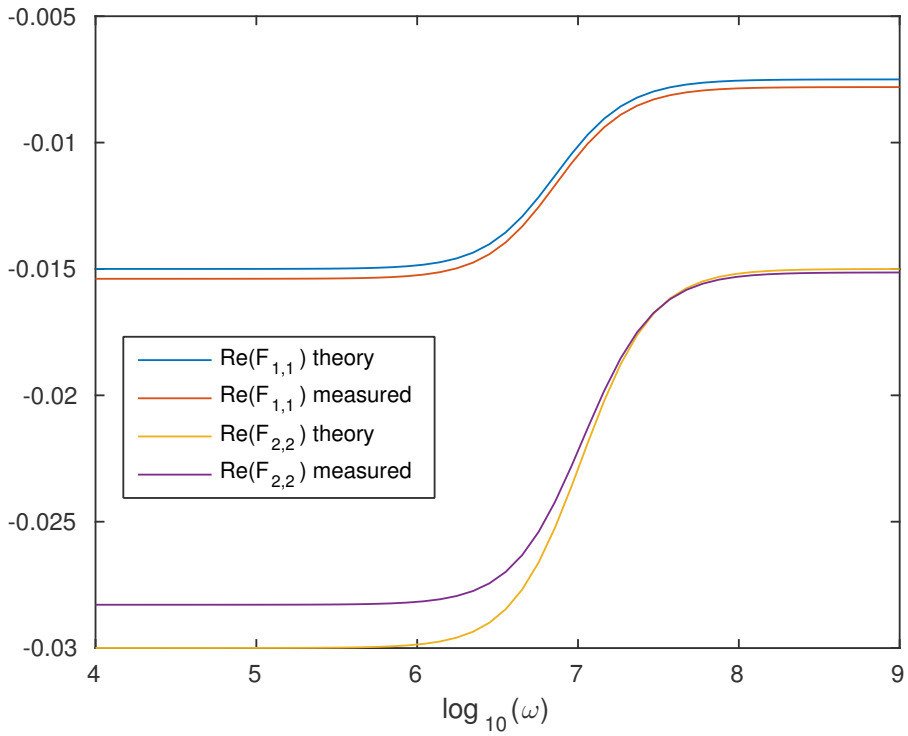

Figure 4.6: Real part of the effective conductivity.

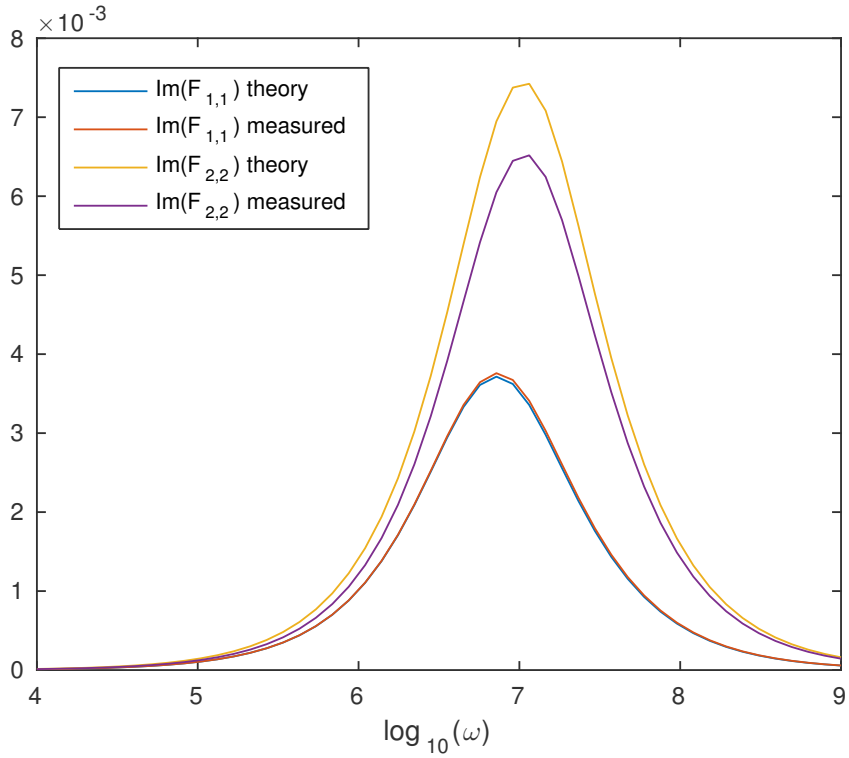

Figure 4.7: Imaginary part of the effective conductivity.

for some $N \in \mathbb{N}$. Such an approximation of F is called a Padé approximation of F. Then we approximate the moments by the following values:

$$\begin{aligned} \tilde{a}_{0,p,q} &= \frac{p_0}{q_0}, \\ \tilde{a}_{1,p,q} &= \frac{p_1}{q_0} - \frac{q_1 p_0}{q_0^2}. \end{aligned}$$

Numerically, this is done as a simple least square inversion: the coefficients of the polynomials $P(z) = p_0 + p_1 z + ... + p_N z^N$ and $Q(z) = q_0 + q_1 z + ... + q_N z^N$ are computed to minimize the quantity

$$\sum_{k=1}^{K} \left| F_{p,q}(z_k) - \frac{P(z_k)}{Q(z_k)} \right|^2,$$

where $z_1, ..., z_K$ are the frequency values where F is measured.

We now consider a toy example where C is an ellipse in $\mathbb{R}^2$. In this case, if λ_1 and λ_2 are the eigenvalues of A_1 defined by (4.20) for $k = 1$, the ratio $r := \lambda_2/\lambda_1$ is independent of the volume fraction and is given by

$$r = \frac{\int_0^{2\pi} \frac{b^2 \cos^2(t)}{\sqrt{b^2 \cos^2(t) + a^2 \sin^2(t)}} dt}{\int_0^{2\pi} \frac{a^2 \sin^2(t)}{\sqrt{b^2 \cos^2(t) + a^2 \sin^2(t)}} dt} = \frac{b}{a} \frac{\int_0^{2\pi} \frac{\cos^2(t)}{\sqrt{\cos^2(t) + \frac{a^2}{b^2} \sin^2(t)}} dt}{\int_0^{2\pi} \frac{\sin^2(t)}{\sqrt{\frac{b^2}{a^2} \cos^2(t) + \sin^2(t)}} dt}. \tag{4.21}$$

Since the right-hand side of (4.21) can be regarded as a function of a/b, the anisotropy ratio a/b can be easily obtained by solving (4.21) with the known value r. In Figure 4.8 (resp. in Figure 4.9), we illustrate the reconstruction of the ratio r using the Padé approximation of F as a function of the anisotropy ratio a/b compared to its theoretical value given by the preceding formula in the case where there is no inclusion B (resp. with an inclusion B with $\rho_B = 0.1$). As we can see, the reconstruction is almost perfect in the case where there is no inclusion, and there is a slight bias induced by the inclusion B.

After recovering the anisotropy ratio a/b, we can recover the volume fraction ρ_C from the product of λ_1, λ_2 of the eigenvalues of A_1. Indeed, we have

$$\begin{aligned} \lambda_1 \lambda_2 &= \rho_C^4 ab \int_0^{2\pi} \frac{\cos^2(t)}{\sqrt{\cos^2(t) + \frac{a^2}{b^2} \sin^2(t)}} dt \int_0^{2\pi} \frac{\sin^2(t)}{\sqrt{\frac{b^2}{a^2} \cos^2(t) + \sin^2(t)}} dt \\ &= \frac{\rho_C^4}{\pi} \int_0^{2\pi} \frac{\cos^2(t)}{\sqrt{\cos^2(t) + \frac{a^2}{b^2} \sin^2(t)}} dt \int_0^{2\pi} \frac{\sin^2(t)}{\sqrt{\frac{b^2}{a^2} \cos^2(t) + \sin^2(t)}} dt. \end{aligned}$$

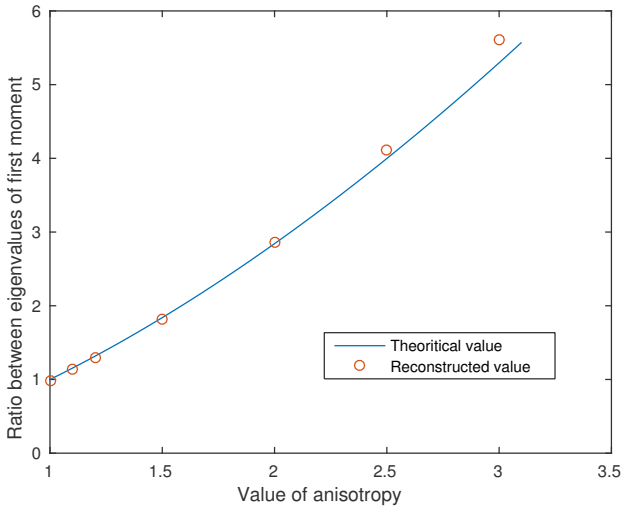

Figure 4.8: Reconstruction of r when there is no inclusion B.

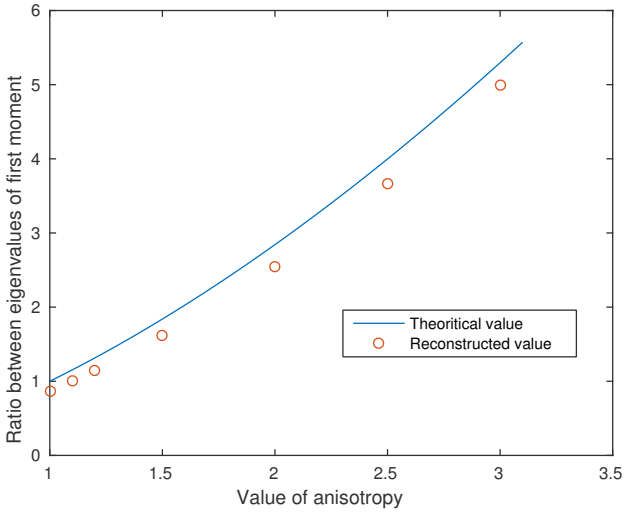

Figure 4.9: Reconstruction of r when there is an inclusion B with $\rho_B = 0.1$.

Values of ρ_C	0.01	0.02	0.03	0.05	0.1	0.2	0.3
Reconstructed	0.0098	0.0196	0.0294	0.0491	0.0981	0.1963	0.2945

Table 4.1: Reconstructed values of ρ_C with anisotropy ratio of 2.

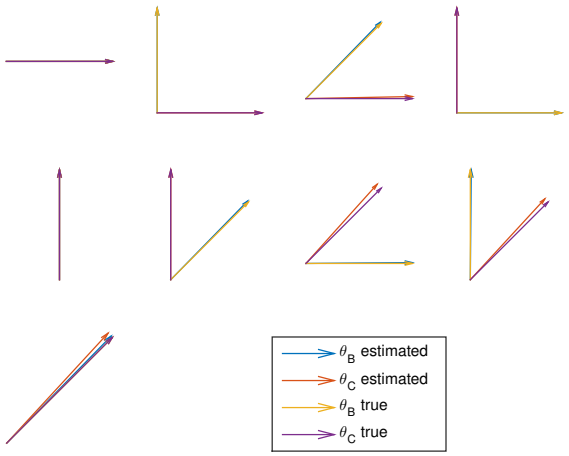

Figure 4.10: Reconstruction of the orientation of the inclusions B and C.

Table 4.1 presents numerical reconstruction of the volume fraction ρ_C using the preceding formula, with an anisotropy ratio equal to 2.

To reconstruct the angle of the inclusions, we simply use the orientation of the eigenvalues of the moments of A_0 for B and A_1 for C. This is illustrated by results in Figure 4.10 when both B and C are ellipses of anisotropy ratio 2 and with $\rho_B = \rho_C = 0.1$.

Appendix A

The Justification of the Approximation of the PSF

This appendix is devoted to the formal justification of the PSF approximation (1.8) which was obtained by truncating the Taylor expansion of $w_\pm^\theta$ at the first order: we shall show here that the error caused by this truncation is small. For simplicity, we shall consider only the case when $z = z'$ and $\theta = 0$: the general case may be tackled in a similar way. Without loss of generality, we may set $x' = 0$ and suppose $x \geq 0$. We also suppose that we are not too close to the detectors, namely $z \geq 10^{-2}\,\mathrm{m}$. Moreover, in order to be able to be quantitative, we consider the particular case when $F = 0.4$ and $\tau = 1$.

The expression of the PSF that we want to approximate is (see (1.7))

$$g(x) := g_0((x,z),(0,z)) = \frac{c_0}{4\pi x}\left[f'(w_+(x)) - f'(w_-(x))\right],$$

where $w_\pm(x)$ is given by

$$w_\pm(x) := h^0_{\mathbf{x},\mathbf{x}'}(x \pm Fz) = c_0^{-1}\left(\sqrt{1+F^2}z - \sqrt{z^2 + (x \pm Fz)^2}\right).$$

(Note that, for simplicity of notation, we have removed the dependence of w on θ and z.) An immediate calculation shows that

$$w_\pm(0) = 0, \qquad w'_\pm(0) = \frac{\mp c_0^{-1} F}{\sqrt{1+F^2}}, \qquad w''_\pm(x) = \frac{-c_0^{-1} z^2}{\left((x \pm Fz)^2 + z^2\right)^{3/2}}.$$

Hence, there exists $\xi_x \in [0, x]$ such that

$$w_\pm(x) = \frac{\mp c_0^{-1} F}{\sqrt{1+F^2}} x + c_x \frac{x^2}{2}, \qquad |c_x| = |w''_\pm(\xi_x)| \leq c_0^{-1} z^{-1}.$$

Therefore, the absolute error $E(x)$ due to the truncation of the Taylor series of $w_\pm$ at first order is given by

$$E(x) = c_0(4\pi)^{-1}\left[E_+(x) - E_-(x)\right],$$

where

$$E_\pm(x) = \frac{1}{x}\left[f'(\frac{\mp c_0^{-1}F}{\sqrt{1+F^2}}x + c_x\frac{x^2}{2}) - f'(\frac{\mp c_0^{-1}F}{\sqrt{1+F^2}}x)\right].$$

We now consider two cases, depending on x. First, consider the case when $x > 5\cdot 10^{-3}\,\mathrm{m}$. From the above calculations we immediately have

$$|E(x)| \le c_0(4\pi)^{-1}\frac{4}{x}\left\|f'\right\|_\infty \le \frac{2}{5}c_0 10^3\nu_0 \le 3.7\cdot 10^{12}.$$

Next, consider the case when $x \le 5\cdot 10^{-3}\,\mathrm{m}$. By using again the mean value theorem we obtain

$$E_\pm(x) = c_x\frac{x}{2}f''(\theta_x), \qquad \theta_x = \frac{\mp c_0^{-1}F}{\sqrt{1+F^2}}x + \delta_x c_x\frac{x^2}{2}$$

for some $\delta_x \in [0,1]$. Since $|f''(t)|$ is even and decreasing for $t > 0$, we have that

$$|E_\pm(x)| \le c_0^{-1}\frac{x}{2z}|f''(\frac{c_0^{-1}F}{\sqrt{1+F^2}}x - c_0^{-1}\frac{x^2}{2z})|,$$

since the inequality $x \le 5\cdot 10^{-3}\,\mathrm{m}$ guarantees that $\frac{c_0^{-1}F}{\sqrt{1+F^2}}x - c_0^{-1}\frac{x^2}{2z} > 0$. Therefore we have

$$|E(x)| \le (4\pi)^{-1}xz^{-1}|f''(\frac{c_0^{-1}F}{\sqrt{1+F^2}}x - c_0^{-1}\frac{x^2}{2z})|.$$

Let us look at the right hand side of this inequality. As $x \to 0$ the error tends to 0: this is expected, because of the Taylor expansion around 0. On the other hand, for big x, the value of $|f''(\frac{c_0^{-1}F}{\sqrt{1+F^2}}x - c_0^{-1}\frac{x^2}{2z})|$ is very small, since $|f''(t)|$ decays very rapidly for large t. Therefore, the maximum of the right hand side is attained in a point $x^* \in (0, 0.005)$. The value in this point may be explicitly calculated, and we have

$$|E(x)| \le 4\cdot 10^{12}, \qquad 0 \le x \le 5\cdot 10^{-3}\,\mathrm{m}.$$

To summarize the above derivation, we have shown that the absolute error $E(x)$ is bounded by

$$|E(x)| \le 4\cdot 10^{12}, \qquad x \ge 0. \tag{A.1}$$

We now wish to estimate the relative error $\|E\|_\infty / \|g\|_\infty$. In order to do this, let us compute $g(0)$. Since the Taylor expansion becomes exact as $x \to 0$, we may very well compute $g(0)$ by using the approximated version. Thus, setting $G = F/\sqrt{1+F^2}$ we have

$$\begin{aligned} g(0) &= \lim_{x\to 0} -\frac{c_0}{4\pi x}\left[f'(c_0^{-1}Gx) - f'(-c_0^{-1}Gx)\right] \\ &= \lim_{x\to 0} -G(4\pi)^{-1}\left[\frac{f'(c_0^{-1}Gx) - f'(0)}{c_0^{-1}Gx} + \frac{f'(-c_0^{-1}Gx) - f'(0)}{-c_0^{-1}Gx}\right] \\ &= -2G(4\pi)^{-1}f''(0), \end{aligned}$$

whence $|g(0)| \geq 8.8\cdot 10^{13}$ by a direct calculation of $|f''(0)|$. Finally, combining this inequality with (A.1) allows to bound the relative error by

$$\frac{\|E\|_\infty}{\|g\|_\infty} \leq 5\%.$$

We have proven that the relative error of the approximation obtained by truncating the Taylor expansions of $w_\pm$ at the first order is less than 5%. This has been proven only in the particular case when $z = z'$: the general case may be done by extending the above argument to two dimensions.

Appendix B

Spectrum of some periodic integral operators

Let $C \subset \mathbb{R}^d$ be a $C^{1+\alpha}$-domain for some $\alpha > 0$. It is known that the non periodic operator $\lambda I - \mathcal{K}_C^*$ is invertible on $H^{-1/2}$ for $\lambda \notin \left(-\frac{1}{2}, \frac{1}{2}\right]$ [20, 28]. The positivity of $\mathcal{L}_C$ [46, Section 3.3] also implies that $\lambda\mathcal{I} + \mathcal{L}_C : H^{1/2} \to H^{-1/2}$ is invertible for $\lambda > 0$. We extend these results to the case of periodic Green's function.

Theorem 11. *For any $\lambda > 0$, the operator $\lambda\mathcal{I} + \mathcal{L}_{\#,C} : H^{1/2}(\partial C) \to H^{-1/2}(\partial C)$ is invertible.*

Proof. We first show that the operator $\mathcal{L}_{\#,C}$ is a Fredholm operator. Note that, $\mathcal{L}_{\#,C} = \mathcal{L}_C + \mathcal{R}$ where $\mathcal{R}$ is an integral operator with a smooth kernel and is therefore compact. Moreover, since $\mathcal{L}_C$ has a dimension 1 kernel and image, it is a Fredholm operator. Therefore, $\mathcal{L}_{\#,C}$ is Fredholm. Now we show that $\mathcal{L}_{\#,C}$ is positive semi-definite, and the result will follow from the Fredholm alternative. Since

$$\langle \mathcal{L}_{\#,C}[\varphi], \psi \rangle_{L^2} = - \langle \mathcal{S}_{\#,C}[\mathrm{curl}_{\partial C}\varphi], \mathrm{curl}_{\partial C}\psi \rangle_{L^2}$$

for any $\varphi, \psi \in H^{1/2}(\partial C)$, we just have to show that $\mathcal{S}_{\#,C}$ is negative semi-definite. From the expression (4.12) for $G_\#$, we compute, for any $\varphi \in$

$L^2(\partial C)$,

$$\begin{aligned}\langle \mathcal{S}_{\#,C}[\varphi],\varphi\rangle_{L^2} &= -\sum_{n\in\mathbb{Z}^d\setminus\{0\}}\int_{\partial C}\int_{\partial C}\frac{e^{2i\pi n\cdot(x-y)}}{4\pi^2|n|^2}\varphi(x)\,\varphi(y)\,ds(x)\,dS(y)\\ &= -\sum_{n\in\mathbb{Z}^d\setminus\{0\}}\overline{\left(\int_{\partial C}\frac{e^{2i\pi n\cdot y}}{2\pi|n|}\varphi(y)\,dS(y)\right)}\left(\int_{\partial C}\frac{e^{2i\pi n\cdot x}}{2\pi|n|}\varphi(x)\,ds(x)\right)\\ &= -\sum_{n\in\mathbb{Z}^d\setminus\{0\}}\left|\int_{\partial C}\frac{e^{2i\pi n\cdot y}}{2\pi|n|}\varphi(y)\,ds(y)\right|^2\leq 0.\end{aligned}$$

Therefore, $\mathcal{S}_{\#,C}$ is negative semi-definite, which concludes the proof. □

Theorem 12. *For $\lambda\notin\left(-\frac{1}{2},\frac{1}{2}\right]$, the operator $\lambda I-\mathcal{K}^*_{\#,C}$ is invertible on $H^{-1/2}(\partial C)$.*

Proof. Since $\lambda I-\mathcal{K}^*_C$ is invertible, $\mathcal{K}^*_{\#,C}-\mathcal{K}^*_C$ is a compact operator [9], $\lambda I-\mathcal{K}^*_{\#,C}$ is a Fredholm operator and it is enough to show that it is one-to-one. The proof goes exactly as in [20]. Let us assume that $\lambda I-\mathcal{K}^*_{\#,C}$ is not one-to-one. Then there exists some $f\in H^{-1/2}(\partial C)$ such that

$$\left(\lambda I-\mathcal{K}^*_{\#,C}\right)[f]=0.$$

Let us write

$$\left(\lambda I-\mathcal{K}^*_{\#,C}\right)[f]=\left(\lambda-\frac{1}{2}\right)f+\left(\frac{1}{2}I-\mathcal{K}^*_{\#,C}\right)[f].$$

Since $\left\langle\left(\frac{1}{2}I-\mathcal{K}^*_{\#,C}\right)[f],1\right\rangle_{L^2}=0$, we have $\langle f,1\rangle_{L^2}=0$. Let $u=\mathcal{S}_{\#,C}[f]\in H^1(\mathcal{Y}\backslash\partial C)$. Let

$$A=\int_C|\nabla u(x)|^2\,dx \text{ and } B=\int_{\mathcal{Y}\setminus C}|\nabla u(x)|^2\,dx.$$

Then $A\neq 0$ or $B\neq 0$ since f is not identically zero. Then by Green's formula together with the jump formulas, we have

$$A=\left\langle\left(-\frac{1}{2}I+\mathcal{K}^*_{\#,C}\right)[f],\mathcal{S}_{\#,C}[f]\right\rangle_{L^2},$$

and

$$B=\left\langle\left(\frac{1}{2}I+\mathcal{K}^*_{\#,C}\right)[f],\mathcal{S}_{\#,C}[f]\right\rangle_{L^2}.$$

Since $\left(\lambda I - \mathcal{K}^*_{\#,C}\right)[f] = 0$, we have $\beta = \frac{1}{2}\frac{B-A}{B+A}$. We have therefore a contradiction : we have $|\beta| \leq \frac{1}{2}$ since $A, B \geq 0$. Therefore, $\beta = -\frac{1}{2}$ which implies that $B = 0$. Therefore, u is constant in $\mathbb{R}^d \backslash \cup_{n\in\mathbb{Z}^d} \{C + n\}$. Since u is continuous across ∂C, u is harmonic on C and is constant on ∂C, and by uniqueness of the Dirichlet problem on C, u is constant on C. Therefore,

$$f = \frac{\partial}{\partial \nu}\mathcal{S}_{\#,C}[f]\Big|_+ - \frac{\partial}{\partial \nu}\mathcal{S}_{\#,C}[f]\Big|_- = 0,$$

which is a contradiction.

□

Bibliography

[1] Giovanni S Alberti and Habib Ammari. Disjoint sparsity for signal separation and applications to hybrid inverse problems in medical imaging. *Applied and Computational Harmonic Analysis*, 2015.

[2] Giovanni S Alberti, Habib Ammari, Bangti Jin, Jin-Keun Seo, and Wenlong Zhang. The linearized inverse problem in multifrequency electrical impedance tomography. *SIAM Journal on Imaging Sciences*, 9(4):1525–1551, 2016.

[3] Giovanni S Alberti, Habib Ammari, Francisco Romero, and Timothée Wintz. Mathematical analysis of ultrafast ultrasound imaging. *SIAM Journal on Applied Mathematics*, 77(1):1–25, 2017.

[4] G. Allaire. Homogenization and two-scale convergence. *SIAM J. Math. Anal.*, 23:1482–1518, 1992.

[5] H Ammari, J Garnier, W Jing, H Kang, M Lim, K Solna, and Wang H. *Mathematical and Statistical Methods for Multistatic Imaging*, volume 2098 of *Lecture Notes in Mathematics*. Springer, Cham, 2013.

[6] Habib Ammari, Josselin Garnier, Laure Giovangigli, Wenjia Jing, and Jin-Keun Seo. Spectroscopic imaging of a dilute cell suspension. *J. Math. Pures Appl.*, 105:603–661, 2016.

[7] Habib Ammari, Laure Giovangigli, Hyeuknam Kwon, Jin-Keun Seo, and Timothée Wintz. Spectroscopic conductivity imaging of a cell culture. *Asymptotic Analysis*, 100(1-2):87–109, 2016.

[8] Habib Ammari and Hyeonbae Kang. *Reconstruction of small inhomogeneities from boundary measurements*. Springer, 2004.

[9] Habib Ammari and Hyeonbae Kang. *Polarization and moment tensors: with applications to inverse problems and effective medium theory*, volume 162. Springer, 2007.

[10] Habib Ammari, Francisco Romero, and Cong Shi. A signal separation technique for sub-cellular imaging using dynamic optical coherence tomography. *To appear in Multiscale Modeling and Simulation: A SIAM Interdisciplinary Journal*, 2017.

[11] Tamir Bendory. Robust recovery of positive stream of pulses. *arXiv preprint arXiv:1503.08782*, 2015.

[12] J. Bercoff, G. Montaldo, T. Loupas, D. Savery, F. Meziere, M. Fink, and M. Tanter. Ultrafast compound doppler imaging: providing full blood flow characterization. *IEEE Transactions on Ultrasonics, Ferroelectrics, and Frequency Control*, 58(1):134–147, January 2011.

[13] Jeremy Bercoff, Gabriel Montaldo, Thanasis Loupas, David Savery, Fabien Mézière, Mathias Fink, and Mickael Tanter. Ultrafast compound doppler imaging: Providing full blood flow characterization. *IEEE transactions on ultrasonics, ferroelectrics, and frequency control*, 58(1), 2011.

[14] S. Bjaerum, H. Torp, and K. Kristoffersen. Clutter filter design for ultrasound color flow imaging. *IEEE Transactions on Ultrasonics, Ferroelectrics, and Frequency Control*, 49(2):204–216, Feb 2002.

[15] A. van den Bos. The multivariate complex normal distribution-a generalization. *IEEE Transactions on Information Theory*, 41(2):537–539, 1995.

[16] Nicholas Boyd, Geoffrey Schiebinger, and Benjamin Recht. The alternating descent conditional gradient method for sparse inverse problems. In *Computational Advances in Multi-Sensor Adaptive Processing (CAMSAP), 2015 IEEE 6th International Workshop on*, pages 57–60. IEEE, 2015.

[17] C. Bruneel, R. Torguet, K. M. Rouvaen, E. Bridoux, and B. Nongaillard. Ultrafast echotomographic system using optical processing of ultrasonic signals. *Applied Physics Letters*, 30(8):371–373, 1977.

[18] Emmanuel J Candès and Carlos Fernandez-Granda. Towards a mathematical theory of super-resolution. *Communications on Pure and Applied Mathematics*, 67(6):906–956, 2014.

[19] Colin Gerald Caro. *The mechanics of the circulation*. Cambridge University Press, 2012.

[20] TongKeun Chang and Kijung Lee. Spectral properties of the layer potentials on lipschitz domains. *Illinois Journal of Mathematics*, 52(2):463–472, 2008.

[21] Weng Cho Chew. *Waves and fields in inhomogeneous media*, volume 522. IEEE press New York, 1995.

[22] Yohann De Castro and Fabrice Gamboa. Exact reconstruction using beurling minimal extrapolation. *Journal of Mathematical Analysis and applications*, 395(1):336–354, 2012.

[23] Charlie Demene, Thomas Deffieux, Mathieu Pernot, Bruno-Felix Osmanski, Valerie Biran, Jean-Luc Gennisson, Lim-Anna Sieu, Antoine Bergel, Stephanie Franqui, Jean-Michel Correas, et al. Spatiotemporal clutter filtering of ultrafast ultrasound data highly increases doppler and fultrasound sensitivity. *Medical Imaging, IEEE Transactions on*, 34(11):2271–2285, 2015.

[24] Quentin Denoyelle, Vincent Duval, and Gabriel Peyré. Support recovery for sparse super-resolution of positive measures. *Journal of Fourier Analysis and Applications*, pages 1–42, 2016.

[25] Yann Desailly, Olivier Couture, Mathias Fink, and Mickael Tanter. Sono-activated ultrasound localization microscopy. *Applied Physics Letters*, 103(17):174107, 2013.

[26] Claudia Errico, Juliette Pierre, Sophie Pezet, Yann Desailly, Zsolt Lenkei, Olivier Couture, and Mickael Tanter. Ultrafast ultrasound localization microscopy for deep super-resolution vascular imaging. *Nature*, 527(7579):499–502, Nov 2015. Letter.

[27] Claudia Errico, Juliette Pierre, Sophie Pezet, Yann Desailly, Zsolt Lenkei, Olivier Couture, and Mickael Tanter. Ultrafast ultrasound localization microscopy for deep super-resolution vascular imaging. *Nature*, 527(7579):499–502, 2015.

[28] E.B. Fabes, M. Sand, and J.K. Seo. The spectral radius of the classical layer potentials on convex domains, partial differential equations with minimal smoothness and applications. *IMA Vol. Math. Appl.*, 42:129–137, 1992.

[29] J.-L. Gennisson, T. Deffieux, M. Fink, and M. Tanter. Ultrasound elastography: Principles and techniques. *Diagnostic and Interventional Imaging*, 94(5):487 – 495, 2013.

[30] F. Hecht. New development in freefem++. *Journal of Numerical Mathematics*, 20(3):251–266, 2012.

[31] Samuel T Hess, Thanu PK Girirajan, and Michael D Mason. Ultra-high resolution imaging by fluorescence photoactivation localization microscopy. *Biophysical journal*, 91(11):4258–4272, 2006.

[32] K Iizuka and P Kmtky. Data adaptive signal estimation by singular value decomposition of data matrix. *Proceedings of the IEEE*, 70(6), 1982.

[33] Chulmin Joo, Conor Evans, Thomas Stepinac, Tayyaba Hasan, and Johannes de Boer. Diffusive and directional intracellular dynamics measured by field-based dynamic light scattering. *OPTICS EXPRESS*, 18(3):2858–2871, Jan 2010.

[34] J Jossinet, B Lavandier, and D Cathignol. The phenomenology of acousto-electric interaction signals in aqueous solutions of electrolytes. *Ultrasonics*, 36(1-5):607–613, 1998.

[35] Abdessatar Khelifi and Habib Zribi. Asymptotic expansions for the voltage potentials with two-dimensional and three-dimensional thin interfaces. *Mathematical Methods in the Applied Sciences*, 34(18):2274–2290, 2011.

[36] S. Kim, E.J. Lee, E.J. Woo, and J.K. Seo. Asymptotic analysis of the membrane structure to sensitivity of frequency-difference electrical impedance tomography. *Inverse Problems*, 28, 2012.

[37] Jean-Baptiste Laudereau, Alexander Grabar, Michael Tanter, Jean-Luc Gennisson, and Francois Ramaz. Ultrafast acousto-optic imaging with ultrasonic plane waves. *OPTICS EXPRESS*, 24(4):3774–3789, Feb 2016.

[38] Stephan Link and Mostafa A El-Sayed. Shape and size dependence of radiative, non-radiative and photothermal properties of gold nanocrystals. *International reviews in physical chemistry*, 19(3):409–453, 2000.

[39] E. Mace, G. Montaldo, B. F. Osmanski, I. Cohen, M. Fink, and M. Tanter. Functional ultrasound imaging of the brain: theory and basic principles. *IEEE Transactions on Ultrasonics, Ferroelectrics, and Frequency Control*, 60(3):492–506, March 2013.

[40] Emilie Mace, Gabriel Montaldo, Ivan Cohen, Michel Baulac, Mathias Fink, and Mickael Tanter. Functional ultrasound imaging of the brain. *Nat Meth*, 8(8):662–664, Aug 2011.

[41] Armando Manduca, Travis E Oliphant, MA Dresner, JL Mahowald, Scott A Kruse, E Amromin, Joel P Felmlee, James F Greenleaf, and Richard L Ehman. Magnetic resonance elastography: non-invasive mapping of tissue elasticity. *Medical image analysis*, 5(4):237–254, 2001.

[42] JOSEPH M Mansour. Biomechanics of cartilage. *Kinesiology: the mechanics and pathomechanics of human movement*, pages 66–79, 2003.

[43] Graeme W Milton. *The theory of composites*, volume 6. Cambridge university press, 2002.

[44] G. Montaldo, M. Tanter, J. Bercoff, N. Benech, and M. Fink. Coherent plane-wave compounding for very high frame rate ultrasonography and transient elastography. *Ultrasonics, Ferroelectrics, and Frequency Control, IEEE Transactions on*, 56(3):489–506, March 2009.

[45] G. Nguestseng. A general convergence result for a functional related to the theory of homogenization. *SIAM J. Math. Anal.*, 20:608–623, 1989.

[46] Jean-Claude Nédélec. *Acoustic and electromagnetic equations: integral representations for harmonic problems*, volume 144. Springer Science & Business Media, 2001.

[47] Bradley J Roth. The role of magnetic forces in biology and medicine. *Experimental Biology and Medicine*, 236(2):132–137, 2011.

[48] K Kirk Shung. *Diagnostic ultrasound: Imaging and blood flow measurements*. CRC press, 2015.

[49] Thomas L. Szabo. *Diagnostic Ultrasound Imaging: Inside Out*. Academic Press, Boston, second edition, 2014.

[50] M. Tanter and M. Fink. Ultrafast imaging in biomedical ultrasound. *IEEE Transactions on Ultrasonics, Ferroelectrics, and Frequency Control*, 61(1):102–119, January 2014.

[51] Michael A Thompson, Matthew D Lew, and WE Moerner. Extending microscopic resolution with single-molecule imaging and active control. *Annual review of biophysics*, 41:321–342, 2012.

[52] Kazumi Watanabe. *Integral transform techniques for Green's function*, volume 76 of *Lecture Notes in Applied and Computational Mechanics*. Springer, Cham, second edition, 2015.

Résumé

Les différentes modalités d'imagerie par ondes présentent chacune des limitations en termes de résolution ou de contraste. Dans ce travail, nous modélisons l'imagerie ultrasonore ultrarapide et présentons des méthodes de reconstruction qui améliorent la précision de l'imagerie ultrasonore. Nous introduisons deux méthodes qui permettent d'augmenter le contraste et de mesurer la position super-résolue et la vitesse dans les vaisseaux sanguins. Nous présentons aussi une méthode de reconstruction des paramètres microscopiques en tomographie d'impédance électrique en utilisant des mesures multifréquence et en s'aidant de la théorie de l'homogénisation.

Abstract

Different modalities in wave imaging each present limitations in terms of resolution or contrast. In this work, we present a mathematical model of the ultrafast ultrasound imaging modality and reconstruction methods which can improve contrast and resolution in ultrasonic imaging. We introduce two methods which allow to improve contrast and to locate blood vessels below the diffraction limit while simultaneously estimating the blood velocity. We also present a reconstruction method in electrical impedance tomography which allows reconstruction of microscopic parameters from multi-frequency measurements using the theory of homogenization.

Mots Clés

Ultrasons, Imagerie, Problèmes inverses, Ondes, Tomographie d'impédance électrique, Spectroscopie, Super-résolution

Keywords

Ultrasound, Imaging, Inverse problems, Waves, Electrical impedance tomography, Spectroscopy, Super-resolution